LAYER WAVINESS EFFECTS ON COMPRESSION STRENGTH OF COMPOSITE LAMINATES: PROGRESSIVE FAILURE ANALYSIS AND EXPERIMENTAL VALIDATION

by

Passakorn Duangmuan

A dissertation submitted to the faculty of
The University of Utah
in partial fulfillment of the requirements for the degree of

Doctor of Philosophy

Department of Mechanical Engineering

The University of Utah

August 2012

The University of Utah Graduate School

STATEMENT OF DISSERTATION APPROVAL

The dissertation of **Passakorn Duangmuan**

has been approved by the following supervisory committee members:

Daniel O. Adams	, Chair	**04/26/12** Date Approved
K. L. DeVries	, Member	**04/26/12** Date Approved
Sivaraman Guruswamy	, Member	**04/26/12** Date Approved
A.K. Balaji	, Member	**04/26/12** Date Approved
Ken Monson	, Member	**04/26/12** Date Approved

and by **Timothy Ameel**, Chair of the Department of **Mechanical Engineering**

and by Charles A. Wight, Dean of The Graduate School.

ABSTRACT

Out-of-plane layer waviness, a manufacturing-induced imperfection in multidirectional composite laminates, can produce significant decreases in compression strength. To date, failure predictions based on initial "first-ply" failure analyses as well as compression strength reductions based on the ply fraction containing waviness have shown limited agreement for compression-loaded cross-ply laminates with idealized formations of layer waviness. The objective of this investigation was to extend previous research by employing progressive failure analysis to predict the ultimate compression strength of carbon/epoxy composite laminates with layer waviness. A finite element modeling methodology was developed using cohesive elements available in the commercial finite element code ANSYS to model the formation and growth of delaminations at layer interfaces. Progressive failure analysis within individual composite layers was performed using the Hashin failure criterion and subsequent reduction of appropriate stiffness properties of the failed elements. Strength predictions were compared to mechanical test results obtained for a variety of layer wave formations intentionally fabricated into otherwise wave-free cross-ply laminates. Results suggest that the computational approach used for progressive failure analysis is well suited for predicting strength reductions due to realistic formations of layer waviness in composite laminates.

TABLE OF CONTENTS

LIST OF FIGURES

LIST OF TABLES

ACKNOWLEDGEMENTS

I wish to express my sincere appreciation to my advisor, Professor Daniel Adams, for his knowledge, guidance, and encouragement during the course of this study. I would like to express my heartfelt thanks to the other members of my committee, Dr. K. L. DeVries, Dr. Sivaraman Guruswamy, Dr. A.K. Balaji, and Dr. Ken Monson, for agreeing to be my supervisory committee and for their support.

I would also like to express my sincere gratitude to Mr. John Laakso and Dr. Seubpong Leelavanichkul for their valuable suggestions and support in conducting this research. My thanks also go to my lab mates for the past five years for their contribution towards the completion of this work.

I would like to gratefully thank the Royal Thai Navy, the University of Utah, and the Department of Mechanical Engineering for providing this opportunity and for their support during the course of my Ph.D. studies.

And last but not least, I wish to thank my parents and family for their love, encouragement, and support.

CHAPTER 1

INTRODUCTION

Composite materials are currently being used in many applications that require high stiffness and strength but with minimal weight. Typically, fiber reinforced composites are fabricated into thin layers, referred to as laminas, which are stacked with the desired fiber orientations to produce a composite laminate. The fabrication of composite laminates sometimes leads to out-of-plane layer waviness, an undesired imperfection of the layers within a multidirectional laminate. Typically, layer waviness is produced within a cluster of layers with the laminate as shown in Figure 1.1 and Figure 1.2. Waviness is most commonly observed in cylindrical composite structures as shown in Figure 1.2 , but can also be found in thick, flat laminates. The processing of composite cylinders typically involves compacting the composite layers onto an internal mandrel, causing the layers to migrate inward, buckle, and produce layer waviness.

The presence of layer waviness has been shown to produce significant reductions in the compression strength of composite laminates [1–4]. The compressive strength is an important material property which influences the design and utility of composites for many structural applications. Stress analysis of composite laminates with layer waviness has indicated that waviness produces interlaminar normal stresses and interlaminar shear stresses at the layer interfaces [1–7].

Figure 1.1 Layer waviness in composite laminates.

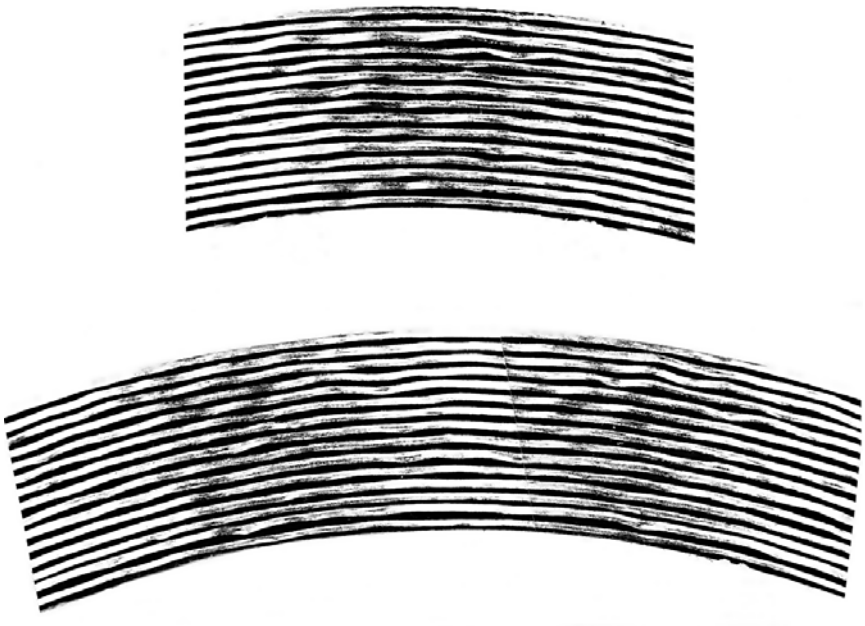

Figure 1.2 Wavy layers in a thick-section composite cylinder.

These stresses can lead to delaminations, which in turn can lead to instability under compression loading and loss of compression strength.

Although finite element modeling methodologies have been implemented to investigate the effects of layer waviness on compression strength, only initial "first-ply" failure predictions based on standard stress analyses have been performed to date [1–4]. However, predicted failure strengths based solely on these initial failures have been shown to not be in good agreement with test results [3]. Further, the formation of delaminations and the progression of failure in composite laminates with layer waviness have not been studied. Therefore, the primary focus of this research is to develop a progressive failure methodology to more accurately predict the compression strength reductions in composite laminates due to layer waviness.

Both mechanical testing and finite element analysis have been performed as part of this research investigation. Initial mechanical testing involved fracture mechanics tests performed on the carbon/epoxy laminates. Both Mode I and Mode II fracture mechanics tests were performed. To investigate layer waviness effects, a series of composite panels were fabricated in a single-step operation to produce wavy layers into otherwise wave-free laminates. Using these test panels, static compression tests were performed to investigate layer waviness effects and validate finite element predictions.

The focus of the finite element modeling performed in this analysis was to develop a progressive failure methodology for investigating compression strength reductions due to layer waviness. A variety of layer wave formations were modeled within cross-ply carbon/epoxy composite laminates. Cohesive elements were utilized to model the formation and growth of delaminations at layer interfaces without making

changes to the finite element mesh [8]. Progressive failure analysis within individual composite layers was performed using the Hashin failure criterion [9] and subsequent reduction of appropriate stiffness properties of the failed element.

Results of finite element analyses were compared to mechanical test results obtained in this investigation as well as those from earlier works performed by Adams and Bell [4], and Adams [10]. These comparisons were used to assess the accuracy of the progressive failure analysis in predicting compression strength reductions from a variety of layer waviness formations.

In Chapter 2, additional background is provided on previous investigations related to predicting and measuring compression strength reductions due to layer waviness. Chapter 3 describes the fabrication methods used to fabricate composite panels with intentional layer waviness, mechanical test methods used, and test results obtained. Chapter 4 describes the finite element analyses performed to predict the failure progressions and strength reductions associated with layer waviness in composite laminates. Finally, Chapter 5 provides a summary of the results and conclusions from the investigation.

CHAPTER 2

LITERATURE REVIEW AND BACKGROUND

2.1 The Influence of Waviness on the Compressive Strength of Composites

This research extends the work of previous studies related to the effects of layer waviness on the compressive response of composite materials. Layer waviness can significantly reduce the compression strength of the composite laminates. In this section, the past analytical, experimental, and numerical research on this subject is briefly reviewed. This review is followed by a summary of the current understanding of layer waviness effects on the compression strength of composite laminates.

The earliest studies related to the influence of waviness on the compressive strength of composites focused on the development of analytical models for waviness of individual fibers within a unidirectional layer, as opposed to waviness of complete layers within a multidirectional laminate. Rosen [11] developed a two-dimensional analytical model to predict the compressive load at which fiber buckling occurs within a unidirectional composite. The individual fibers are modeled as columns supported by the matrix. Rosen showed two possible modes of bucking: an extension mode and a shear mode. For the extension mode, adjoining fibers were presumed to buckle in opposite directions (out of phase) and shear deformation in the matrix was neglected for this

mode. For the shear mode, adjoining fibers were presumed to buckle in same directions (in-phase) and extensional deformation in the matrix was neglected for this mode. Rosen used an energy method to generate analytical expressions for the critical compression stress in the two modes. The largest compression stress from the two modes was used as the compression strength. However results of the analytical model were found to over predict compression strength.

Davis [12] investigated fiber waviness within a unidirectional composite material using the methodology developed by Rosen [11]. Davis modeled all of the fibers within the composite as initially sinusoidal in shape, which resembled the shear bucking mode in Rosen's model. Two failure modes were considered: fiber-matrix delamination caused by interlaminar shear stress, and shear instability. The governing equation was solved using a finite difference routine and the interlaminar shear stress was predicted as a function of the applied compressive load. Davis also used an energy method to develop an equation to predict the compression stress at which shear bucking occurs. Result showed that strength reduction was dependent on the level of fiber waviness. The dominant failure mode was a shear bucking failure.

Hyer [13] developed a similar model to that of Davis [12] to investigate the influences of fiber and matrix properties on fiber waviness within unidirectional composite under compressive load. Hyer assumed that sinusoidal shaped fibers deformed in a shear mode. This model used energy methods to determine the wave amplitude at a known applied compressive load. The initial wave amplitude of the fiber was 0.10 times of the fiber diameter whereas the half wavelength was 10 times larger than the fiber

diameter. Reducing the shear modulus of the matrix material was determined to decrease the compressive strength of the composite.

A fiber kinking model, which included initial fiber misalignment, was developed by Argon [14]. The presence of initial fiber misalignment under compressive load was found to generate interlaminar shear stresses as a result of the fiber rotation. The interlaminar shear stress was found to increase with increasing fiber angle. Shear buckling failures were predicted. A similar fiber kinking model was developed by Budiansky [15]. This model considered plasticity of the matrix phase and the initial fiber misalignment. The author concluded that the applied stress level at which kinking occurs was sensitive to the degree of fiber misalignment within the unidirectional composite.

Steif [16] studied fiber kinking in unidirectional composite materials under compressive loading. This kinking model was separated into two steps. In the first step, misalignment was assumed within a bundle of fibers and fiber failure within the wavy composite was investigated using a micro-buckling model. In the second step, the compression stress at the formation of a complete kink band was predicted at the point of fiber rupture.

Guynn [17] studied parametric variables that influence fiber microbucking initiation in composite laminates. The initiation of fiber microbucking in wavy 0° fibers was modeled using two-dimensional finite element analysis including both geometric and material nonlinearity. The parameters investigated included the matrix nonlinear constitutive behavior, the initial fiber waviness, and the fiber/matrix interfacial debonding. To study the influence of matrix nonlinear constitutive behavior, an amplitude-to-wavelength ratio of 0.0050 was used with four different matrix behaviors: a

linear and three nonlinear data (21°C, 77°C, and 132°C). For three nonlinear data, yield strength values increased as the temperatures decreased. Results indicated that reducing shear yield strength significantly decreases the fiber microbuckling initiation strain levels. To investigate the effects of initial fiber waviness, four levels of waviness were considered, with amplitude-to-wavelength ratios of 0.0000, 0.0025, 0.0050, and 0.0075. Results suggested that even small amount of initial fiber waviness level can considerably reduce the strain levels at which fiber microbucking initiates. Further, increasing the severity of fiber waviness produces increasing shear strain and reduced strain levels for initiation of microbuckling. To investigate debonding effects, a debond length that was 11% of the fiber length was located in two locations along the fiber: near the symmetry line and along the region of the localized maximum shear strains. Furthermore, three debond lengths were investigated: 11%, 25%, and 50% of the fiber length. The debond length and location were found to have a significant effect on the fiber microbuckling strains. The critical debond location was determined to be in the area of maximum shear strain.

The effects of layer waviness within multidirectional laminates have been studied by several researchers. Shuart [18] modeled layer waviness in composite laminates by representing the fibers of the layer of the laminate as a plate and the matrix as an elastic foundation. The thicknesses of the layers were determined by the fiber and matrix volume fractions of the composite. Shuart used a linear buckling analysis to predict short-wavelength buckling mode shapes and a geometrically nonlinear analysis to study layer waviness effects. The effects of layer waviness were considered and the interlaminar shear strains were calculated at boundary interfaces. Shuart used four different laminates

to investigate layer waviness effects: $[0_2]_s$, $[0/90]_s$, $[\pm 45]_s$, and $[+45/0/-45/90]_s$. Additionally, two values of amplitude-to-layer thickness ratio were considered. For the small amplitude-to-layer thickness ratio of 0.1, the load carrying capacity for these laminates was decreased between 5 to 17 %. The load carrying capacity for these four laminates was reduced by between 12 and 36 % for the greater amplitude-to-layer thickness ratio of 0.5. Shuart concluded that the maximum shear strain occurred at the inflection points of the wave (midway between central crest and adjacent trough). Three possible failure modes were considered in this study: short-wavelength buckling, interlaminar shear failure, and in-plane shear failure.

Peel [19] investigated compression failure of angle-ply laminates containing layer waviness. IM7/8551-7A laminates were used for experiments and analysis. Various failure modes including kink bands, brooming, interlaminar shearing, in-plane transverse tensile splitting, and in-plane shearing were observed in the failed specimens. Several wave amplitudes and wavelengths were considered in the laminate containing layer waviness. Result showed that the predicted failure loads were a function of the off-axis angle, relative severity of the wave amplitude and wavelength, and the dominant failure mode. For fiber compression and transverse tension failure, the wavelength was more predominant than the wave amplitude in predicted failure loads. Therefore, different compression strengths were predicted in laminates with the same wave amplitude-to-wavelength ratios but with different wavelengths.

Hyer et al. [5] and Telegadas and Hyer [6, 7] were among the first researchers to investigate layer waviness of complete layers within a multidirectional composite laminate. They considered the stress state involving an isolated group of wavy layers

within composite cylinder. Hyer et al. [5] used both analytical and finite element analyses to investigate the state of stress in a region of a composite laminate with layer waviness. An isolated cosinusoidal wave was modeled in a perfect composite cylinder. The region including the wavy layers was modeled using finite element. The focus was on the forms of waviness observed in thick cross-ply composite cylinders that were designed for external hydrostatic pressure loading. Moreover, the effects of material property variations were investigated to account for changes in fiber orientation and fiber volume fractions in the wavy region. Hyer et al. concluded that layer waviness could generate significant shear stresses in the cylinder and could effectively change material properties as well.

Telegadas and Hyer [6] further studied the stress state around wavy layers in hydrostatically loaded composite cylinders. The interlaminar normal and shear stress profiles along the layer interface were investigated. Thermal stresses were also considered. The radial location of the wavy layer strongly affected the interlaminar normal stress. The inner radial, mid-radial, and outer radial locations through the cylinder thickness were examined. The maximum compressive interlaminar normal stress was found when the wavy layers occurred on the outer radial location. However, the interlaminar normal stress was essentially tensile at the inner radial location. Telegadas and Hyer [7] further extended their research to analyze the failure pressure levels, modes, and failure location. The maximum stress failure criterion was employed for this study. Variations of wavelength and wave amplitude were considered. The three values of wavelengths divided by the thickness of one layer were 5, 10, and 20. The three values of wave amplitudes divided by the thickness of one layer were 0.5, 1, and 2. Nine wave

geometries containing the various wave geometries were studied at three radial locations in the cylinder. Three distinct failure modes were recognized. The first failure mode, compression failure in the fiber direction, occurred for the less severe wave geometries (long wavelength coupled with small amplitude). The second mode of failure was interlaminar shear failure that occurred near the inflection point of the wave. Interlaminar shear failure was predicted when wave severity was increased (short wavelength with large amplitude). The last mode, interlaminar tensile failure, was produced at the inner radial location since the wavy layer deformed outward under the load.

Among the earliest experimental investigations of layer waviness was the work of Abdallah et al. [20], who used Moiré interferometry to investigate the strain fields produced by wavy layer regions in composite rings under external pressure. Different types of cylinder fabricated from serveral kinds of carbon fiber composite materials were used in this study. Various degrees of layer waviness were investigated in several composite rings. The lowest failure pressures and strains were associated with the composite rings which contained the greatest severity of layer waviness. In these composite rings, failure was found to occur in regions of severe layer waviness. Furthermore, the displacement fields showed that the locations of high interlaminar shear strains were in the surrounding area of the more severe layer waviness. In summary, the location of maximum shear deformation occurred at the inflection points of the waves. Harris and Lee [21] also used Moiré interferometry to investigate corrugated aluminum/epoxy model materials designed to better understand the effects of layer waviness in composite laminates.

Bogetti et al. [22] developed analytic models to investigate the effects of layer waviness on the stiffness and strength reduction of $[90/0/90]_T$ composite laminates: AS4 Graphite/PEKK and S2 Glass/PEKK. Two-dimensional analytical modeling was employed in this study. A model was developed to predict the elastic properties and thermal expansion coefficient of $[90/0/90]_T$ composite laminates that contained layer waviness in the 0° layer. This study investigated the influence of layer waviness on the stiffness and strength reduction of cross ply composite laminates, which were normally used in filament wound cylinder for hydrostatic pressure loading. Waviness in the 0° layer was assumed to exist in the axial direction of the cylinder only. A half-sine wave was employed to represent the wavy ply configuration. To investigate the effects on the elastic properties and thermal expansion coefficient, the half-sine wave was divided into discrete sections in the 0° direction. The maximum stress failure criterion was used in failure analysis. The stiffness decrease due to layer waviness occurred primarily in the direction of the wavy layer. The degree of ply waviness significantly influenced the amount of stiffness reduction. Greater stiffness reduction was observed when the wave amplitude was increased and the half-sine wavelength was decreased. Increasing wave amplitude was observed to increase the thermal expansion coefficient up to 60% in the wavy ply direction. Interlaminar shear failure of the wavy layer was predicted to occur, significantly reducing the strength of the laminates when loaded in the wavy ply direction. Additionally, the strength reduction was very sensitive to the degree of waviness.

The significant influence of shear nonlinearity in modeling layer waviness was recognized by Adams and Hyer [2]. Additionally, Bogetti et al. [23] extended their

previous research to examine the effect of ply waviness with nonlinear shear behavior of composite laminates. A three-dimensional analytical model was developed to predict nonlinear mechanical behavior of two different wavy ply geometries: a $[90/0/90]_T$ and $[90/\pm\beta/90]_T$. The geometric parameter β represented the winding angle (cross-over model). The $\pm\beta$ plies were inserted between two nonwavy 90° plies. The half-sine wave segment was also employed to model the wavy ply. Results showed that the stress/strain relationships from the linear and nonlinear cases were similar at low load level. At the ultimate load level of the nonlinear case, however, the ultimate stress value was significantly higher compared to that of the linear case due to the nonlinear material response. No influence of interlaminar shear on ultimate failure was observed in the nonlinear analysis.

Adams and Hyer [1, 2, 24] performed a combined experimental and computational investigation of layer waviness effects in flat thermoplastic composite laminates under compression loading. Similar to the previous work by Telegadas and Hyer [6, 7] the authors used finite element analysis to investigate stress fields associated with idealized forms of waviness. Using carbon/polysulfone thermoplastic composite laminates, the authors developed a method to intentionally fabricate isolated layer waviness formations into otherwise wave free composite laminates. A 22 ply $[90_2/0_2/90_2/0_2/\ 90_2/\overline{0_{2w}}]_s$ cross-ply laminate was selected for investigation. For this laminate, each individual layer consisted of double plies in thickness. The wavy 0° layer was placed at the midplane of the laminate. Note that the designation, $\overline{0_{2w}}$ indicates the 0° wavy layer, and the overbar implies that the layer was not repeated in the symmetric stacking sequence. The layer wave geometry was characterized individually for each

specimen because of the slightly difference of wave geometry. Figure 2.1 shows wavelength, λ, and wave amplitude, δ. Layer wave "severity" was determined by the parameter, δ/λ.

Several wave severities of layer waviness were considered, all for a single 0° layer within a multilayer cross-ply laminate consisting of alternating 0° and 90° layers. Uniaxial compression testing was performed on specimens cut from the composite panels and compression strength reductions due to the layer waviness were obtained. For this study, the ASTM D3410 test method with the IITRI compression test fixture was employed. Results showed that the reduction in static strength of laminates containing layer waviness in the central 0° layer ranged from 1% to 36%. Adams and Hyer [24] also investigated the compression fatigue response as a result of the influence of layer waviness. Several maximum fatigue levels were applied to the specimen containing a moderate level of wavy layer to establish *S-N* curves. Compression fatigue testing for this study was executed using test fixture designed and manufactured at NASA Langley Research Center.

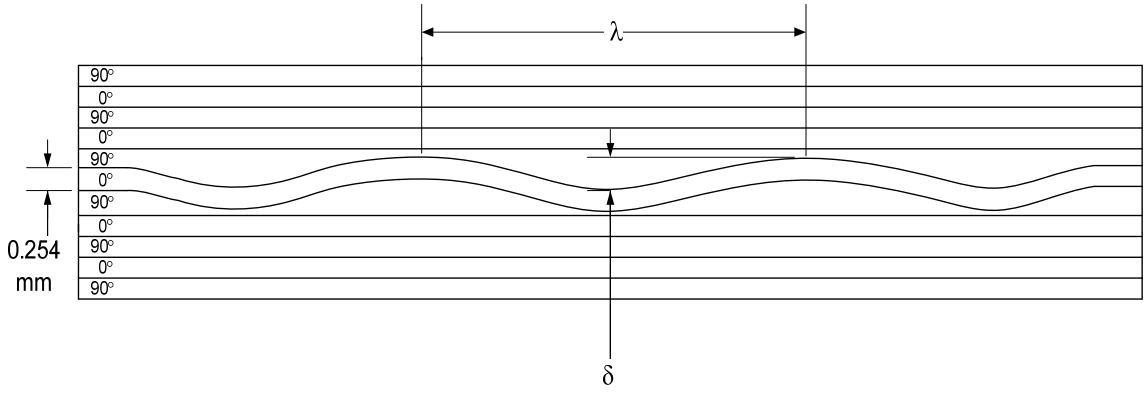

Figure 2.1 Layer waviness in $[90_2/0_2/90_2/0_2/\ 90_2/\ \overline{0_{2w}}\ ]_s$ cross-ply laminate.

Testing of specimens with several wave severities were performed under load control. Results demonstrated a reduction of the compression fatigue life as a result of the moderate layer waviness. Specimens manufactured from carbon/polysulfone thermoplastic composites containing moderate waviness (δ/λ ratios between 0.05 and 0.06) experienced a 1.5 decade loss of compression fatigue life compared to specimens with no layer waves. There were two failure modes observed in this study. Each failure mode corresponded to different failure locations: at the waviness and within the grips. Catastrophic and sudden failure occurred at the location of the layer wave in a "brooming" manner. Specimens without waviness typically failed within the grip and experienced localized bucking of each of the 0° layers. If the loading continued, a brooming failure occurred at the edge of the grip. The stress level of these layer wave specimens related to the 10^6 cycle run-out was reduced to about 45% of the static compression strength compared to the wave-free specimens.

Adams and Hyer [1] additionally used a finite element analysis to investigate the influences of layer waviness in flat compression-loaded thermoplastic composite laminates. Two classifications of wave geometry were considered: a moderate and severe layer wave. Material nonlinearity was considered in this analysis. A maximum stress failure criterion was used and three failure modes were considered: fiber compression failure, interlaminar shear failure, and interlaminar tension failure. A maximum interlaminar shear stress failure was predicted at the inflection point of the wavy 0° layers. The value of maximum interlaminar shear stress of the severe layer wave was three times more than the value of the moderate layer wave. The peak value of interlaminar tensile stress of the severe layer wave was two times of that of the moderate

layer wave but the peak locations of the two layer wave geometries were different. For a fiber compression failure, the strength reduction of the moderate layer wave was only 4 percent comparing to the nonwavy laminate. However, the model predicted 48 percent strength reduction in compression for the severe layer wave. The failure was predicted along the layer wave centerline within the 90° layer immediately above the wavy 0° layer.

Bradley, Adams, and Gascoigne [3] furthered the work of Adams and Hyer [1, 2, 24] to investigate more complex formations of "nested" layer waviness, involving several adjacent layers with waviness. However, their work focused on carbon/epoxy thermoset composites rather than thermoplastic composites. IM7/8551-7A carbon/epoxy was used to fabricate two cross-ply laminates, which consisted of alternating 0° and 90° layers. Two layer wave formation of the cross-ply laminates were intentionally fabricated into otherwise wave-free laminates: a single wavy layer and three nested wavy layers as shown in Figure 2.2. These "nested" layer waviness formations were investigated using a combined experimental and computational study. To fabricate multiple-layer waviness into otherwise wave-free composite laminates, a single-step fabrication procedure was developed. To fabricate a single wavy 0° layer into a cross-ply laminate, two thin strips of the carbon/epoxy prepreg material were removed from the adjacent 90° plies as shown in Figure 2.3. One strip was formed into a cylinder and placed above the 0° layer and the other strip was split in half, formed into two small cylinders, and placed below the 0° layers. The entire composite laminate was then placed into a steel mold and cured in a heated press. Three nested wavy 0° layers were fabricated in a similar method as shown in Figure 2.4.

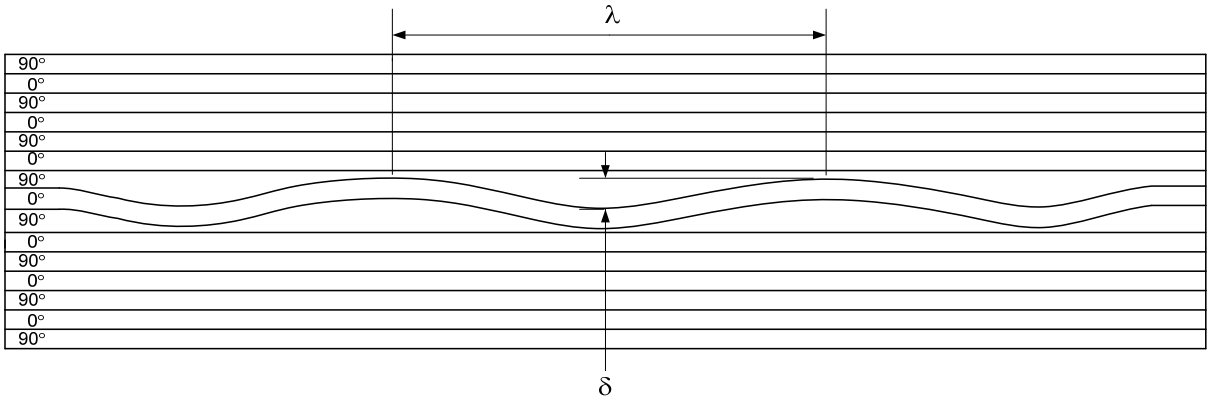

(a) Single wavy layer.

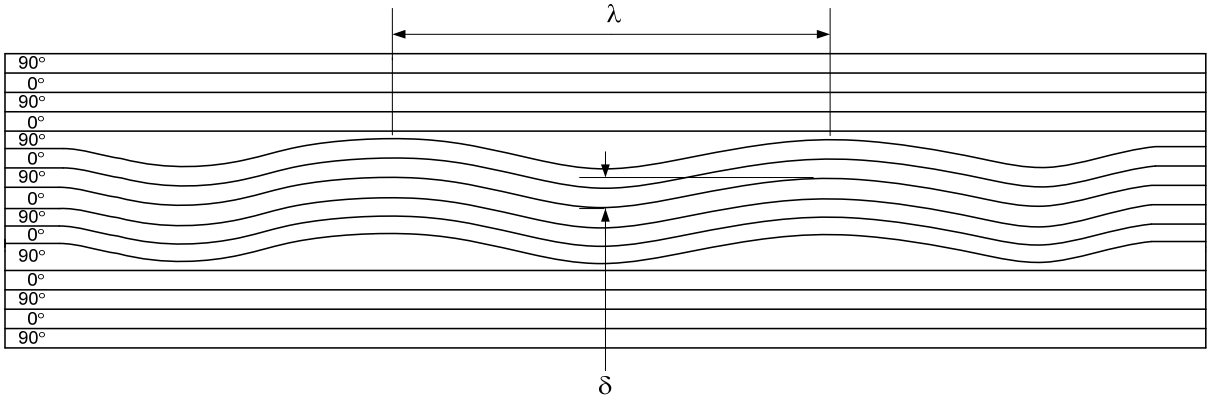

(b) Three nested wavy layers.

Figure 2.2 Two layer wave formations in the cross-ply laminates.

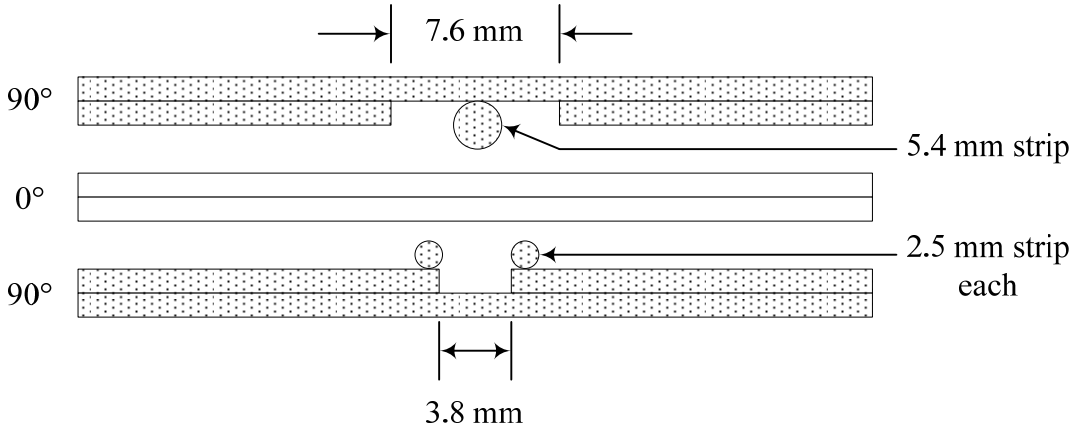

Figure 2.3 Fabrication of single wavy 0° layer.

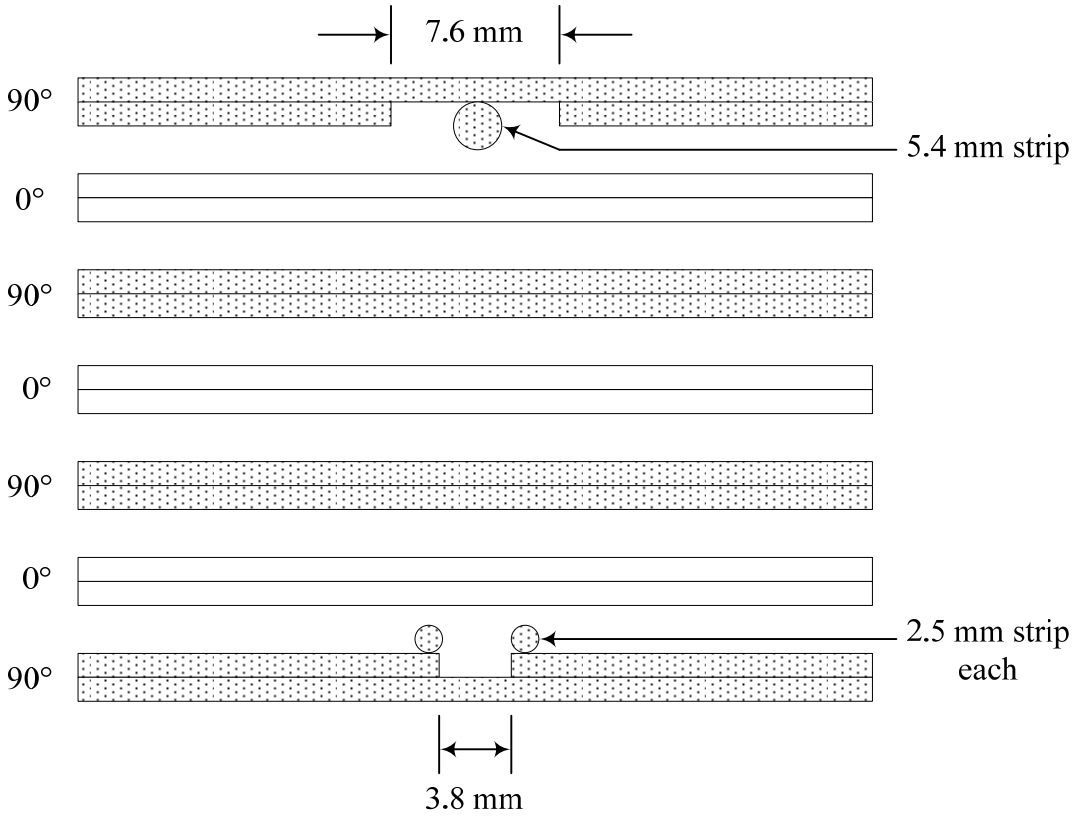

Figure 2.4 Fabrication of three nested wavy 0° layer.

In this study, Moiré interferometry, mechanical testing, and finite element analyses were performed to determine compressive strengths and interlaminar strains. Finite element analyses based on previous work by Adams and Hyer [1, 2, 24] were performed to determine the stress and strain distributions resulting from waviness for both the single layer wave and the three nested layer wave. The maximum stress failure theory was used to predict fiber failure and the maximum stress failure criterion based on comparing values of five individual stress components to corresponding material allowable strengths. Fiber failure was predicted when the longitudinal compressive stress exceeded the longitudinal strength. The Hashin failure criterion [9] was applied to stresses in the plane of the model, using the interlaminar shear and normal stresses to predict matrix failure at the layer interfaces. Moiré interferometry was performed for validation and compression testing was performed to determine the effects of layer waviness on compression strength. The finite element results for both wave geometries indicated that the peak interlaminar normal strain occurred at the central wave trough along the upper interface of the top wavy 0° layer. The peak interlaminar shear strain occurred near the inflection points of the top wavy 0° layer along the upper interface layer. Both interlaminar normal and shear strains results predicted as a result of layer waviness were in agreement with the displacement fields form Moiré interferometry. In this work, the strength for the single layer wave formation reduced 12.1% and the strength for three nested layer wave decreased 35.8%. No direct relationship between the magnitude of the interlaminar stresses and the strength reductions due to waviness were observed. Therefore, results from the stress analysis were not able to be used to accurately predict strength reductions.

Adams and Bell [4] performed an additional experimental investigation of layer waviness in carbon/epoxy thermoset composites. Cross-ply laminates were fabricated using IM7/8551-7A carbon/epoxy. In an effort to better understand the compression strength reductions produced from layer waviness, the authors investigated waviness in which the amplitude δ and wavelength λ of the layer waviness was held constant, but the fraction of the 0° layers within a multi-layer cross-ply laminate was varied. In the fabrication of wavy 0° layers into the crossply laminates, the measured values of layer wave severity δ/λ were from 0.067 to 0.072, which were assumed to be constant. The wavy 0° layer fraction, f_w is the number of wavy 0° layers divided by the total number of 0° layers within the laminate. The range of wave fraction, f_w was varied from a low of 0.14 (1/7) to a high of 0.71 (5/7). The fabrication method used was similar to that developed previously by Bradley et al. [3]. The cluster of wavy layers was placed about the laminate midplane. The IITRI compression test fixture was employed to perform the static compression testing. During the test, signs of initial failure could not be detected audibly or visually since failure was catastrophic and sudden. Results from static compression testing showed that the strength reduction for laminates containing waviness in 33% or less of the 0° layers within the laminate was approximately equal to the percentage of 0° wavy layers. In laminates where greater than 33% of the 0° layers had waviness, approximately a 35% strength reduction was observed, independent of the percentage of wavy 0° layers. These results indicated that compressive strength reductions due to layer waviness may be estimated by the percentage of 0° layers containing waviness for composite laminates containing layer waviness.

Chun, Shin, and Daniel [25] investigated analytically and experimentally the effects of fiber waviness on the nonlinear behavior of unidirectional composites under tensile and compressive loadings. Three formations of fiber waviness with sinusoidal waviness were studied: uniform, graded, and localized fiber waviness. The complementary energy density and incremental approaches were employed in the analysis. All fibers with sinusoidal waviness were assumed to be parallel to each other. Samples with several degrees of fiber waviness were fabricated using carbon/epoxy. The wave severities (δ/λ) of the specimens fabricated were 0.011, 0.034, and 0.059. The IITRI compression test fixture was used for the compression testing. Results showed that Young's modulus, E_x decreased with increase of the wave severity but no fiber waviness effect occurred on E_y. However, the E_z slightly increased with increase of the wave severity. Additionally, G_{yz} slightly decreased but the G_{xy} and G_{xz} increased with increase of the wave severity. They concluded that the predictions were in good agreement with experimental results for the uniform fiber waviness model.

Hale and Villa [26] studied the influence of opposing wave nesting under compression loading using IM7/8551-7A carbon/epoxy. Two opposing nest laminates that consisted of close opposing nest sample and separated opposing nest sample were fabricated. Two-dimensional finite element analyses were performed to predict the interlaminar normal and shear strain distributions. Three wave formations of the finite element models were investigated: close opposite, moderately separated opposite, and separate opposite undulations. Moire´ interferometry was used to study experimental strain distributions and wave interaction effects. The authors concluded that maximum interlaminar shear and normal strains are a function of the severity of individual waves

found within the laminate, and local interactions among individual waves were not significant.

Jumahat et al. [27] experimentally and theoretically studied fiber microbuckling and fiber kinking failure mechanisms in carbon fiber/toughened epoxy. Both compression and in-plane shear testing was performed. Results revealed that the failure initially occurred by fiber microbuckling, followed by fibers cracking at two points and generating a kink band. Fiber microbuckling and fiber kinking failure models from Berbinau [28] and Budiansky's [15] were used, and a new combined failure model was developed. The fiber microbuckling compressive stress was predicted to increase when the shear strength was increased. An initial fiber misalignment angle was investigated and a higher compressive strength was obtained from the model with a smaller initial fiber misalignment angle. The predicted compressive strength was in good agreement with the experimental result.

In summary, previously performed research investigations have documented that layer waviness produces significant interlaminar normal and shear stresses. Additionally, layer waviness has been shown to produce significant strength reductions in cross-ply composite laminates. Even though the finite element modeling methodologies implemented have properly predicted deformations and strains determined experimentally, the simple stress-based failure criteria used have not been adequate for predicting compressive strength reductions associated with layer waviness. The application of stress-based failure criteria has resulted only in the identification of probable locations of initial damage formation. Further, predicted failure loads based on initial damage formation have been shown to not be in good agreement with test results.

However, results from both experimental and computation studies suggest that failure may be initiated by the high interlaminar normal and/or shear stress that are produced by layer waviness at the layer waviness. Thus, the need remains to develop a method to predict compression strength reductions due to layer waviness in composite laminates.

2.2 The Virtual Crack Closure Technique

Fracture mechanics is a field of solid mechanics that focuses on the propagation of cracks in materials. In fracture mechanics, crack propagation criteria are presented in several forms, including the fracture toughness or strain energy release rate, G. For finite element modeling performed in this research, a cohesive-zone model was used within interface elements at the layer boundaries of composite laminates. The use of interface elements allowed for the modeling of delamination initiation and propagation under mixed-mode interface loading. The strain energy release rate components, G_{I} and G_{II}, were verified using the virtual crack closure technique (VCCT). Finite element models were developed to determine the strain energy release rate based on the virtual crack closure technique. In this section, previous studies associated with the virtual crack closure technique are reviewed.

In 1920, Griffith [29] presented the problem of fracture in terms of an energy balance according to the first law of thermodynamics, which stated that energy cannot be created nor destroyed. This concept was applied by Griffith to the growth of a crack. The propagation of a crack could occur under the condition that a process caused the total energy to decrease or remain constant. The total energy of the system under equilibrium conditions can be expressed as:

$$\frac{dE}{da} = \frac{dU_a}{da} + \frac{dU_s}{da} = 0, \tag{2.1}$$

where E is total energy, U_a is the potential energy, U_s is surface energy, and a is an initial crack length. Terms $\frac{dU_a}{da}$ and $\frac{dU_s}{da}$ can be defined as the strain energy release rate, G and the critical strain energy release rate, G_c respectively. If the G is larger than G_c , crack growth occurs. This condition for crack growth thus becomes

$$G \geq G_c, \tag{2.2}$$

The crack closure method employed in this research required two analysis steps to determine the strain energy release rate [30]. This two-step method included both the condition with the crack extended as well as the crack closed, as shown in Figure 2.5 and Figure 2.6, respectively. This crack closure method is based on Irwin's assumption that the energy release rate in the process of crack extension is equivalent to the work needed to close the crack to the primary condition [31]. In Figure 2.5 and Figure 2.6, the energy release, ΔE as the crack extended by small amount Δa from a to $a + \Delta a$ is equal to the energy required to close the crack,

$$\Delta E = \frac{1}{2}\left[F_x.\Delta u_i.F_z.\Delta w_i\right], \tag{2.3}$$

where F_x and F_z are the shear and normal forces required to close the crack at node i (Figure 2.5). The terms Δu_i and Δw_i are shear and normal displacements at node i (Figure 2.6). Thus, Irwin calculated this work per unit thickness to close a small amount, Δa as

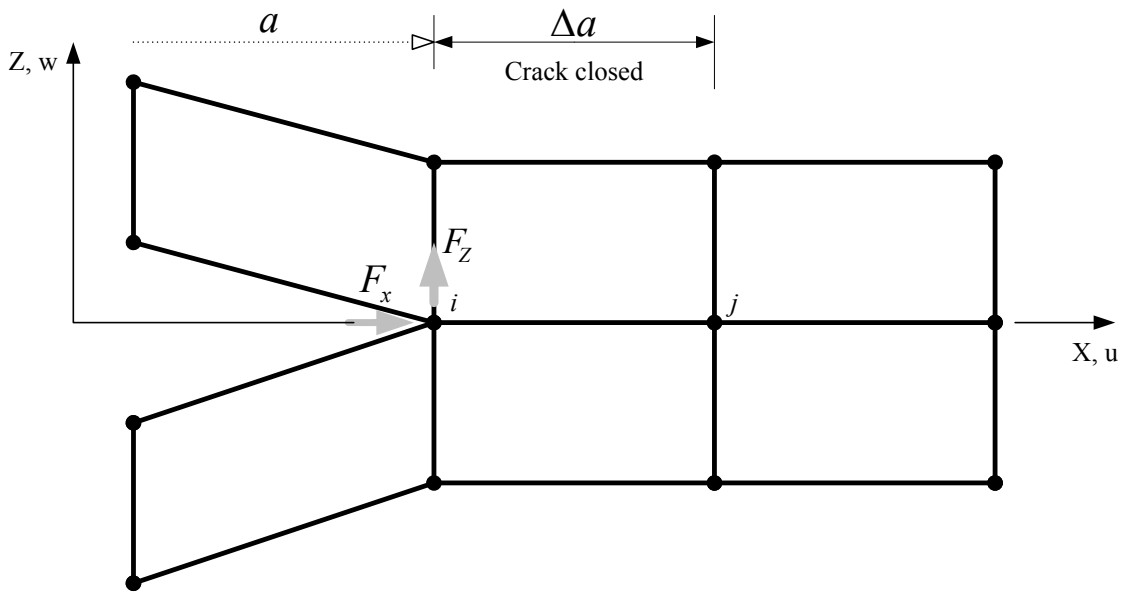

Figure 2.5 Crack closure method (crack closed).

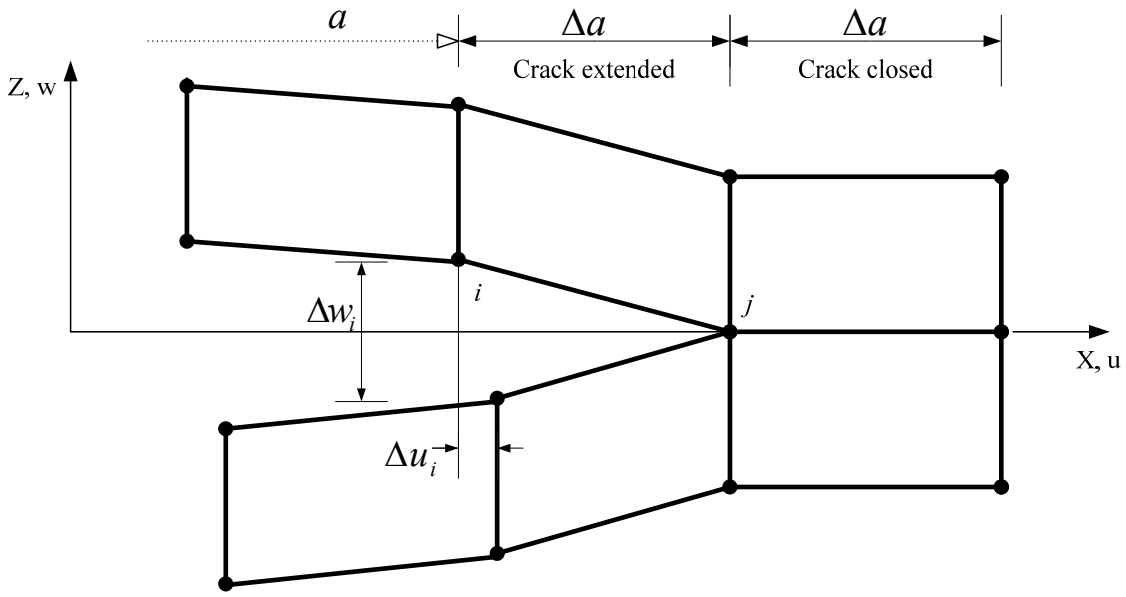

Figure 2.6 Crack closure method (crack extended).

$$\Delta W = -\frac{1}{2}\int_0^{\Delta a} \bar{\sigma}.\,\Delta\bar{u}\; da, \tag{2.4}$$

where $\bar{\sigma}$ are the opening or normal stress (σ_{zz}) as well as shear stresses (τ_{xy}, τ_{yz}). The term $\Delta\bar{u}$ are the relative displacement components, and Δa is the change in virtual crack length as shown in Figure 2.7. Therefore, the strain energy release rate for the crack length *a* is

$$G = \lim_{\Delta a \to 0} \frac{1}{2\Delta a}\int_0^{\Delta a} \bar{\sigma}.\,\Delta\bar{u}\; da. \tag{2.5}$$

The strain energy release rate for the crack can be calculated for mixed mode conditions as shown in Figure 2.7.

The total strain energy release rate for the crack, G_T is given by

$$G_T = G_{\mathrm{I}} + G_{\mathrm{II}} + G_{\mathrm{III}}. \tag{2.6}$$

The three components of strain energy release rate can be determined by substituting the stresses and relative displacements into equation (2.5), yielding

$$\begin{aligned} G_{\mathrm{I}} &= \lim_{\Delta a \to 0} \frac{1}{2\Delta a}\int_0^{\Delta a} \sigma_{zz}.\,\Delta w\, da \\ G_{\mathrm{II}} &= \lim_{\Delta a \to 0} \frac{1}{2\Delta a}\int_0^{\Delta a} \tau_{xz}.\,\Delta u\, da \\ G_{\mathrm{III}} &= \lim_{\Delta a \to 0} \frac{1}{2\Delta a}\int_0^{\Delta a} \tau_{yz}.\,\Delta v\, da. \end{aligned} \tag{2.7}$$

Rybicki and Kanninen [32] developed a method using the finite element technique to calculate the energy release rate.

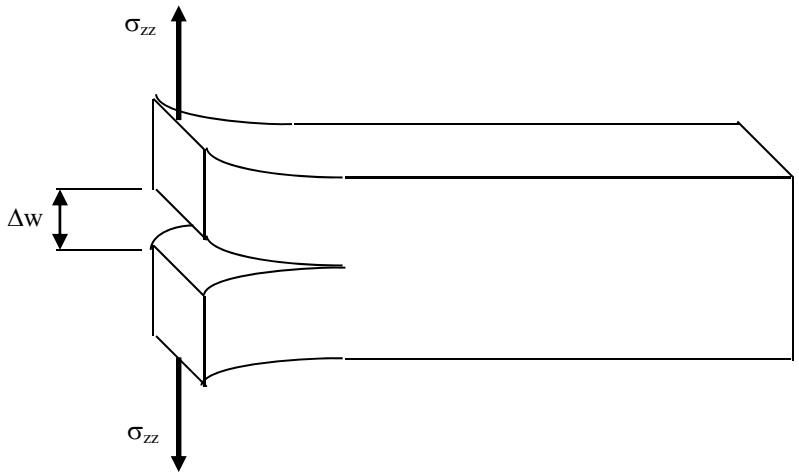

(a) Mode I: Interlarminar tension.

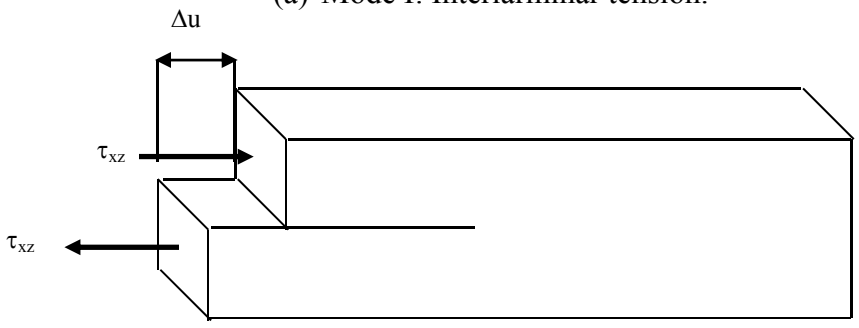

(b) Mode II: Interlaminar in plane shear.

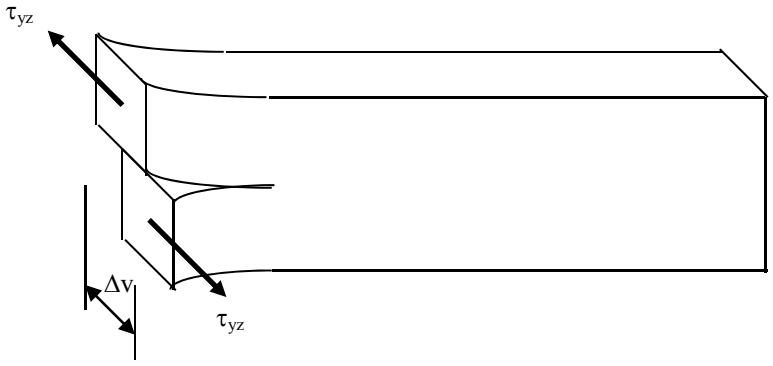

(c) Mode III: Interlerminar out of plane shear.

Figure 2.7 Fracture modes.

This method is referred to as the virtual crack closure technique (VCCT). This technique was used to investigate crack propagation in a double cantilever beam specimen. Rybicki et al. [33] used the virtual crack closure technique to determine the energy release rate associated with the free-edge delamination problem. The energy release rate associated with the three fracture modes were calculated using finite element analysis. The nodal forces required to close the crack extension and nodal displacements of the element as given as

$$
\begin{aligned}
G_{\mathrm{I}} &= \frac{1}{2\Delta a B}\left[F_z\left(w_i - w_{i'}\right)\right] \\
G_{\mathrm{II}} &= \frac{1}{2\Delta a B}\left[F_x\left(u_i - u_{i'}\right)\right] \\
G_{\mathrm{III}} &= \frac{1}{2\Delta a B}\left[F_y\left(v_i - v_{i'}\right)\right],
\end{aligned}
\tag{2.8}
$$

where F_{x}, F_{y}, F_{z} are the element nodal forces. *u, v, w* are the nodal displacement in x, y, z respectively. The term *B* is the nodal thickness and Δa is the change in virtual crack length as shown in Figure 2.8.

2.3 Interface Element with Cohesive Zone Material Model

Interface elements may be used between layers within composite laminates to simulate interlaminar delaminations. In this research, an ANSYS cohesive zone material model [34] was employed using interface elements at selected layer interfaces of the composite laminates where the possibility of delamination was identified. The initial geometric thickness of the cohesive elements was designated to be zero before.

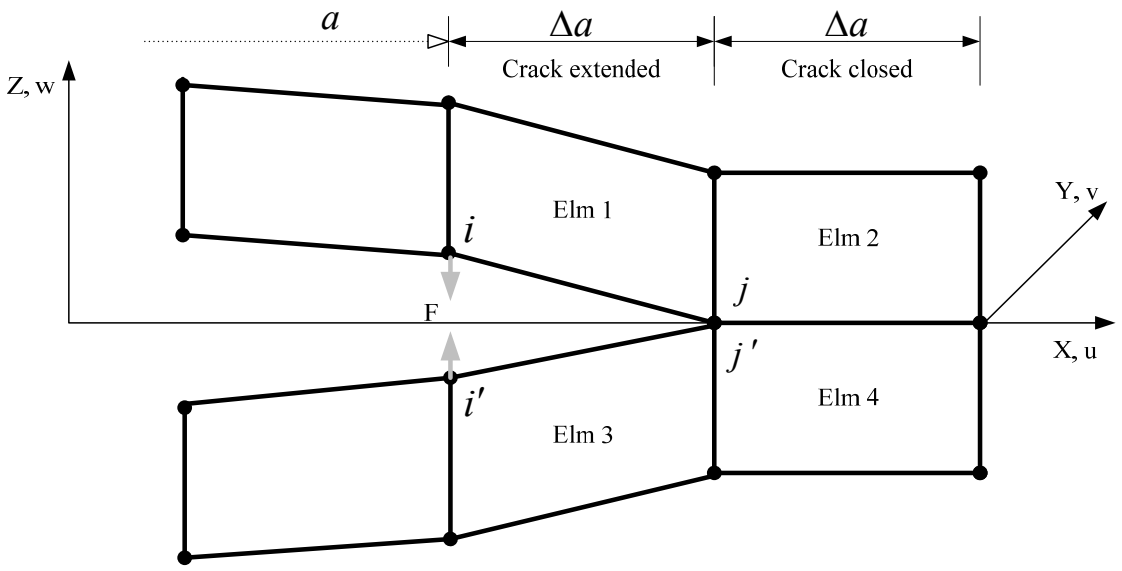

Figure 2.8 The 2D finite element model near crack tip.

Note that the finite element model used in this research used four-node cohesive elements within the two-dimensional plane analyses as shown in Figure 2.9.

The interfacial debonding elements composed of the non-linear constitutive law and combined a stress based formation with a fracture mechanics based formulation [35]. The cohesive constitutive law relates the traction, $\boldsymbol{\sigma_t}$ the displacement jumps, δ at the interface. Basically, softening models as the cohesive zone models shown in Figure 2.10 (point 3) can still transfer load after onset of separation, δ^0. For Mode I, II, and III crack growth behavior, when the interfacial normal or shear traction reach their corresponding interlaminar normal (tensile) or shear strengths, the resistance to deformation in the corresponding displacement mode is gradually reduced to zero, corresponding to an interface that is fully debonded. The elements in which softening (such as fiber bridging or matrix ductility) occurs are in the range of $\delta^0 < \delta < \delta^f$.

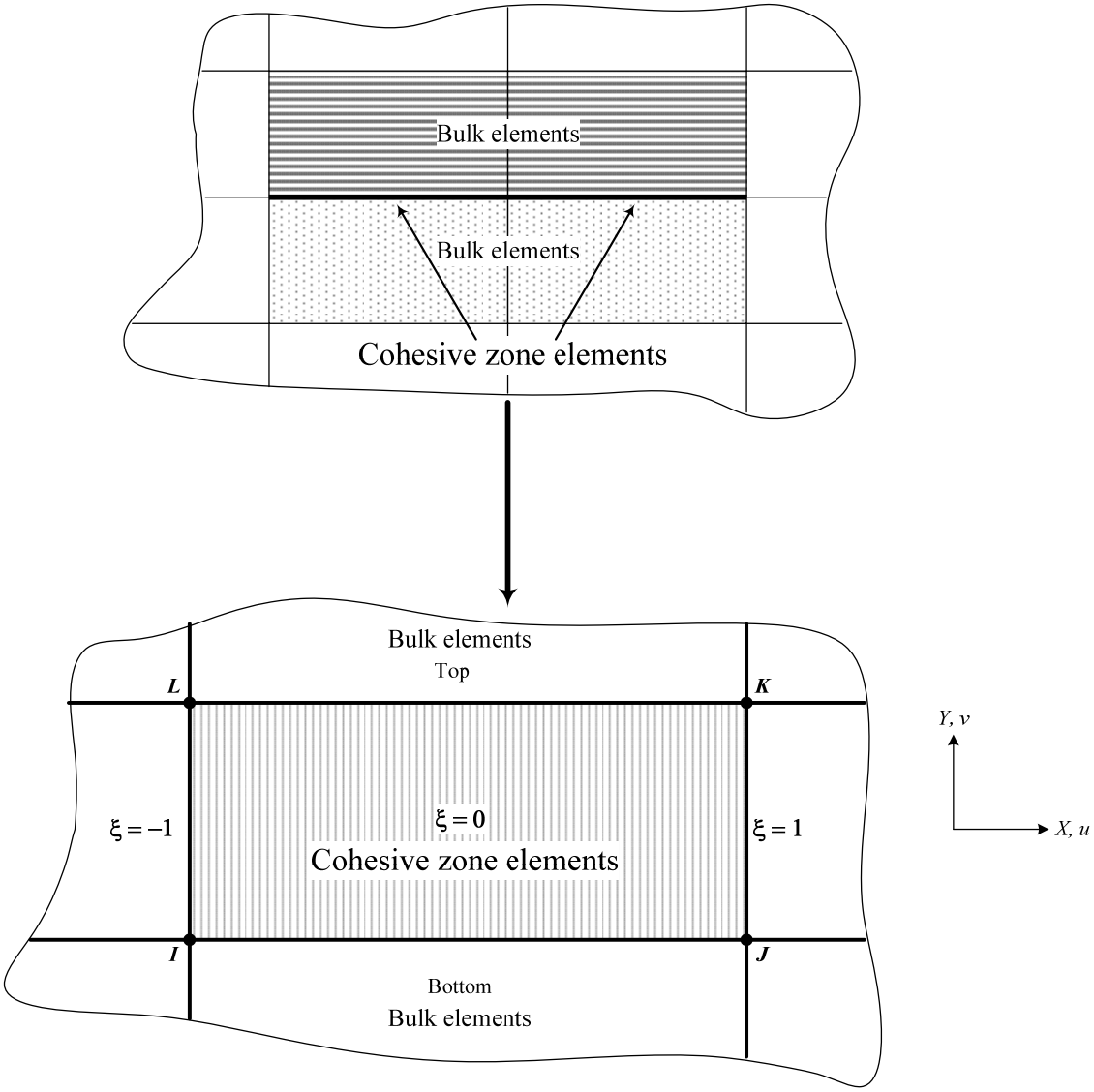

Figure 2.9 Four-node cohesive element (Undeformed).

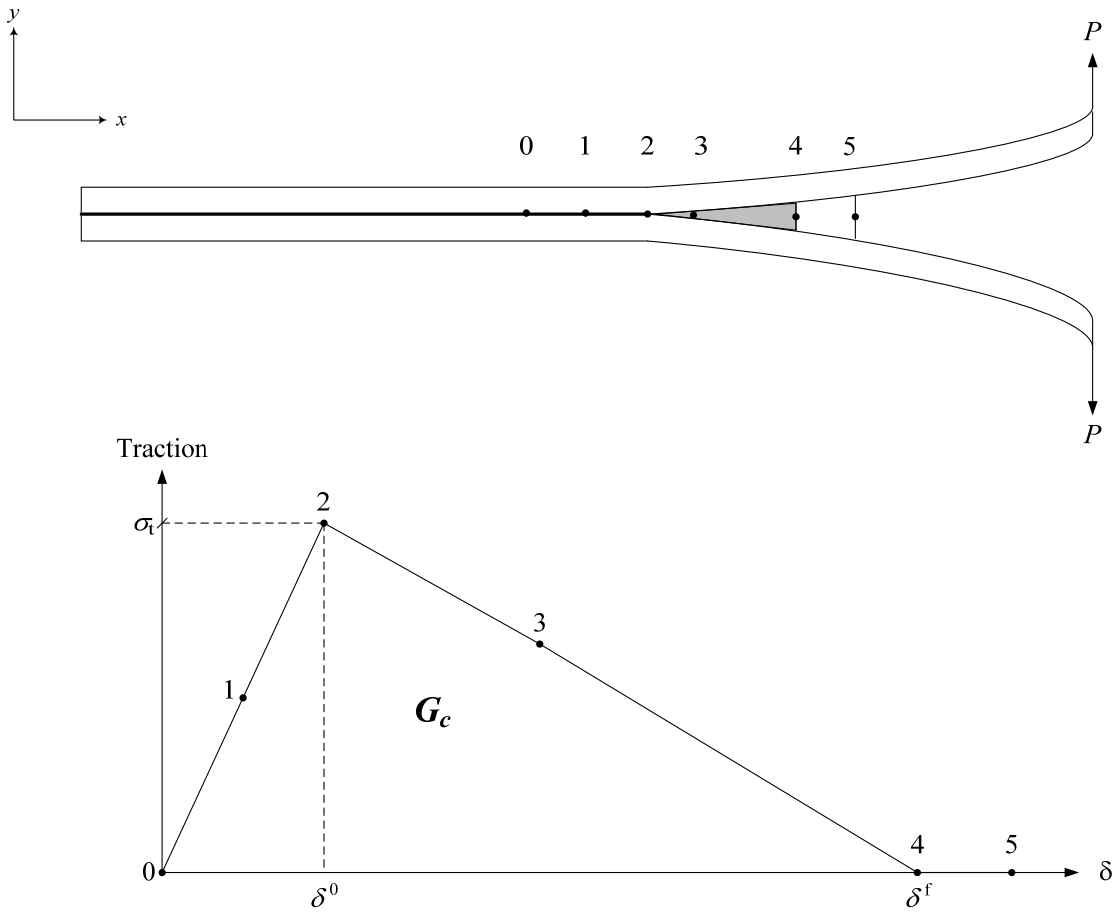

Figure 2.10 Cohesive zone decohesion model.

The area under the traction-displacement jump curves is the respective critical fracture energy, G_c for a particular mode (Mode I, II, or III). At the crack propagation the critical value of G, G_c is:

$$G_c = \int_0^{\delta^f} \boldsymbol{\sigma_t}(\boldsymbol{\delta}) d\boldsymbol{\delta} \tag{2.19}$$

where δ^f is the displacement jump at the fully interface failure that is shown in Figure 2.10. The penalty stiffness, *K,* is an arbitrarily large number selected such that the presence of undamaged cohesive elements does not introduce appreciable compliance to the structure [36]. The cohesive zone models use high penalty stiffness before delamination onset (point 1 in Figure 2.10) to prevent additional deformation. At point 5 in Figure 2.10, all the penalty stiffnesses became zero. Therefore, a crack is not able to transfer any more load. A bilinear cohesive law was assumed for each mode that the three - direction was perpendicular to the interface and that the interlaminar shear strength, τ^0_{shear} was independent of the shear direction [37]. Therefore, the displacement jumps of the onset for each mode (Mode I, II, and III) were:

$$\boldsymbol{\delta}_1^0 = \frac{\sigma_t^0}{K}$$

$$\boldsymbol{\delta}_2^0 = \frac{\tau^0_{shear}}{K} \tag{2.20}$$

$$\boldsymbol{\delta}_3^0 = \frac{\tau^0_{shear}}{K}$$

A constitutive law concerns the interfacial traction, σ_t and the displacement jump, $\boldsymbol{\delta}$ relationship in the local coordinate system. Bilinear cohesive law model, which was

shown in Figure 2.11 was explained by the following interfacial constitutive equation [35]. If $\boldsymbol{\delta} < \boldsymbol{\delta}^0$; elastic region, the traction across the interface kept increasing to maximum traction. The stress equation was defined as:

$$\sigma = \begin{bmatrix} K & 0 & 0 \\ 0 & K & 0 \\ 0 & 0 & K \end{bmatrix} \boldsymbol{\delta} = \boldsymbol{D\delta} \tag{2.21}$$

When $\boldsymbol{\delta}^0 \leq \boldsymbol{\delta} < \boldsymbol{\delta}^f$; softening region, the traction across the interface kept decreasing to zero and the two plies started to delaminate at the same time. The constitutive equation was defined as:

$$\sigma = (\boldsymbol{I} - \boldsymbol{D})\boldsymbol{E}_0\boldsymbol{\delta} \tag{2.22}$$

where $\boldsymbol{I}$ is the identity matrix and $\boldsymbol{E}_0$ is a diagonal matrix containing the initial (high) stiffnesses. The delamination started to propagate and accumulate at the interface that could also be defined by a parameter *d*. The value of *d* was equal to zero whenever no damage occurred. Then, it became equal to 1 when the interface was fully broken. If $\boldsymbol{\delta} \geq \boldsymbol{\delta}^f$; absolute debonding region, interface elements were completely destroyed and all the penalty stiffnesses went back to zero. When interpenetration was detected, reapplying the normal stiffness was typical of the solution procedures of contact problems using penalty methods in a constrained variational formulation [35].

Furthermore, the precision of the analysis relies on the penalty stiffness, *K* selected for the linear-elastic region of the constitutive equation. High values of the penalty stiffness can keep away from interpenetration of the crack faces but can lead to numerical problems, as well. Y. Mi et al. [38] calculated the penalty stiffness value for their study including 5.7×10^7 N/mm^3 .

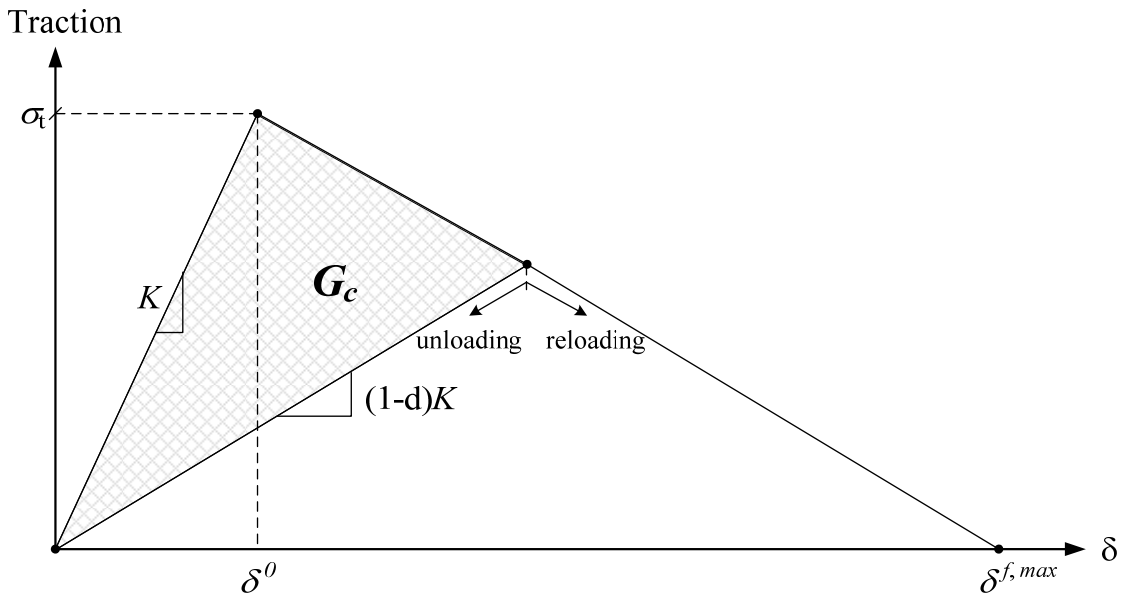

Figure 2.11 Bilinear cohesive law model.

Schellekens et al. [39] used 10^8 N/mm^3 for their work and some researchers shown the lower values for instant 10^7 N/mm^3 .

The particular solution that base on Reference [38] was primarily concerned with plane-strain simulation. It performed a preliminary computation using linear elastic fracture mechanics, LEFM to acquire the mode ratio. After that, the mode ratio value was used to calculate a value of G_c. For the interaction between Mode I and Mode II , the interaction relationship such as linear relationship given by Wu and Reuter [40] was used in this analysis.

$$\left(\frac{G_{\mathrm{I}}}{G_{\mathrm{I}c}}\right)+\left(\frac{G_{\mathrm{II}}}{G_{\mathrm{II}c}}\right)=1 \tag{2.23}$$

Then, the quadratic relationship was given in Reference [41] as following:

$$\left(\frac{G_{\mathrm{I}}}{G_{\mathrm{I}c}}\right)^2+\left(\frac{G_{\mathrm{II}}}{G_{\mathrm{II}c}}\right)^2=1 \tag{2.24}$$

The following two chapters describe the two principle features of this investigation: mechanical testing and finite element analysis. Results are summarized and conclusions presented in the final chapter.

CHAPTER 3

MECHANICAL TESTING

Mechanical testing was performed using cross-ply laminates (0° and 90° ply orientations) fabricated from IM7/8551-7A unidirectional carbon fiber/epoxy prepreg material. Two categories of mechanical testing were performed as part of this research. First, fracture mechanics testing was performed to determine the critical strain energy release rate, G_c for both Mode I and Mode II loading. The critical energy release rates measured were used as input for the cohesive elements in finite element analysis. The Double Cantilever Beam (DCB) tests method, ASTM D 5528 [42] was used for Mode I testing whereas the End-Notched Flexure (ENF) test, currently a proposed ASTM standard test [43], was used for Mode II testing. Secondly, static compression tests were performed to investigate layer waviness effects in cross-ply laminates. Cross-ply laminates containing wavy layers were fabricated using a single-step fabrication method. Single as well as multiple-nested wavy 0° layers were fabricated into otherwise wave-free laminates using previously developed procedures [3, 4, 10]. Static compression testing was performed using the NASA short block compression test fixture [10] to determine the effects of layer waviness on compression strength. In this chapter, both categories of mechanical testing are described, and test results are presented and discussed.

3.1 Mode I Double Cantilever Beam Testing

For determining the Mode I energy release rate, G_{Ic}, the ASTM D 5528 Double Cantilever Beam (DCB) test was used [42]. Following the standard procedure, DCB specimens were loaded by applying a constant displacement. G_{Ic} values were determined using the applied displacement, resulting load, and measured crack length. The energy release rate was determined by two following methods: the modified beam theory (MBT) method and the compliance calibration (CC) method.

3.1.1 Material and DCB Specimen Design

The material used throughout this DCB testing was the same IM7/8551-7A carbon/epoxy prepreg material used to investigate layer waviness effects in cross-ply laminates. Mechanical properties of this material, which were obtained from Hercules Aerospace Products [44], are given in Table 3.1 and Table 3.2. The cross-ply laminates tested consisted of 15 layers: 8 plies of 90° layers and 7 plies of 0° layers. Each layer consisted of two 0.127 mm thick plies of prepreg tape. A total of 7 DCB specimens were tested at room temperature/ambient conditions. The DCB specimen geometry is shown in Figure 3.1 and details of the specimen dimensions are listed in Table 3.3. Since the crossply panels used for DCB specimens did not contain an initial delamination produced during manufacturing, an initial crack was produced by pressing a thin knife blade into the laminate at the desired through-the-thickness location and into the laminate a desired length. The resulting crack length, a_0, was approximately 63.5 mm. As shown in Figure 3.1, this initial crack length consisted of an initial delamination length of approximately 50.8 mm plus the extra length of 12.7 mm required for bonding the loading hinges.

Table 3.1 Material properties of IM7/8551-7A.

Material Property	**Value (GPa)**
E_1	153.753
E_2	8.894
E_3	8.894
ν_{12}	0.30
ν_{13}	0.30
ν_{23}	0.34
G_{12}	5.46
G_{13}	5.46
G_{23}	3.316

Table 3.2 Strength properties of IM7/8551-7A.

Material Property	**Value (MPa)**
X_T	2230
X_C	1520
Y_T	62.4
Y_C	117
S	82.7

Table 3.3 DCB specimen dimensions.

IM7/8551-7A	***L*** (mm)	***b*** (mm)	***h*** (mm)	a_0 (mm)
	127	25.4	3.81	50.8

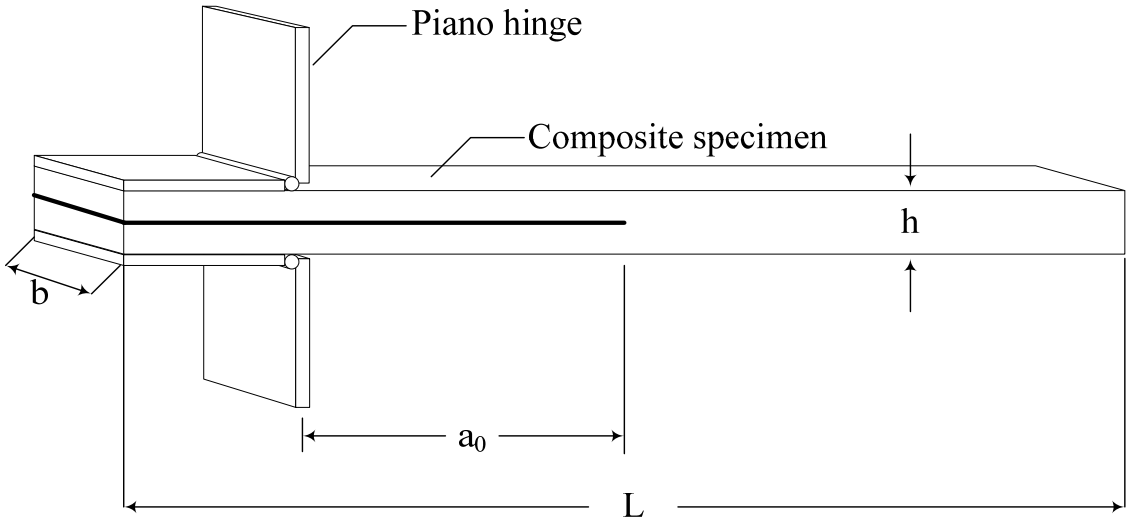

Figure 3.1 Double Cantilever Beam Specimen.

The piano hinges were adhesively- bonded with room temperature curing epoxy adhesive to the laminates.

3.1.2 DCB Experimental Procedure

The specimens were tested on a universal testing machine (Instron 4303) using a 22,241 N load cell. One edge of each specimen was painted just in the front of the initial crack with white typewriter correction fluid to assist in visual inspection of crack propagation as shown in Figure 3.2. Thin vertical lines were marked at an interval of 5.0 mm on the painted surface. The hinges of the specimen were mounted in the grips of the loading machine as shown in Figure 3.3, ensuring that the specimen was properly aligned and centered. An optical microscope was placed as shown in Figure 3.3 for use in observing the movement of the delamination front. Load was applied to the specimen under displacement control.

A constant crosshead displacement rate of 1.02 mm/min. was used. During loading, the applied load, P and crosshead displacement, δ were recorded by the test machine. The optical microscope was used to capture the images of the delamination front. The propagation was visually observed from the initial crack tip. At the beginning point of delamination, the position was recorded as a_0. During crack propagation, the opening displacement and the load were recorded at each 5.0 mm interval of crack growth.

3.1.3 Data Reduction Techniques

Following testing, the energy release rate was calculated using two methods: the Modified Beam Theory (MBT) method and Compliance Calibration (CC) method.

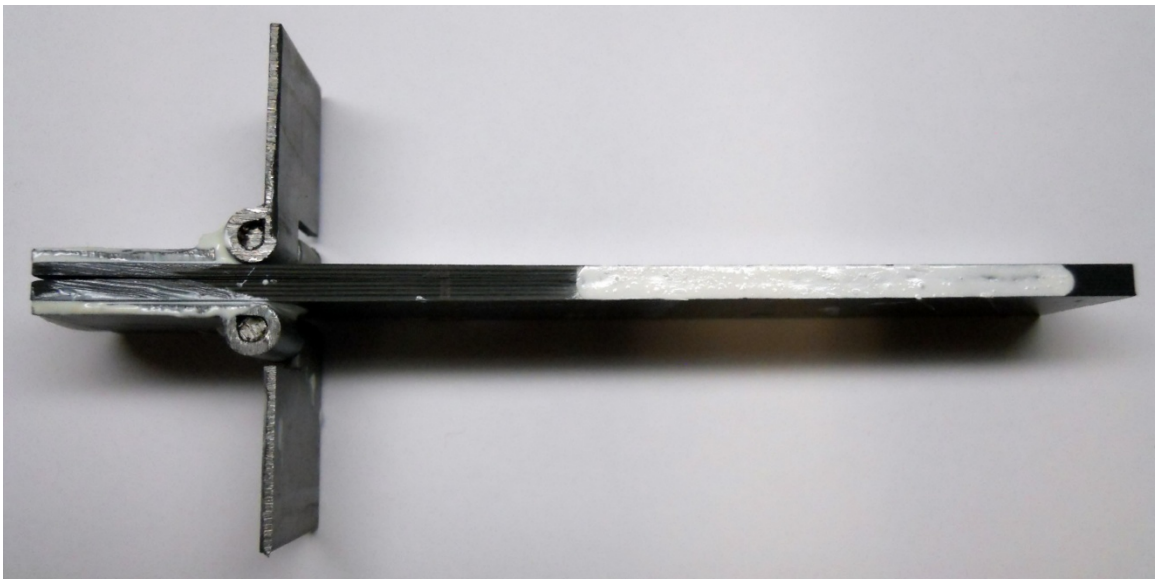

(a) DCB test specimen with white typewriter correction fluid.

(b) Magnified view of DCB test specimen.

Figure 3.2 DCB test specimen.

Figure 3.3 DCB test specimen during testing.

For most of the DCB specimen tested, the MBT method provided the most conservative G_{Ic} values [45], and thus was used for all tests performed. In the MBT method, [46] the cantilever beam is assumed to be perfectly built-in (that is, rotation cannot occur at the delamination front). Beam theory is used to calculate the resulting G_{Ic} associated with crack growth as [42]

$$G_{Ic} = \frac{3P\delta}{2ba}, \tag{3.1}$$

where P is the load, δ is the applied displacement, b is the width of the specimen, and a is the delamination length. Since the cantilever beam is not perfectly built-in (rotation can occur at the delamination front), Equation 3.1 may over-estimate the G_{Ic} value. In order to provide a more accurate calculation, a slightly longer delamination length, $a + |\Delta|$ may be used. The ratio of the displacement to the applied load, δ/P is compliance, C. A least squares fit of the cube root of the compliance, $C^{1/3}$, as a function of the delamination length, a, is generated as shown in Figure 3.4. The intercept of this line on the x-axis is recorded as the increase in delamination length, Δ.

Following this approach, the value for G_{Ic} can be calculated as [46]

$$G_{Ic} = \frac{3P\delta}{2b(a + |\Delta|)}, \tag{3.2}$$

For the compliance calibration (CC) method [47], a least squares plot of log (δ_i/P_i) versus log a_i is generated using the displacements and load corresponding to the visually observed delamination onset values and all of the propagation values. The slope of this line $(\Delta y/\Delta x)$, plotted as shown in Figure 3.5 is recorded as n.

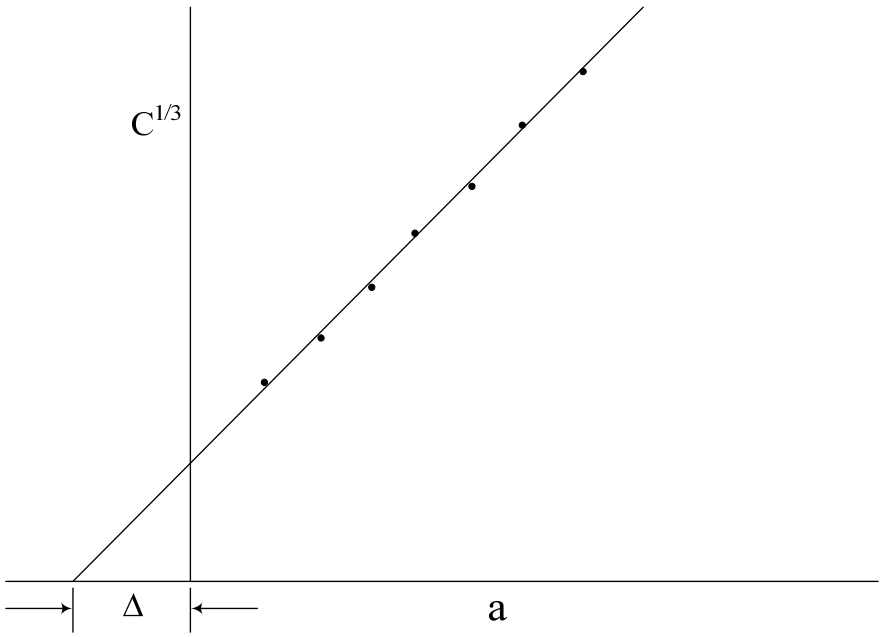

Figure 3.4 Modified beam theory (MBT).

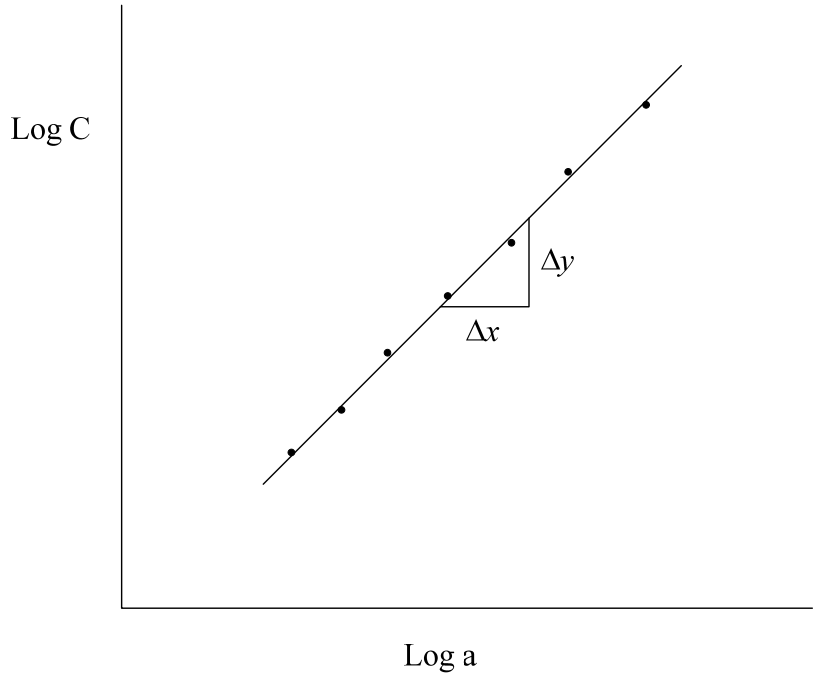

Figure 3.5 Compliance calibration (CC).

Thus, G_{Ic} can be calculated using the expression [47]

$$G_{Ic} = \frac{nP\delta}{2ba}, \tag{3.3}$$

3.1.4 Results of DCB Testing

The load versus displacement plots from the seven DCB tests performed on cross-ply laminates in this investigation are shown in Figure 3.6 to Figure 3.12. From the figures shown, all specimens showed similar load versus displacement responses, although the amplitudes of the peak load for each specimen were different.

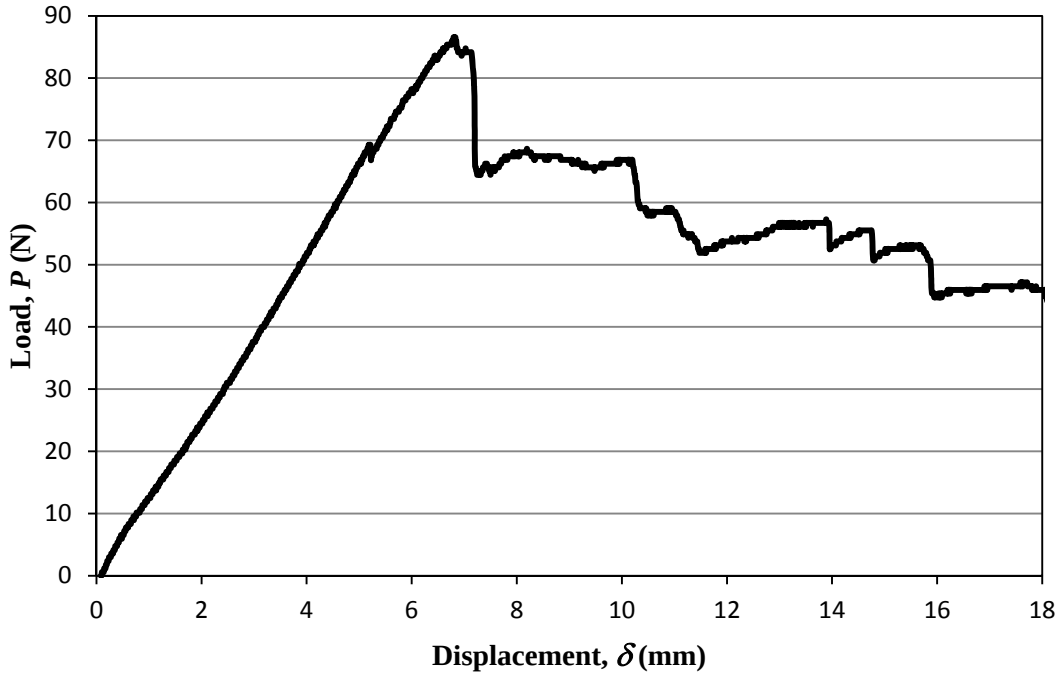

Figure 3.6 Load versus displacement plot of DCB specimen No.1.

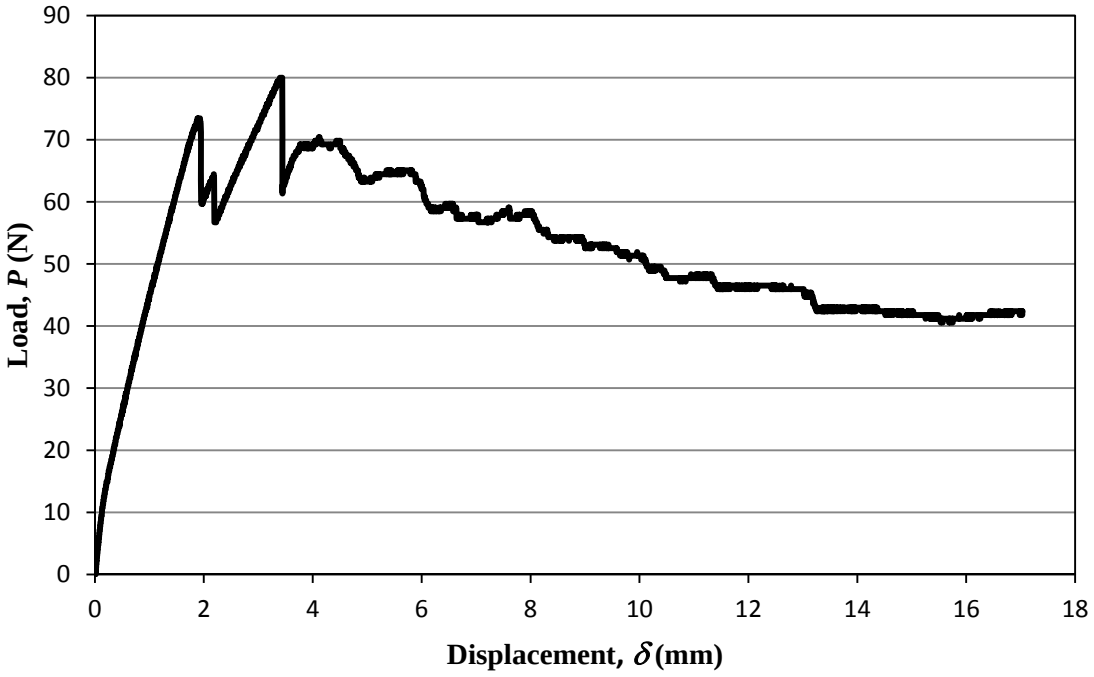

Figure 3.7 Load versus displacement plot of DCB specimen No.2.

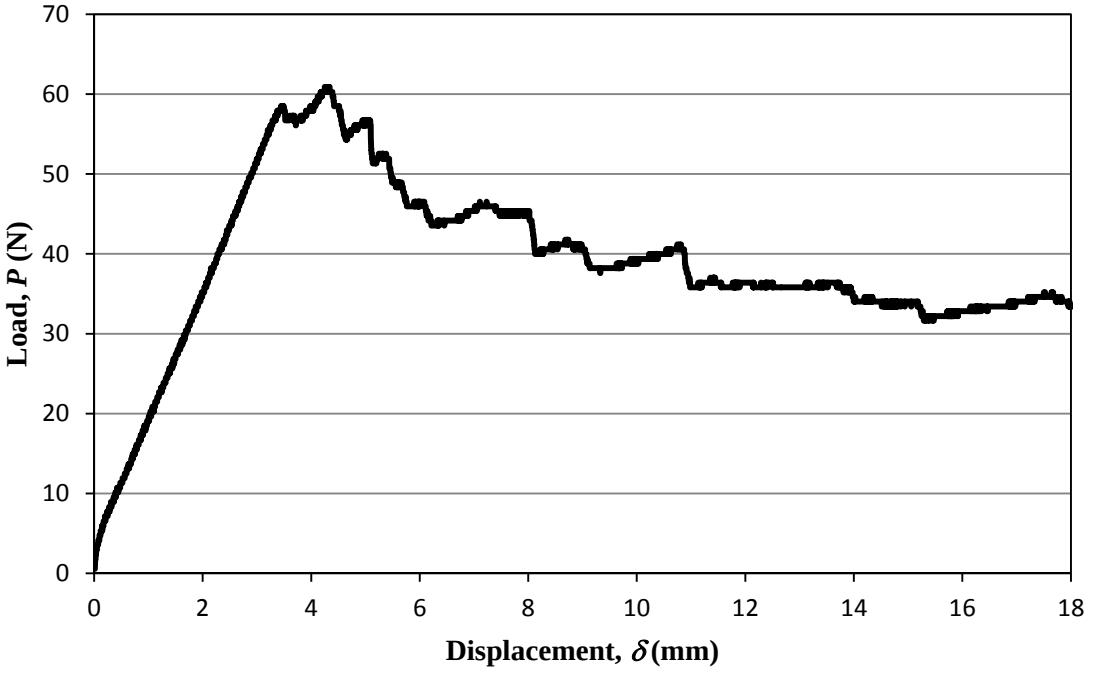

Figure 3.8 Load versus displacement plot of DCB specimen No.3.

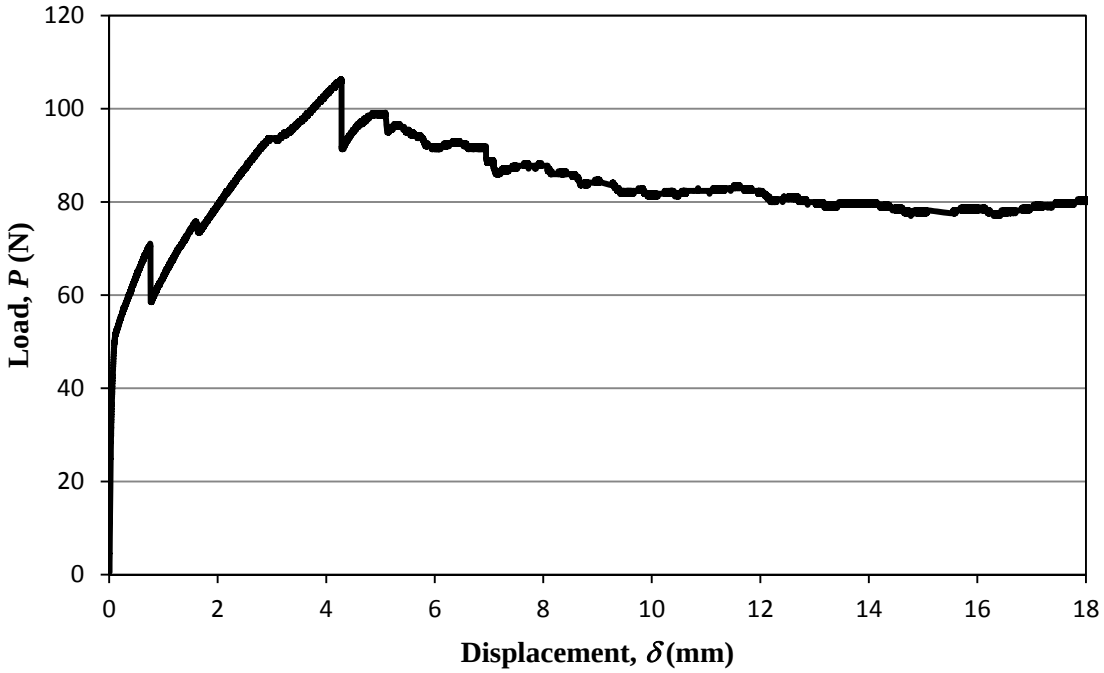

Figure 3.9 Load versus displacement plot of DCB specimen No.4.

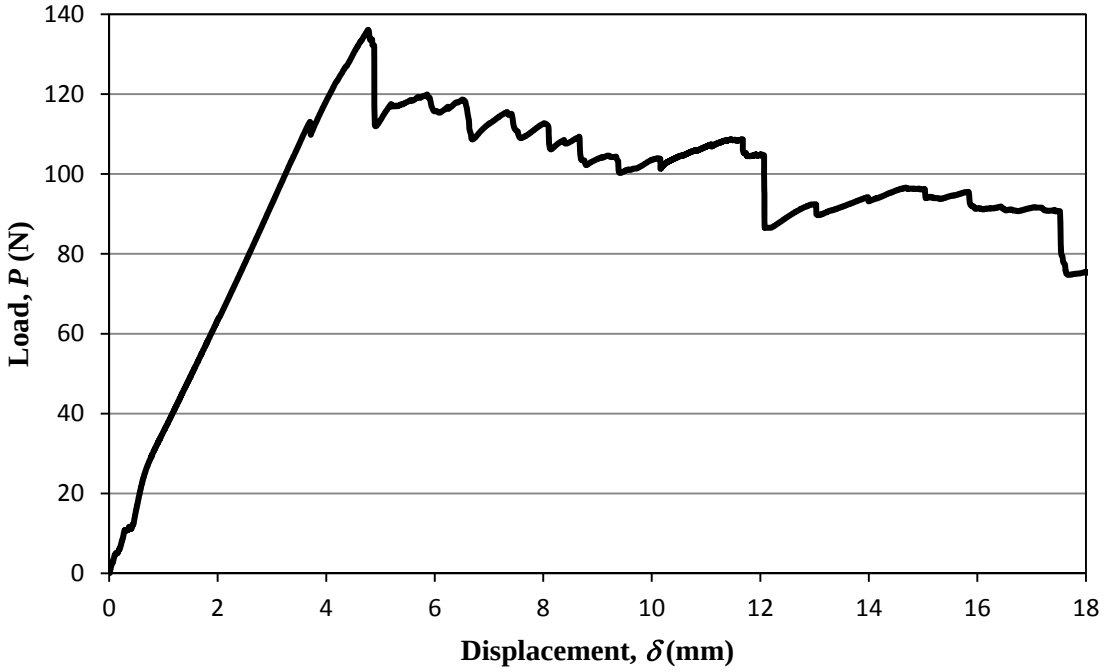

Figure 3.10 Load versus displacement plot of DCB specimen No.5.

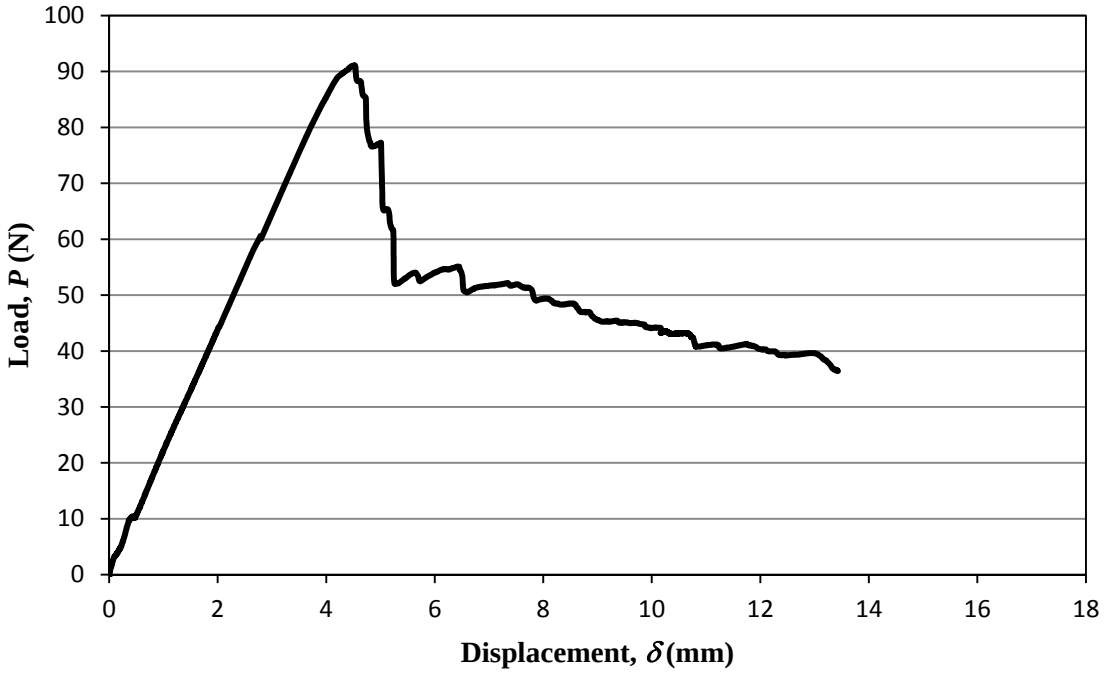

Figure 3.11 Load versus displacement plot of DCB specimen No.6.

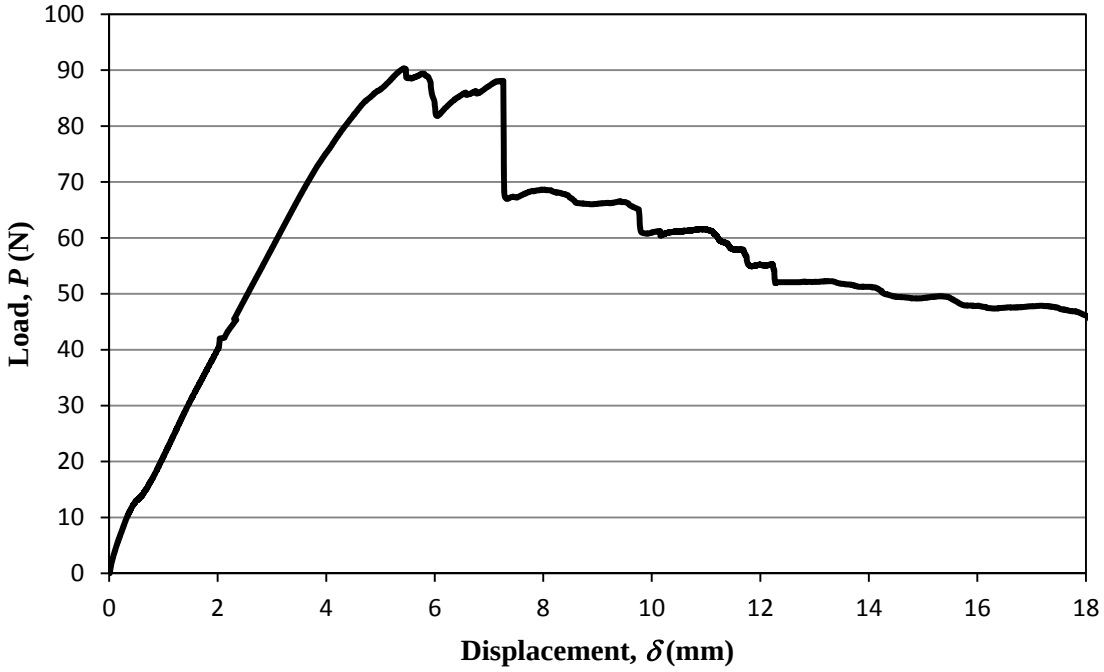

Figure 3.12 Load versus displacement plot of DCB specimen No.7.

The lowest peak load values (specimens 2, 3, and 6) were obtained when the crack propagated through only the 0° layer as shown in Figure 3.13(a). Intermediate peak load values (specimens 1, 4, and 7) were obtained as the crack propagated through a combination of 0° and 90°layers as shown in Figure 3.13(b). The highest peak load value (specimen 5) was obtained when the crack propagated through 90°layers as shown in Figure 3.13(c).

The energy release rates, G_{Ic} measured from the seven DCB specimens are shown in Figure 3.14(a) and Figure 3.14(b) as the results of MBT method and CC method, respectively. From the MBT method, the energy release rates for the different crack propagation paths as described in Figure 3.13(a) to 3.13(c) show different average G_{Ic} values within the range of 0.343 to 0.755 KJ/m^2. For specimen 5, the average value of G_{Ic} is 0.901 KJ/m^2, which represents the upper bound of all specimens.

From the CC method, the energy release rates show average values ranging from 0.342 to 0.729 KJ/m^2. For specimen 5, the average value of the energy release rates is 0.915 KJ/m^2, the upper bound of all specimens. The average G_{Ic} value obtained from the seven DCB specimens was 0.589 KJ/m^2. Values of G_{I}obtained from each specimen using the MBT and CC method are shown in Figure 3.15. These cross-ply composite laminates experienced crack jumping and extensive fiber bridging during crack propagation as shown in Figure 3.16. In addition to the different crack paths described above, such fiber bridging is believed to contribute to the significant scatter in G_{Ic} values obtained.

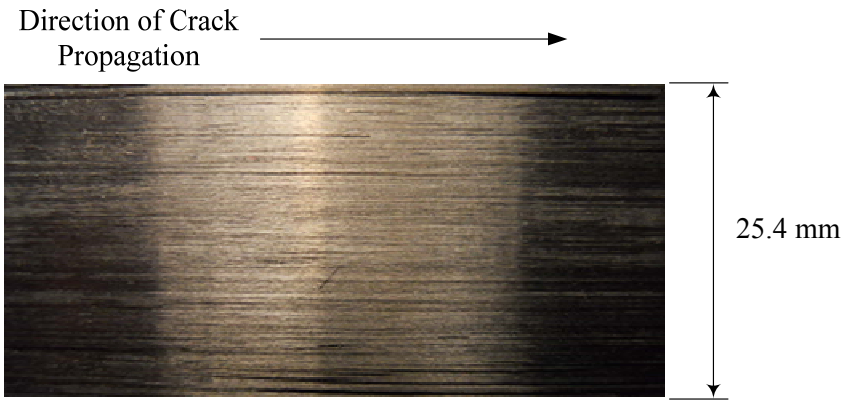

(a) Crack propagation through a 0° layer.

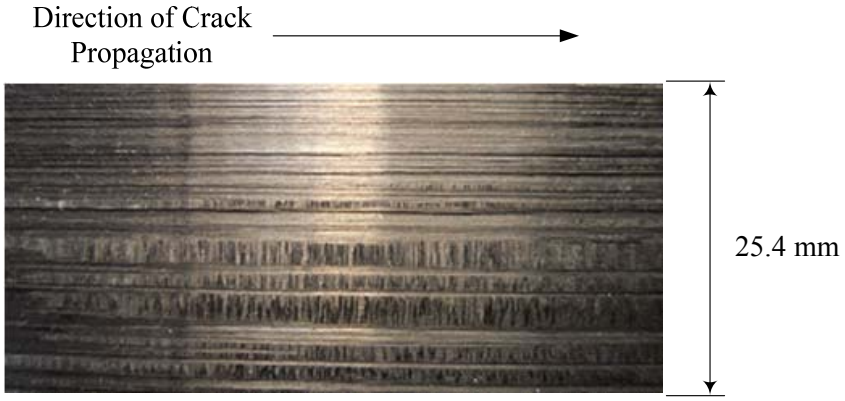

(b) Crack propagation through a combination of 0° and 90° layers.

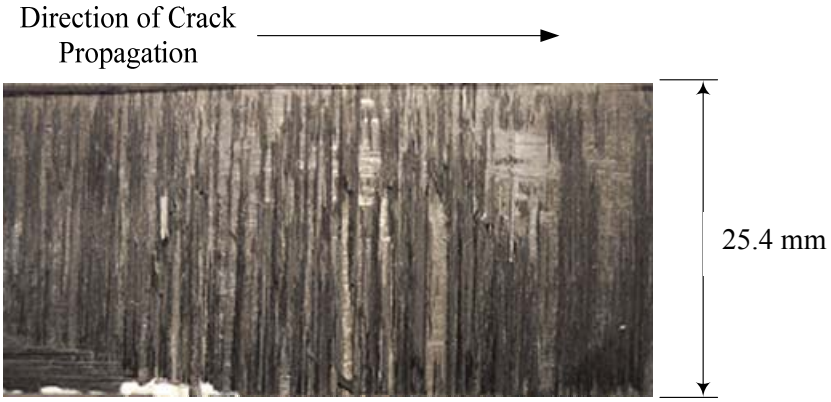

(c) Crack propagation through a 90° layer.

Figure 3.13 Classifications of crack propagation in DCB specimens.

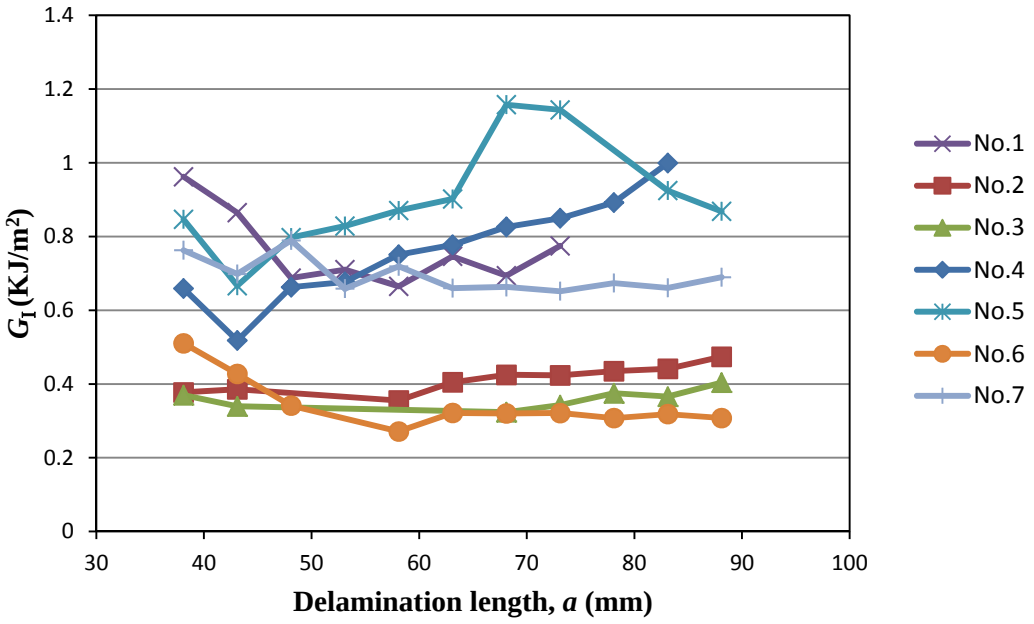

(a) R-curves obtained from MBT method.

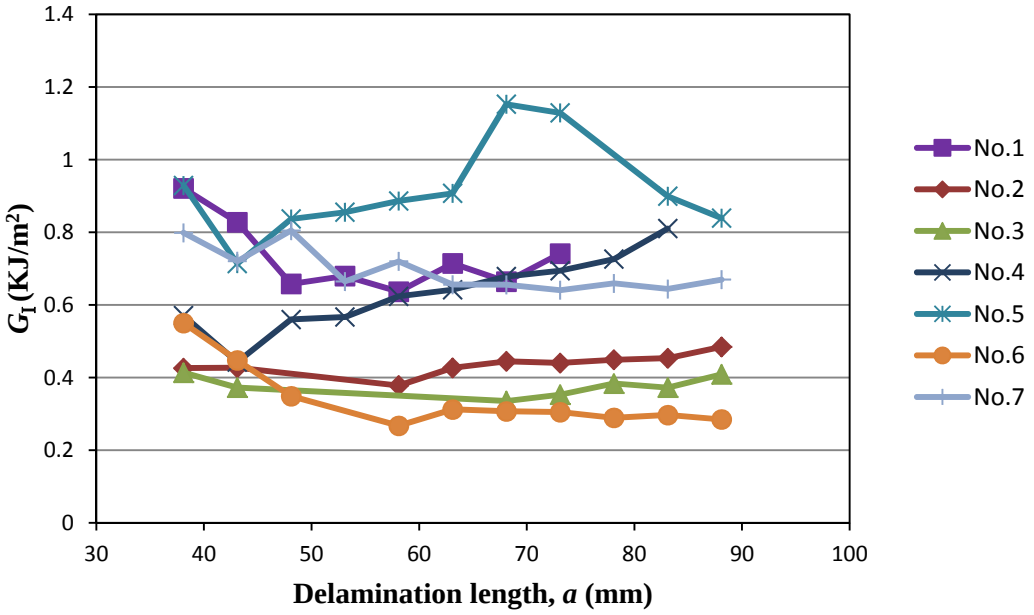

(b) R-curves obtained from CC method.

Figure 3.14 DCB R-curves.

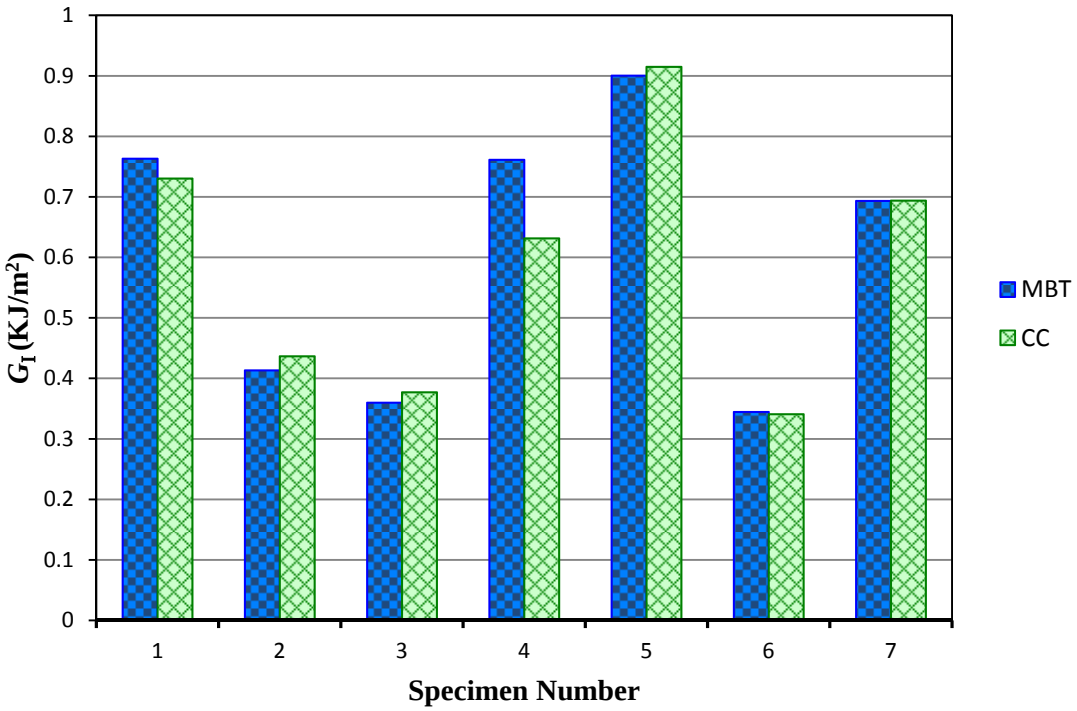

Figure 3.15 Average G_I values from each DCB specimen.

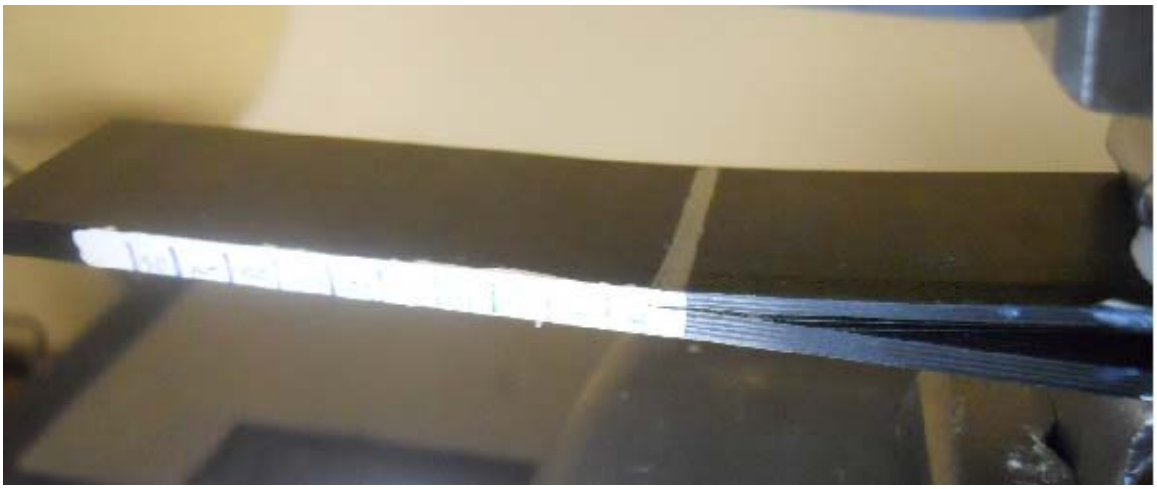

Figure 3.16 Fiber bridging.

3.2 Mode II End-Notched Flexure testing

The objective of this test was to obtain the Mode II critical strain energy release rate, G_{IIc} of the IM7/8551-7A carbon/epoxy composite material. Mode II is defined as a pure sliding mode, produced from shear loading. To measure G_{IIc}, the End Notched Flexure (ENF) test is commonly used. This test method has been used by many researchers and has been comprehensively studied by the ASTM D-30 Committee as a candidate for ASTM standardization. A draft standard of this ENF test method was used as a guide in this investigation for determining G_{IIc} values [48]. The compliance calibration technique was employed to calculate G_{IIc} values from the ENF test.

3.2.1 Material and ENF Specimen Design

Similar to Mode I testing, IM7/8551-7A carbon/epoxy cross-ply laminates were used for ENF testing. Mechanical properties of this material that were obtained from Hercules Aerospace Products [44] are given in Table 3.1 and Table 3.2. The cross-ply laminates used for the ENF specimens were identical to those used for the Mode I DCB specimens. The ENF testing that was performed in this work used a three-point flexure configuration as shown in Figure 3.17. Dimensions of specimen tested were selected with the assistance of the procedure described in the draft ASTM standard [48], and are shown in Table 3.4.

The preparation of the ENF specimens was similar to that of the DCB specimens. The initial crack lengths were produced by pressing a thin cutting blade into the specimen at the desired location. The specimen width, B and thickness $2h$ were measured and typewriter correction fluid was applied to the specimen edges (Figure 3.18) to aid in crack tip observation and compliance calibration markings.

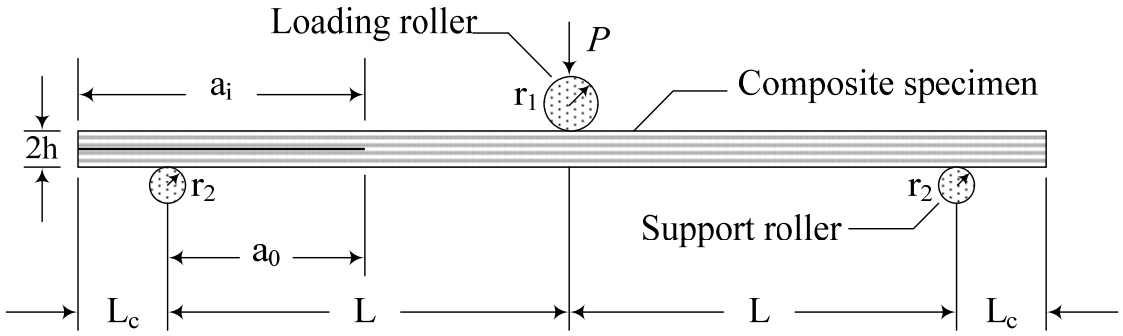

Figure 3.17 Schematic of ENF test.

Table 3.4 ENF Specimen Geometry.

Parameter	**Value or Range of value**
Specimen thickness, ***2h***	3.38 – 4.70 mm
Specimen half-span, ***L***	50.8 mm
Distances from roller center to the end, $\boldsymbol{L_c}$	≥ 15.2 mm
Delamination length, $\mathbf{a_0}$	30.5 mm
Specimen width, ***B***	19.1 – 25.4 mm

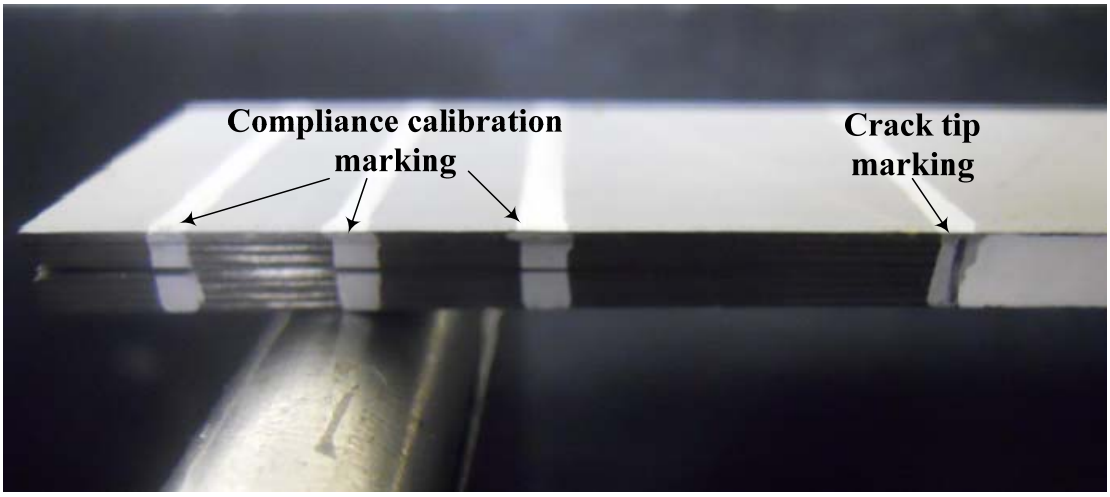

Figure 3.18 Compliance calibration and crack tip marking.

The specimen edges were marked with three vertical compliance calibration marking (within the cracked region) at locations of 20.3, 30.5, and 40.6 mm from the tip of the delamination.

3.2.2 ENF Experimental Procedure

Three ENF specimens were tested on an Instron 4303 universal testing machine. Specimens were placed in the three-point flexure fixture with the longitudinal axis of the specimen aligned to the base and were perpendicular to the loading rollers as shown in Figure 3.19. The Compliance Calibration (CC) method was performed to obtain the Mode II critical strain energy release rate, G_{IIc}. This data reduction technique uses the relationship between specimen compliance and delamination length that is determined prior to crack growth testing [48]. This relationship is acquired by measuring specimen compliance at three simulated crack lengths by sliding the specimen across the support roller.

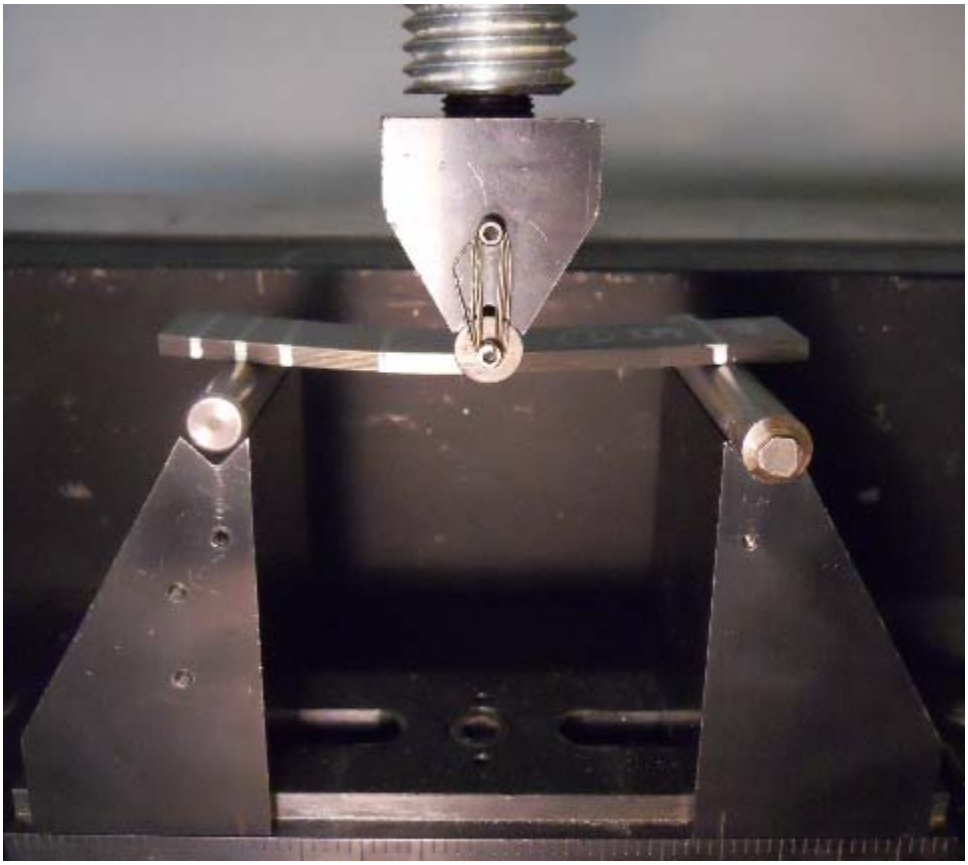

Figure 3.19 ENF test specimen during testing.

Displacement loading for both compliance calibration and crack growth tests were performed at an applied displacement rate between 0.102 to 0.787 mm/min. For unloading, the rate was increased up to 1.60 mm/min. To prevent crack propagation during the compliance calibration testing, the maximum loads were limited to 50% of the predicted values for crack growth, P_c. These critical loads for each crack length can be calculated using classical beam theory (CBT) as [49]

$$P_c = \frac{4B}{3a_0}\sqrt{G_{IIc}E_{1f}h^3}, \tag{3.4}$$

where B is specimen width, $a_0$is delamination length, h is specimen half-thickness, and E_{1f} is the flexural modulus. The flexural modulus can be obtained from [49]

$$E_{1f} = \frac{L^3}{4ABh^3}, \tag{3.5}$$

where A is the compliance calibration coefficient obtained from testing and L is the specimen half-span. Load was applied to the specimen until 50% of P_c, and the specimen was subsequently unloading. Next the specimen was repositioned in the fixture to the next CC marking, and reloaded to 50% of the new P_c value. Following the compliance calibration testing, the specimen was repositioned in the fixture to produce an initial crack length a_0 = 30.5 mm and load was applied until the delamination advanced. The delamination advance was visually observed and detected by a drop in load on the load vs. displacement plot.

3.2.3 Data Reduction Techniques

There are several data reduction methods which have been applied for the ENF test, including: CBT (Classical Beam Theory), MBT (Modified Beam Theory), TBT (Timoshenko Beam Theory), and CC (Compliance Calibration). The CC method was employed for this study. The determination of the Mode II strain energy release rate, G_{IIc} requires a plot of the load-displacement (P vs δ). The compliance at each prescribed initial crack length was obtained by a least squares linear regression analysis, determined from the slope of the load-displacement curve. The three measured compliance values are plotted versus crack length cubed as shown in Figure 3.20.

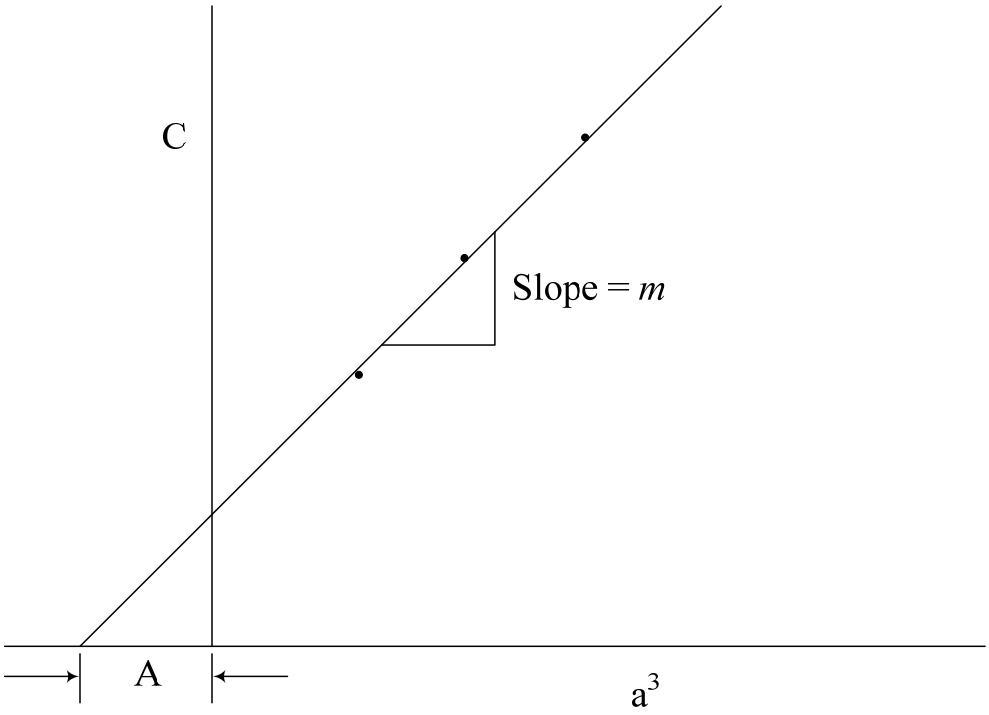

Figure 3.20 Schematic of compliance calibration method.

The least-squares linear regression analysis of compliance can be determined by the expression [48]

$$C = A + ma^3, \tag{3.6}$$

where C is compliance, A is the intercept, and m is the slope of the plot as shown in Figure 3.20. Next, the Mode II energy release rate G_{IIc} is calculated using the expression [48]

$$G_{IIc} = \frac{3mP_{Max}^2 a_0^2}{2B}, \tag{3.7}$$

where P_{Max} is the maximum load from the fracture test, a_o is the delamination length (30.5 mm), and B is the specimen width.

3.2.4 Results and Analysis

Room temperature ENF testing was performed using a total of three cross-ply specimens. The compliance calibration test results from the three specimens are shown in Figure 3.21. For fracture testing, the specimens were positioned such that the initial crack length was a_o = 30.5 mm. The applied displacement was increased until the delamination advanced. Figure 3.22 to Figure 3.24 show representative load versus displacement plots obtained from the three ENF specimens with an initial delamination length of 30.5 mm. The curves show a relatively linear relationship until the onset of delamination growth. At this point, the load immediately drops and the delamination grows in an unstable manner.

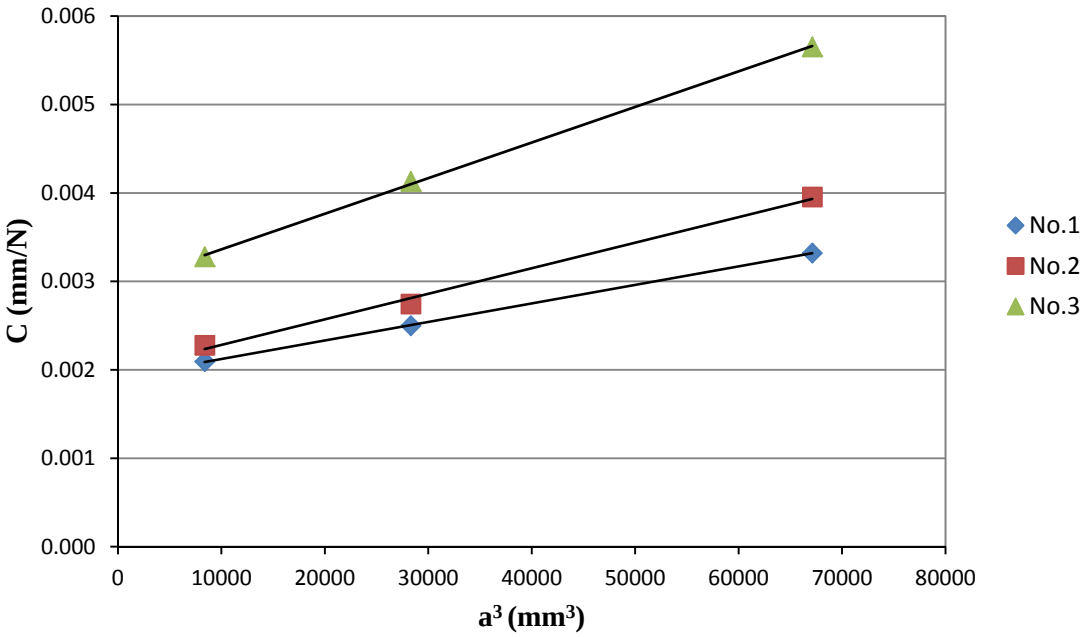

Figure 3.21 ENF compliance calibration test results.

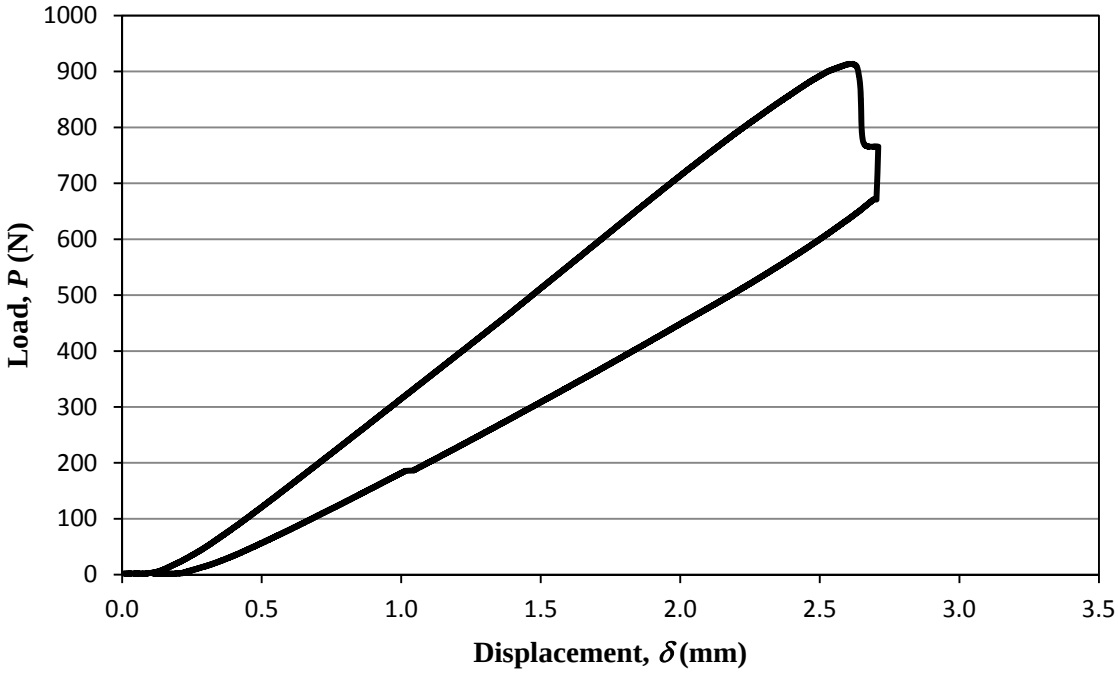

Figure 3.22 Load vs. displacement plot of ENF specimen No.1.

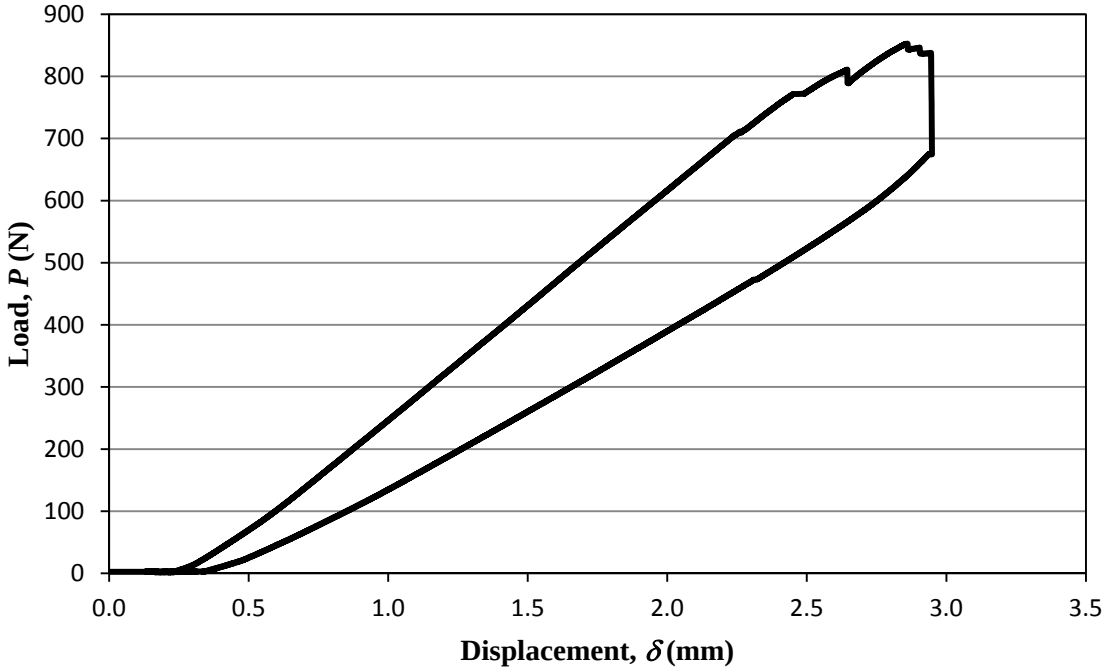

Figure 3.23 Load vs. displacement plot of ENF specimen No.2.

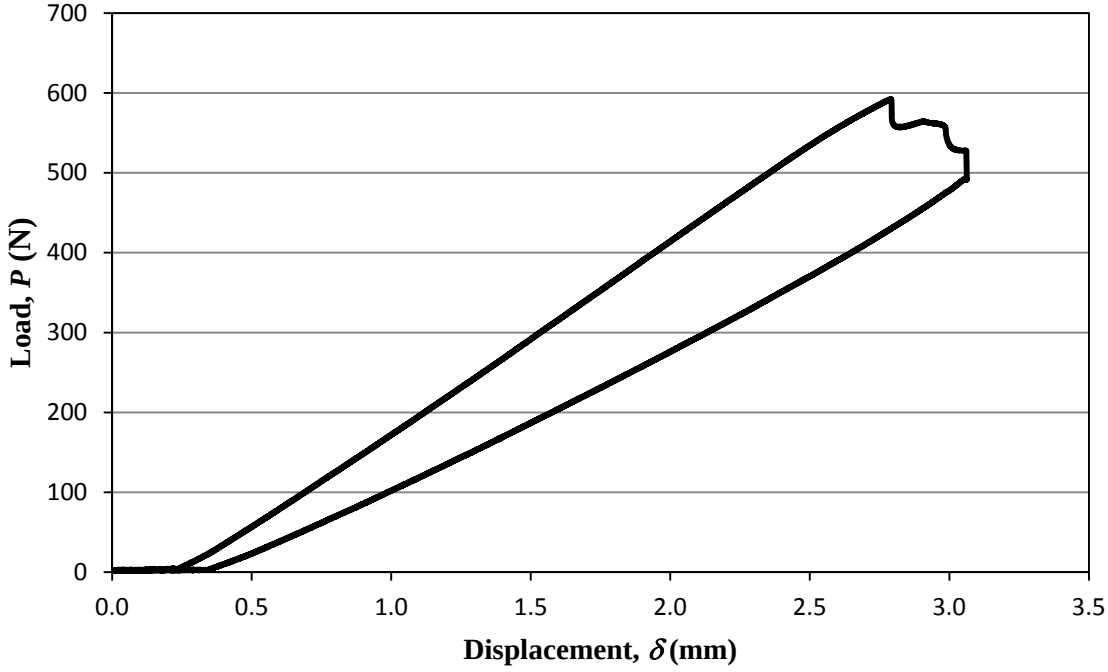

Figure 3.24 Load vs. displacement plot of ENF specimen No.3.

Figure 3.25 show the G_{II} values measured from the three tested specimens. The candidate fracture toughness measured of the fracture test is 1.03 KJ/m^2, 1.18 KJ/m^2, and 0.90 KJ/m^2 for ENF specimen No.1, No.2, and No.3 respectively. Thus, the averaged value of the Mode II critical energy release rate of IM7/8551-7A was 1.04 KJ/m^2. Moreover, this G_{IIc} value is in general agreement with the G_{IIc} value obtained for IM7/8551-7 using a precracked specimen, 1.15 KJ/m^2 [50]. This measured G_{IIc} value was used as input in the finite element models.

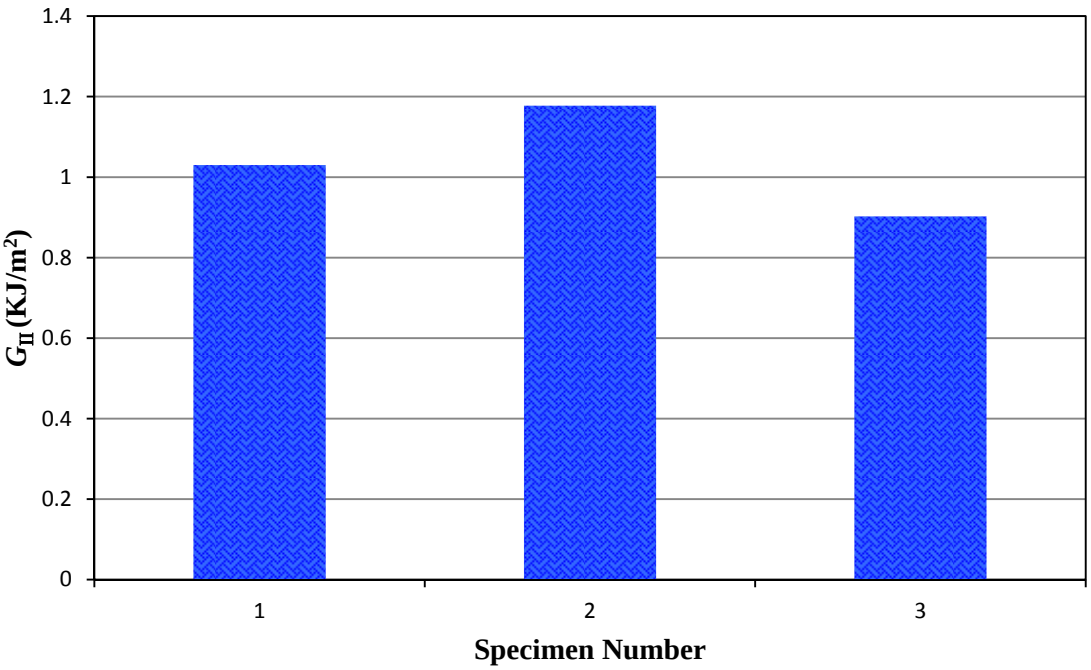

Figure 3.25 Average G_{II} values from each ENF specimen.

3.3 Static Compression Testing

In addition to the progressive damage modeling described in Chapter 4, static compression testing was performed to investigate additional formations of layer waviness discussed in this section. Initially, the set of wavy layers was placed at the laminate midplane. The initial objective was to investigate laminates where the wavy 0° layers represent a smaller fraction of the total number of 0° layers than in previous testing. There are two reasons for considering laminates with relatively small fractions of wavy 0° layers. First, layer waviness occurs most often in thick laminates, and thus the use of laminates with a greater number of nonwavy 0° layers better approximates these thick laminates. Secondly, the use of laminates with a smaller percentage of 0° layers with waviness may result in an observable failure progression. Since the wavy 0° layers are a smaller fraction of the total number of 0° layers, it was believed that an initial failure in the region of waviness may not result in ultimate laminate failure, and thus a progressive failure may be observed during testing. This type of observation provides important information in validating the progression of damage associated with layer waviness under compression loading.

3.3.1 Single-Step Fabrication Procedure

To fabricate a single wavy 0° layer into a cross-ply laminate, two thin strips of the IM7 carbon/epoxy prepreg material were removed from the adjacent 90° plies as shown in Figure 3.26 [3, 4]. One strip was formed into a cylinder and placed above the 0° layer and the other strip was split in half, formed into two small cylinders, and placed below the 0° layers.

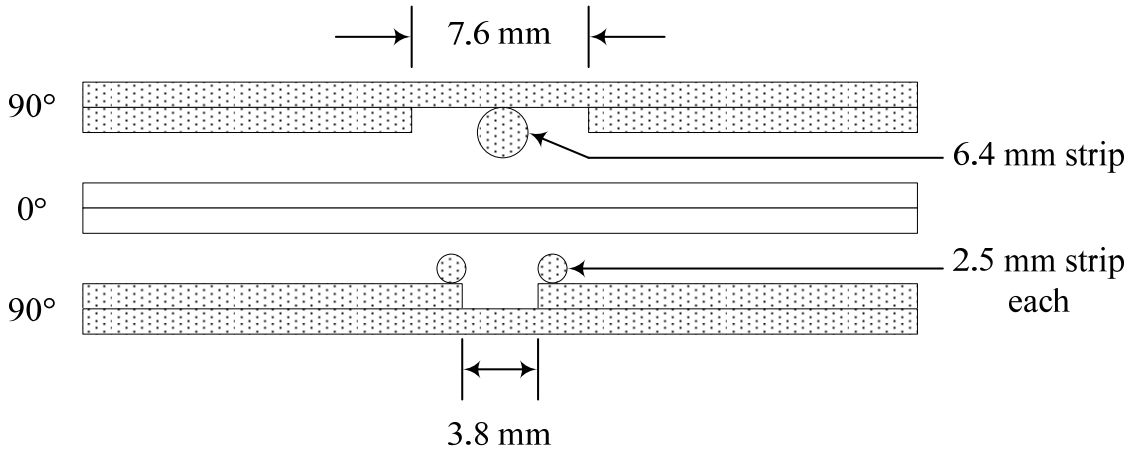

Figure 3.26 Fabrication of single wavy 0° layer.

The entire composite laminate was then placed into a 152 x 152 mm steel mold and cured in a heated press. The cure cycle consisted of applying 340 kPa of pressure and the temperature was increased to 120 °C. After 30 min at 120 °C, the temperature was increased to 180 °C, while the pressure was increased to 550 kPa and held for 3 hours.

Multiple nested wavy 0° layers were fabricated in a similar method as shown in Figure 3.27 [3]. Two thin strips of the carbon/epoxy prepreg material were removed from the adjacent 90° plies, rolled into cylinders, and then placed in similar positions above and below the three 0° layers. The remaining 0° and 90° plies were assembled and placed into the mold and the laminate was then cured in a heated press.

A total of six 152 x 152 mm laminates were fabricated: five with layer waviness and one without as show in Table 3.5. As an example of the notation used to describe the laminate configuration, consider the laminate denoted as $[90_2/0_2/90_2/0_2/90_2/\bar{0}_{2w}]_s$.

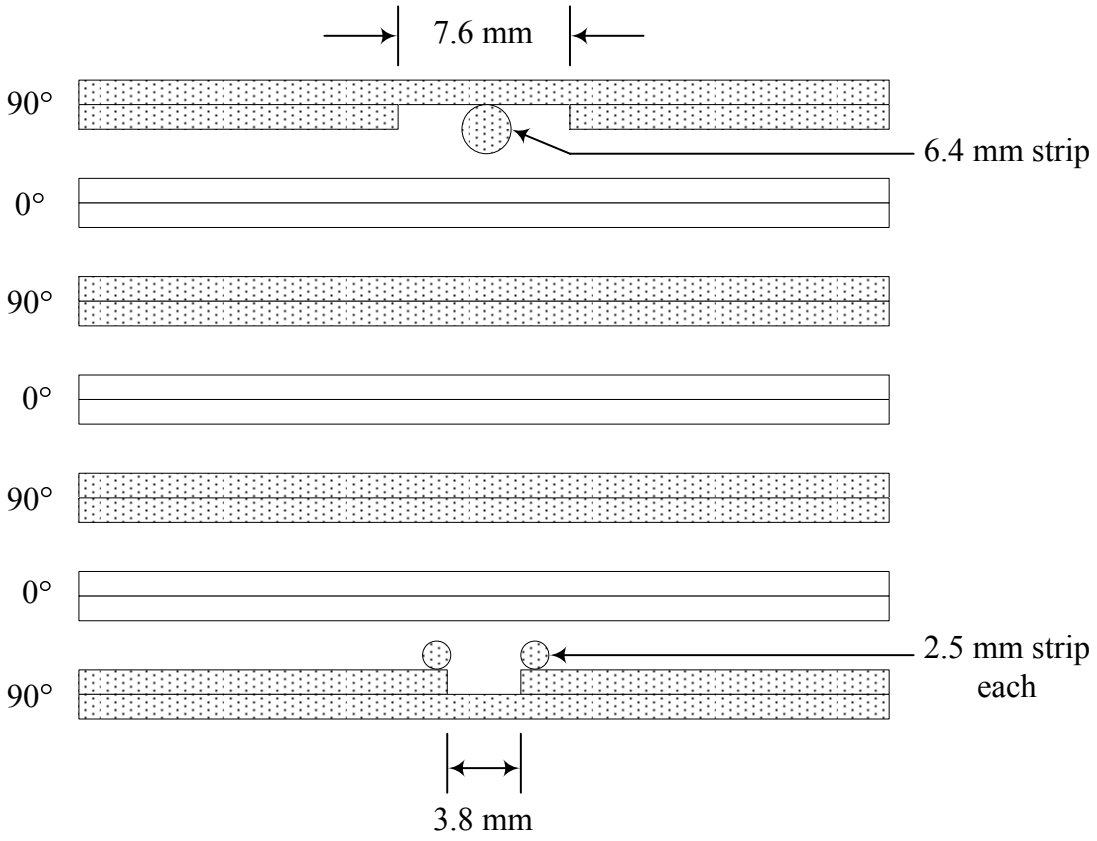

Figure 3.27 Fabrication of multiple nested wavy 0° layer.

Table 3.5 Laminates fabricated with midplane layer waviness formations.

Laminate	Total number of 0° layers	Number of wavy 0° layers	Wave fraction, F_w
$[90_2/0_2/90_2/0_2/90_2/\overline{0_2}]_s$	5	0	No wavy
$[90_2/0_2/90_2/0_2/90_2/\overline{0_{2w}}]_s$	5	1	0.2
$[90_2/0_2/90_2/0_2/90_2/0_2/90_2/0_2/90_2/0_{2w}/\overline{90_{2w}}]_s$	10	2	0.2
$[90_2/0_2/90_2/0_2/90_2/0_2/90_2/0_{2w}/90_{2w}/\overline{0_{2w}}]_s$	9	3	0.333
$[(90_2/0_2)_2/90_2/0_{2w}/90_{2w}/0_{2w}/(90_2/0_2)_2/90]_s$	12	4	0.333
$[(90_2/0_2)_3/90_2/0_{2w}/90_{2w}/0_{2w}/90_2/0_2/90]_s$	12	4	0.333

This designation represents alternating 0° and 90° layers with wavy layers centered about the laminate midplane. The wavy 0° layer (designated as $\overline{0}_{2w}$, the over bar indicating that these layers are not repeated in the symmetric stacking sequence) were placed at the midplane of the cross-ply laminate. The wave fraction, F_w, is defined as the number of wavy 0° layers divided by the total number of 0° layers within the laminate as show in Table 3.5.

Three laminates were performed in the static compression testing. The layer wave geometries of the three panels are shown in Figure 3.28. A specific shorthand designation is used to represent the number and position of wavy 0° layers within the laminate. As an example, in "4~~4", the "~"represents each wavy 0° layer whereas the numbers (4) represent the nonwavy 0° layers in the $[90_2/0_2/90_2/0_2/90_2/0_2/90_2/0_2/90_2/0_{2w}/\overline{90_{2w}}]_s$ laminate.

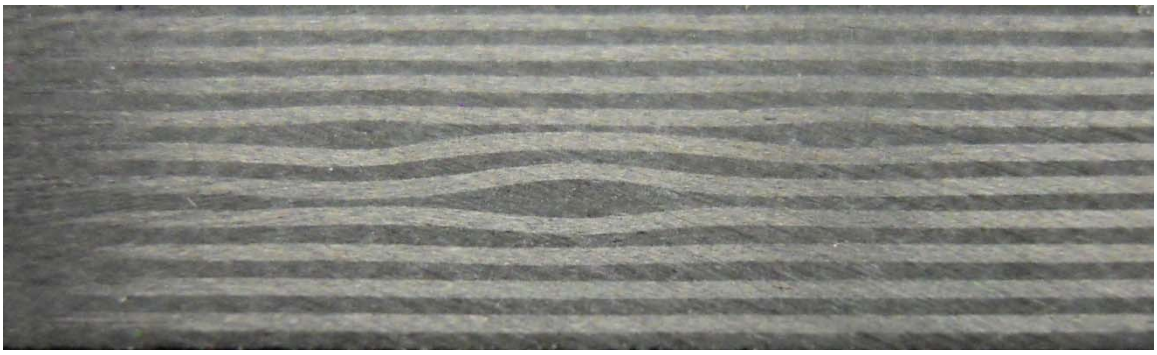

(a) $[90_2/0_2/90_2/0_2/90_2/0_2/90_2/0_2/90_2/0_{2w}/\overline{90_{2w}}]_s$ or 4~~4.

(b) $[(90_2/0_2)_2/90_2/0_{2w}/90_{2w}/0_{2w}/(90_2/0_2)_2/90]_s$ or 2~~2 with upper/lower symmetry.

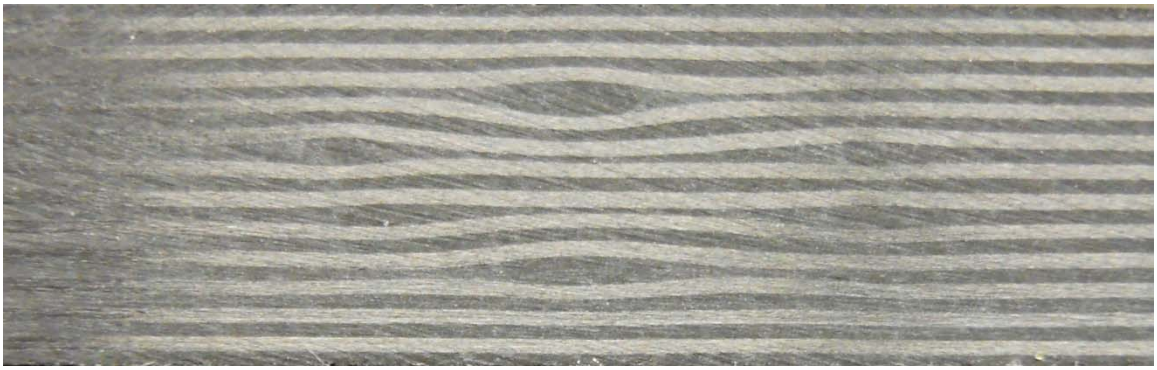

(c) $[(90_2/0_2)_3/90_2/0_{2w}/90_{2w}/0_{2w}/90_2/0_2/90]_s$ or 3~~1 with upper/lower symmetry.

Figure 3.28 Layer wave geometries used in static compression testing.

Each laminate was cut into specimens that were 38.1 mm in width and 50.8 mm in length. For laminates with layer waviness, three full-size specimens (38.1 mm width) were obtained from each panel. The average thickness of each specimen was measured from both ends of the specimen. Upon investigation of the specimen edges, the layer wave geometries of each specimen from the same panel were slightly different. Thus, the layer wave geometries at each cut were separately photographed to measure the wavelength, λ and wave amplitude, δ. The layer wave severity, δ/λ reported for each specimen was the average of the measurements from both sides.

3.3.2 Compression Testing

Static compression testing was performed using the NASA short block compression test fixture (Figure 3.29) [10] to determine the effects of layer waviness on compression strength. Specimens were loaded at a constant displacement rate of 0.8 mm/min. to ultimate failure.

3.3.3 Static Compression Test Results

Static compression test results of the specimens with layer waviness are shown in Table 3.6. The compression strength of wave-free laminates at ultimate failure was calculated using a rule of mixtures approach [51],

$$\sigma_{ult} = \frac{n_0 \sigma_{0f} + n_{90} \sigma_{90f}}{n_0 + n_{90}} \tag{3.9}$$

where σ_{0f} and σ_{90f} are axial stress at failure in the 0° and 90° layers, respectively. The quantities n_0 and n_{90} are the number of 0° and 90° layers, respectively, in the laminate.

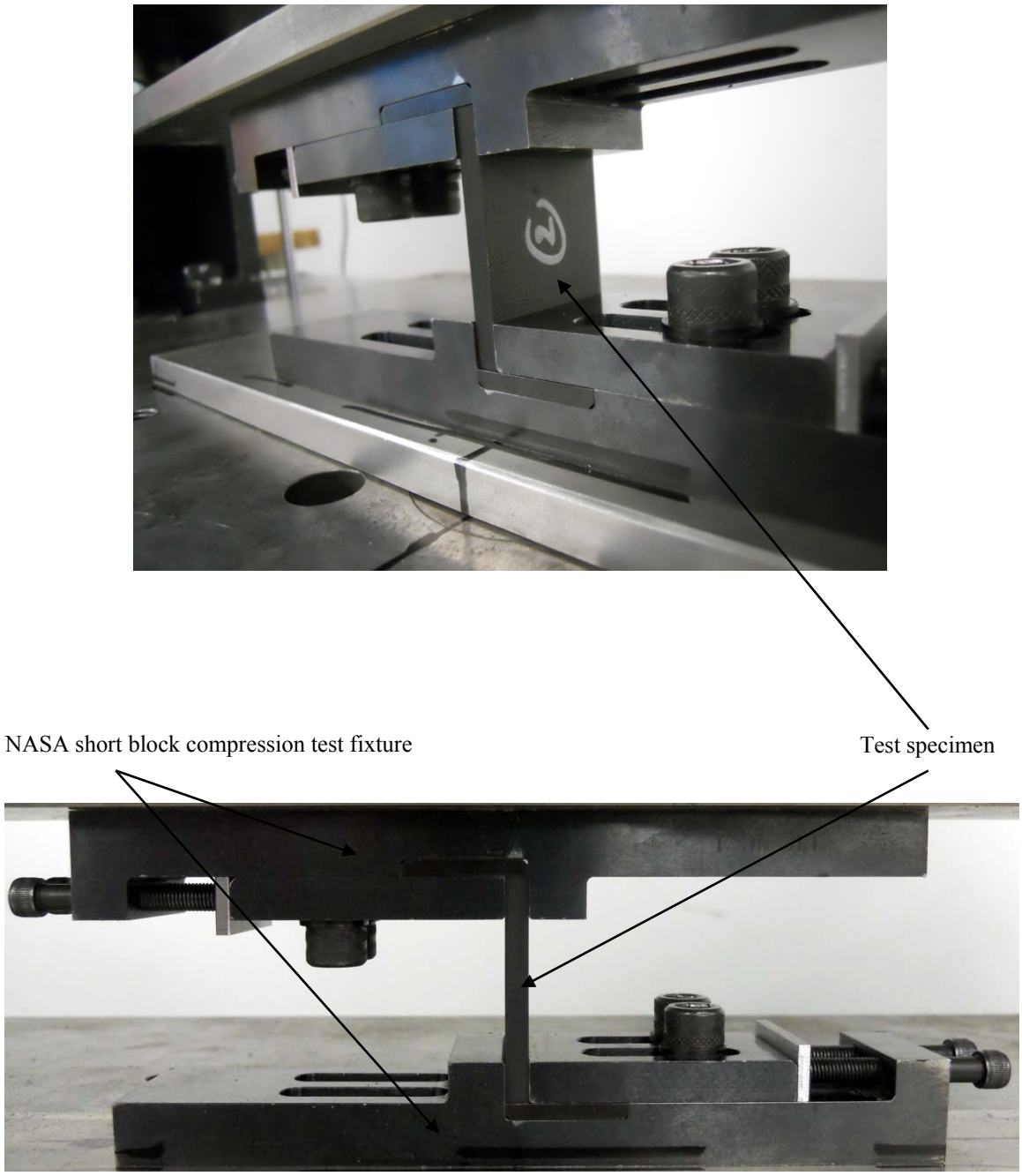

Figure 3.29 NASA short block compression test fixture.

Table 3.6 Static compression test results.

Laminate	Wave fraction, F_w	Specimen	Wave severity, δ/λ	Strength of wave-free laminate (MPa)	Strength (MPa)	Strength ratio, F_{ex}
4~~4	0.2	2	0.045	756	650	0.859
		3	0.044		657	0.868
		4	0.04		682	0.901
		average			663	0.876
2~~2 with upper/lower symmetry	0.333	1	0.049	762	564	0.737
		2	0.056		675	0.877
		3	0.056		600	0.792
		4	0.054		709	0.933
		average			637	0.835
3~~1 with upper/lower symmetry	0.333	1	0.04	762	665	0.871
		2	0.046		709	0.924
		3	0.04		717	0.935
		4	0.046		701	0.896
		average			698	0.906

The axial stresses at failure in the 0° and 90° layers for IM7/8551-7A were measured previously by Adams and Bell as described in reference [4]. The values for σ_{0f} and σ_{90f} are 1493 MPa and 86.8 MPa, respectively [4]. Compression strengths of the three wave-free laminates are shown in Table 3.6. Additionally, the wave severity, δ/λ for each specimen and the wavy 0° layer fraction, F_w for each laminate are presented in the table. The compression strength ratios, F_{ex} for each specimen are nondimensionalized by the corresponding average compression strength of the wave free laminate.

For all specimens tested, the ultimate failure was catastrophic and sudden, with no indication of failure initiation prior to ultimate failure. Thus, the progression of damage was not observed. Post failure observations of specimens indicated a brooming failure (spreading through the thickness of the laminate) in most specimens tested as shown in Figure 3.30.

The relationship between wave fraction and compression strength ratio is shown in Figure 3.31. The compression strength values of the laminates with wavy layers were higher than those obtained in previous testing [4], a result of the wave severity being lower than in previously tested specimens.

In comparing the 2~~2 and 3~~1 laminates with upper/lower symmetry, it is noted that these two laminates have the same thickness but with different wave formations. Whereas the 2~~2 laminate contains four nonwavy 0° layers at the laminate midplane, the 3~~1 laminate contain only two nonwavy 0° layers at the laminate midplane as shown in Figure 3.28. Therefore, more interaction of the wavy 0° layers above and below the central set of nonwavy 0° layers was expected in the 3~~1 laminate.

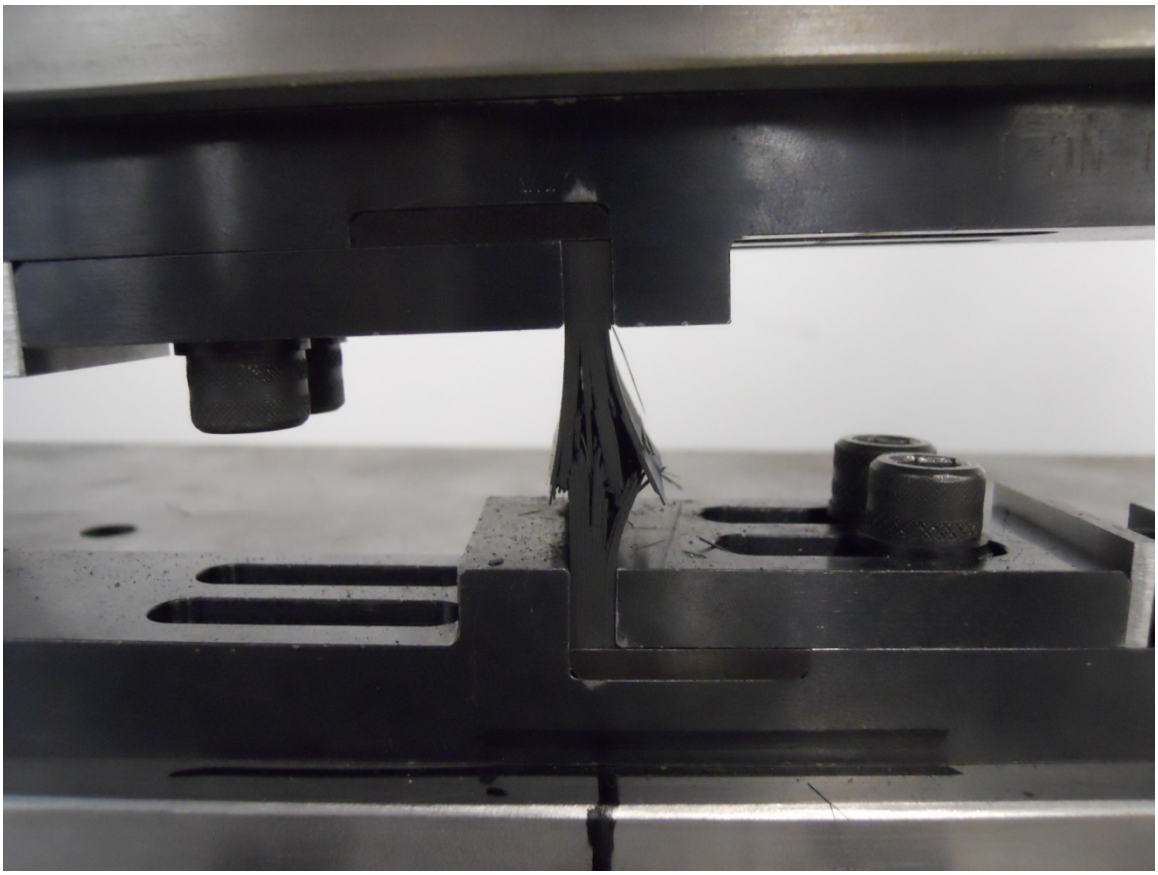

Figure 3.30 Brooming failure of layer waviness specimen.

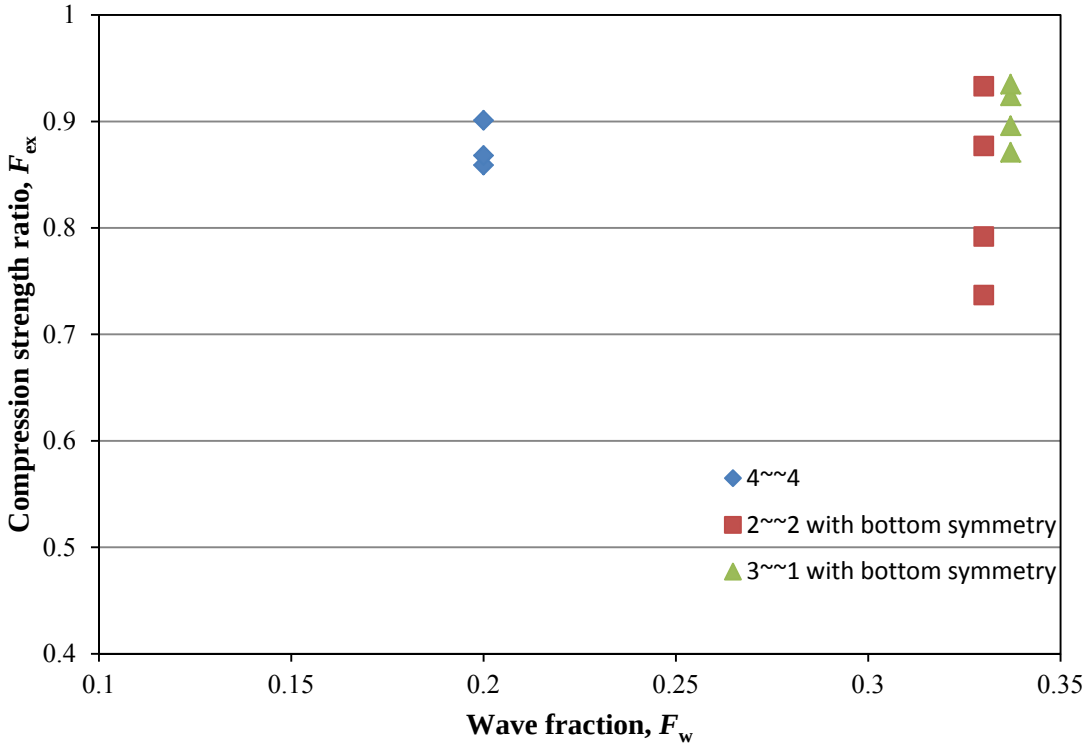

Figure 3.31 Compression strength ratio versus wave fraction.

As shown in Figure 3.31, the 2~~2 laminate displayed a high degree of variability in compression strength. This variability was believed to be due to variations in the layer wave severity produced in this panel.

CHAPTER 4

FINITE ELEMENT ANALYSIS

As discussed in the literature review, the finite element method has been used by previous researchers to investigate the state of stress and initial failure associated with layer waviness in composite laminates. In this investigation, a progressive damage analysis is incorporated into the finite element analysis to investigate compression strength reductions due to layer waviness. The composite material to be investigated is the same IM7/8551-7A, carbon/epoxy discussed previously with material properties summarized in Table 3.1 and Table 3.2. The commercial finite element code ANSYS (version 12.1) [8] was used throughout this research. Two-dimensional plane strain finite element analyses were performed using four-noded PLANE42 elements and orthotropic material properties.

In this research, interface elements with a cohesive-zone model were utilized at selected layer interfaces where the formation of delaminations was possible. The use of cohesive elements in this research allowed for the formation and propagation of interlaminar delaminations under general mixed-mode loading. The use of cohesive elements allowed for a progressive failure analysis to be performed in a single, incremental analysis.

To investigate and validate the cohesive elements used to model interlaminar delamination in the vicinity of layer waviness, a series of simplified analyses were performed and compared to experimental results. Initially, a series of two-block models were utilized to investigate initial failure at an interface under a specified loading. A second set of analyses and experiments were performed to establish the fracture mechanics parameters in the cohesive elements used to predict delamination growth. Two types of fracture mechanics testing, the Double Cantilever Beam test for Mode I crack growth and the End-Notched Flexure test for Mode II crack growth, were performed experimentally and modeled using cohesive elements to validate the behavior of the cohesive zone model. Further discussion and results of the cohesive elements used in this research are presented in the following sections.

4.1 Virtual Crack Closure Technique

The initial finite element analyses were performed to simulate the Mode I Double Cantilever Beam (DCB) and Mode II End-Notched Flexure (ENF) tests discussed previously. The Virtual Crack Closure Technique (VCCT) was used to calculate the energy release rates, and calculated values were compared to those determined experimentally using the compliance calibration method.

4.1.1 VCCT for Mode I Double Cantilever Beam

The dimensions and loading of the Mode I DCB specimen modeled are illustrated in Figure 4.1. The dimensions of the specimen were: length, L of specimen is 127 mm and width is 24.1 mm. The crack length, a_0, was approximately 63.5 mm.

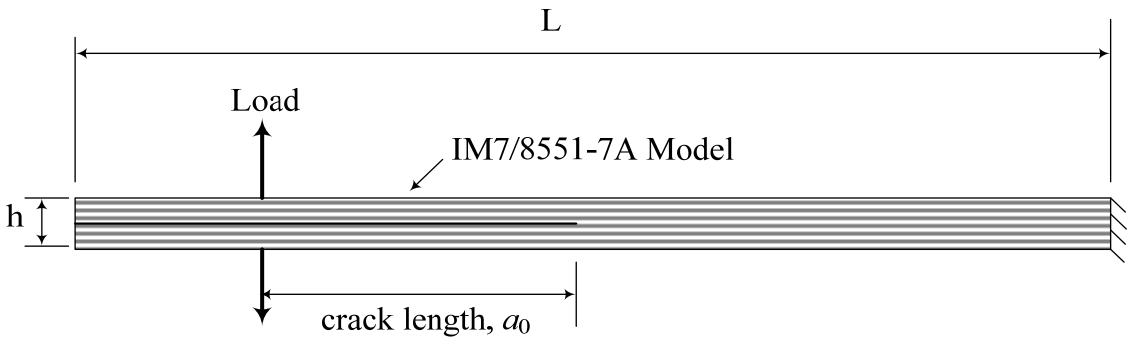

Figure 4.1 Double Cantilever Beam (DCB) model.

This initial crack length also corresponds to an initial delamination length of about 50.8 mm plus the extra length 12.7 mm required for bonding of the loading hinges. The thickness of the laminates, *h,* is 4.06 mm. The cross-ply laminate contains 15 plies (8 90° plies 7 0° plies). The initial crack is along the interface of ply No.9 and No.10 as shown in Figure 4.2.

The crack surfaces were modeled by using a series of node pairs and were coupled along the nondelaminated length using the CPINTF command, as illustrated in Figure 4.3. The coupled node pairs were located along the delamination from the tip of the initial crack to the opposite end of the specimen. The mesh for each ply was generated with one element through the thickness and 400 elements along the length. The material properties of the 90° plies and 0° plies were assigned to the specific locations within the laminate as shown in Figure 4.4. Mechanical properties for the IM7/8551-7A carbon/epoxy material, obtained from Reference [44] are presented in Table 3.1 and Table 3.2.

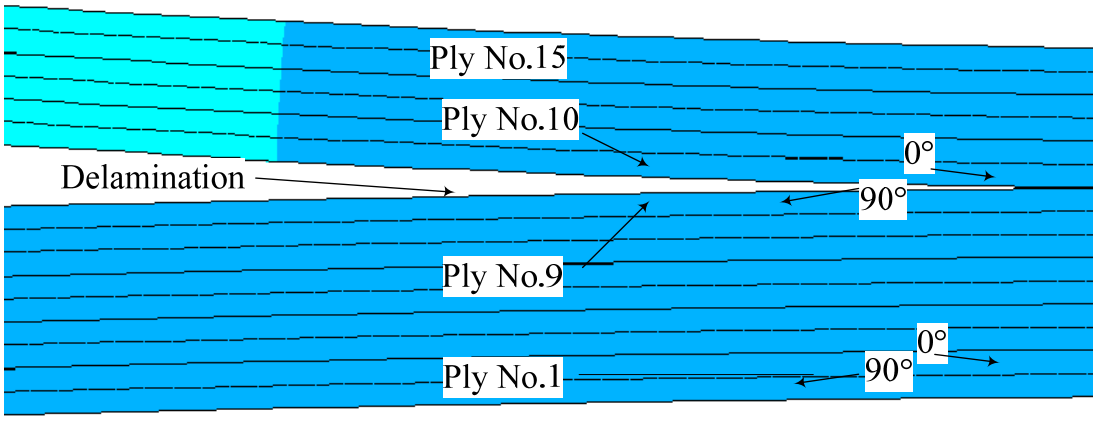

Figure 4.2 Through the thickness position of initial delamination.

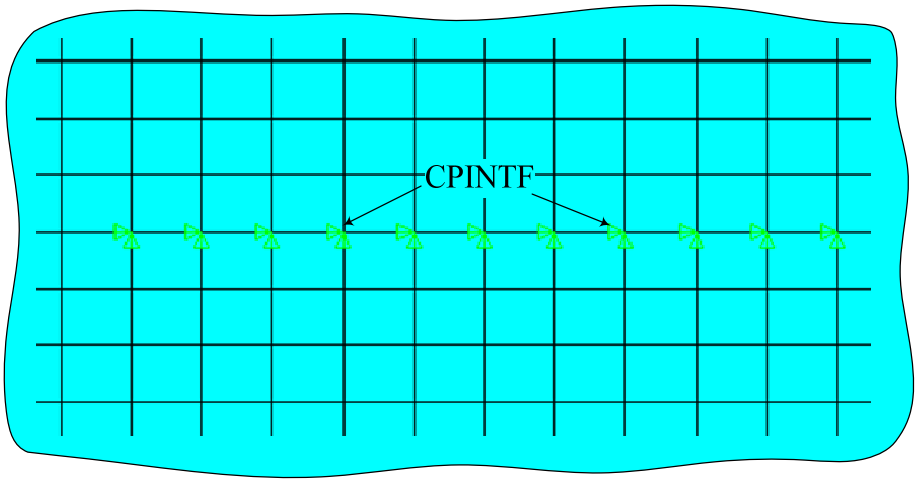

Figure 4.3 Coupled node pairs along delaminated interface.

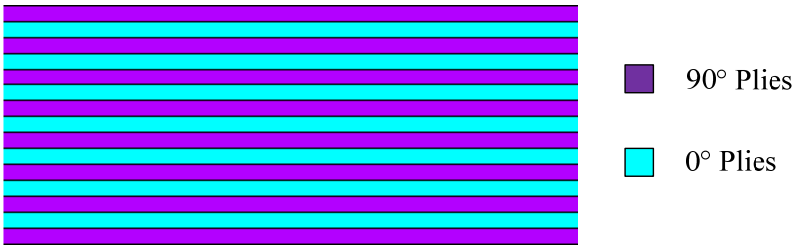

Figure 4.4 Material properties defined for plies.

As described in Chapter 2, the crack closure method employs two analysis steps to determine the strain energy release rate: the crack extended, and the crack closed. The VCCT finite element models in Figure 4.5 and Figure 4.6 show the crack extended (deformed finite element mesh) and the crack closed (undeformed finite element mesh) respectively. The crack propagation length, or change in the crack length, was taken as the length, Δa of each finite element. The work required to close the crack by one element length (Figure 4.5) is

$$W = \tfrac{1}{2} F w,$$

where F is the force required to close the nodes i and i', and w is the opening displacement between nodes i and i'. The force F required to close the crack can be obtained from closing the crack between nodes i and i'. Using these outputs from the finite element analysis, the Mode I energy release rate was determined by using equation 2.8. Results of the VCCT analysis were used as a comparison to those obtained using Mode I DCB test and interface elements with a cohesive zone model.

Figure 4.7 illustrates the deformation of the Mode I DCB model during load application. Using VCCT, the value of G_{Ic} calculated from data from a representative specimen (Chapter 3) was 0.624 KJ/m^2. This value was in general agreement with the measured value from this specimen of 0.729 KJ/m^2, as well as the average of the seven specimens tested, 0.589 KJ/m^2.

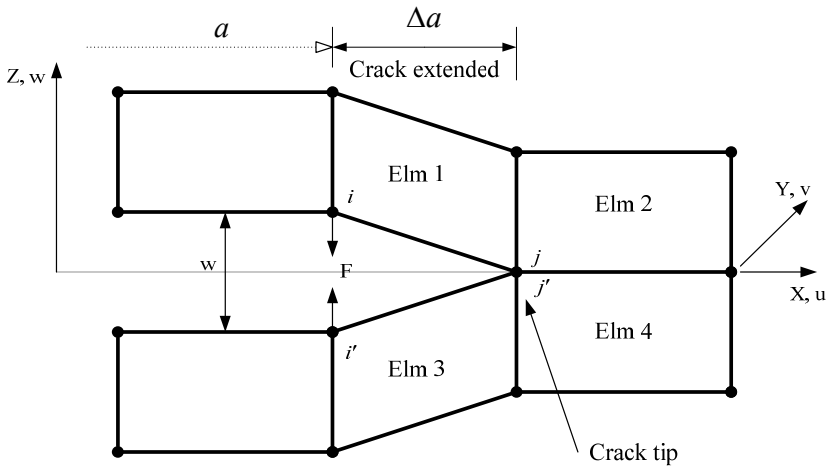

Figure 4.5 Mode I Crack extended (deformed finite element mesh).

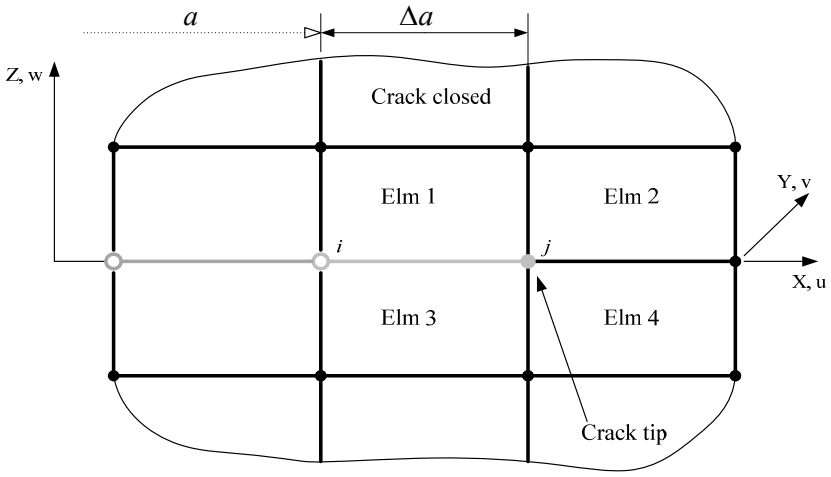

Figure 4.6 Mode I Crack closed (undeformed finite element mesh).

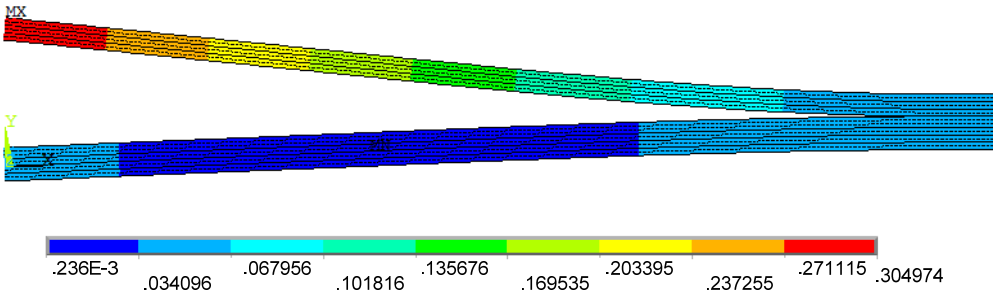

Figure 4.7 Deformed VCCT DCB model.

4.1.2 VCCT for Mode II End-Notched Flexure

For Mode II ENF testing, similar two-dimensional finite element analyses were performed. The dimensions of the Mode II ENF specimen are illustrated in Figure 4.8. The specimen half-span, L, was 50.8 mm and the width was 22.1 mm. The crack length, a_0, was approximately 30.5 mm. The distance from the roller center to the end, L_c, was 17.5 mm. The thickness of the laminates, $2h$, is 3.81 mm. The initial crack was located along the interface of ply No.6 and No.7.

Node pairs were modeled along the delaminated interface, and the nodes were coupled beyond the crack tip to produce the desired crack length as illustrated in Figure 4.9. At the crack interface surfaces, contact and target elements were applied to each surface in order to prevent surface penetration; however, the surfaces were modeled as unbonded.

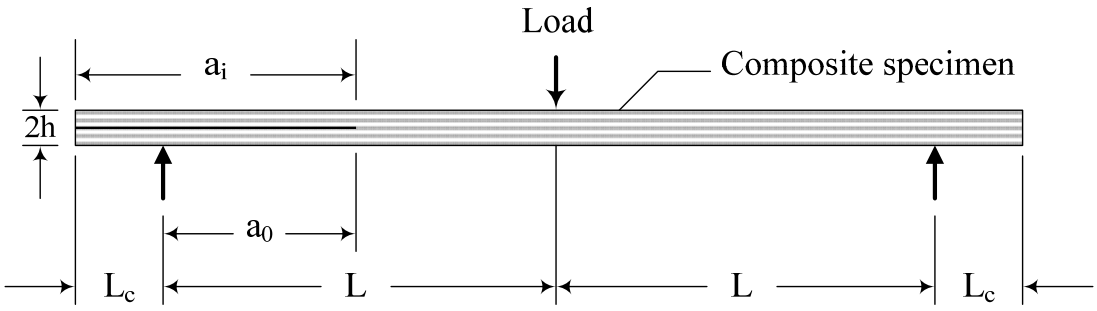

Figure 4.8 End-Notched Flexure model.

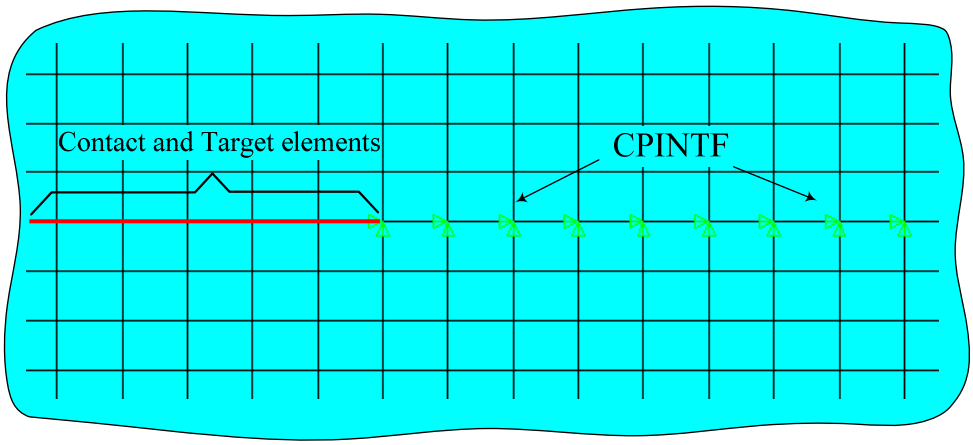

Figure 4.9 Mode II Interface element coupled.

The Mode II ENF mesh was similar to the Mode I DCB mesh but the length of each finite element was slightly longer because of the longer specimen. Similarly, VCCT was performed on the Mode II model. The finite element model in Figure 4.10 shows the Mode II sliding displacement between the nodes i and i'. The relative displacement Δu was measured between nodes i and i'. Subsequently, the force F_x required to close the crack at node i was determined.

Using equation 2.8, the Mode II energy release rate was calculated using data from a representative ENF test. Using VCCT, the value of G_{IIc} calculated from this representative specimen was 1.01 KJ/m^2. This value was in general agreement with the measured value from this specimen (using compliance calibration) of 0.903 KJ/m^2, as well as the average of the three specimens, 1.04 KJ/m^2. Figure 4.11 illustrates the deformation of the mode II ENF model after load was applied.

4.2 Two-Block Validation Analyses

Two bonded blocks were modeled to validate the cohesive elements proposed for use in the layer waviness models. The same PLANE42 elements with a plane strain assumption and 0° layer properties were used and cohesive elements were modeled at the interface of the element sets. For these simulations, Mode I, Mode II, and mixed-mode loadings were applied to investigate the maximum traction, corresponding to interface failure, of the cohesive elements. The material properties used in the cohesive elements are summarized in Table 4.1.

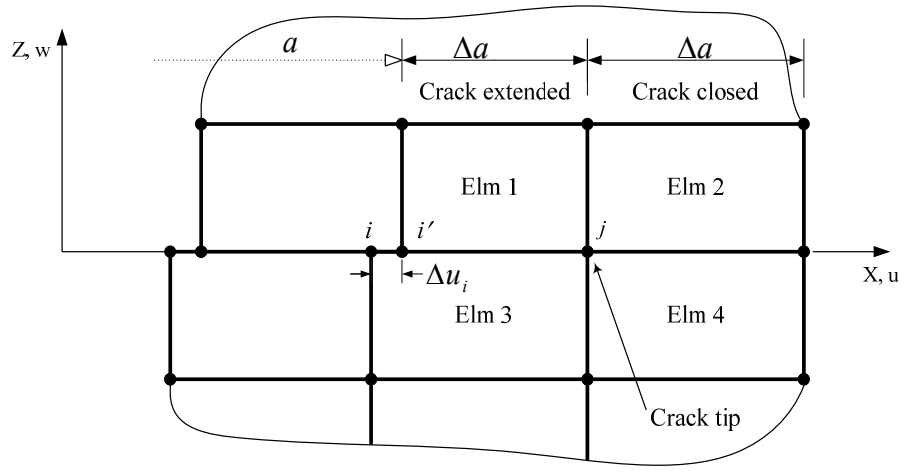

Figure 4.10 Mode II Crack extended (deformed finite element mesh).

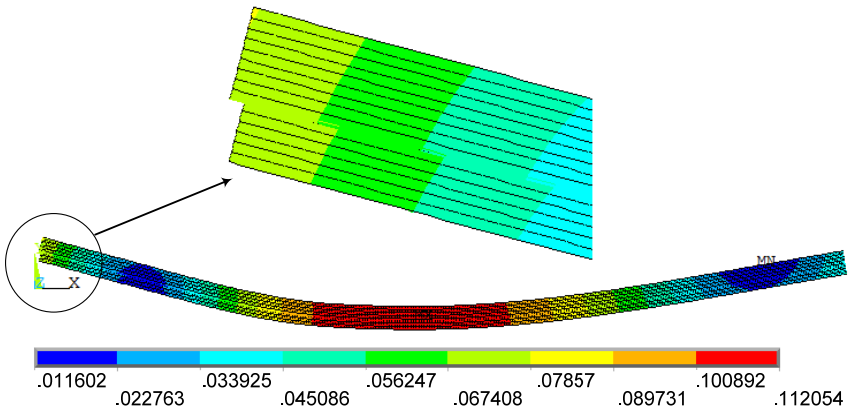

Figure 4.11 Deformed VCCT ENF model.

Table 4.1 Cohesive Element Material Properties.

G_{Ic}	G_{IIc}	σ_T	τ_T	K
0.589 KJ/m^2	1.04 KJ/m^2	62.4 MPa	82.7 MPa	8.8×10^6 N/mm

The quantity σ_T is the maximum normal contact stress, τ_T is the maximum equivalent tangential contact stress, and K is the cohesive element stiffness. The initial stiffness, K should be sufficient high to simulate the extremely high initial stiffness of the layer interface. However, an excessively very high K value may cause convergence problems during the finite element simulation.

Modeling delamination with cohesive zone elements combines a stress-based formation with a fracture mechanics based-formulation [35]. The cohesive constitutive law relates the traction, $\boldsymbol{\sigma_t}$ and the displacement jumps, δ at the interface as shown in Figure 4.12. The area under the traction-displacement curve is the respective critical fracture energy, G_c for a particular fracture mode (Mode I, II, or III).

4.2.1 Two-Block Mode I Simulation

For the pure Mode I tensile test, the two-block simulation was performed using displacement boundary conditions. The geometry and loading is shown in Figure 4.13. A 10 × 10 mesh of four-node elements was adopted for this model. The interface to be investigated was modeled with the cohesive zone model (CONTA171 and TARGE169).

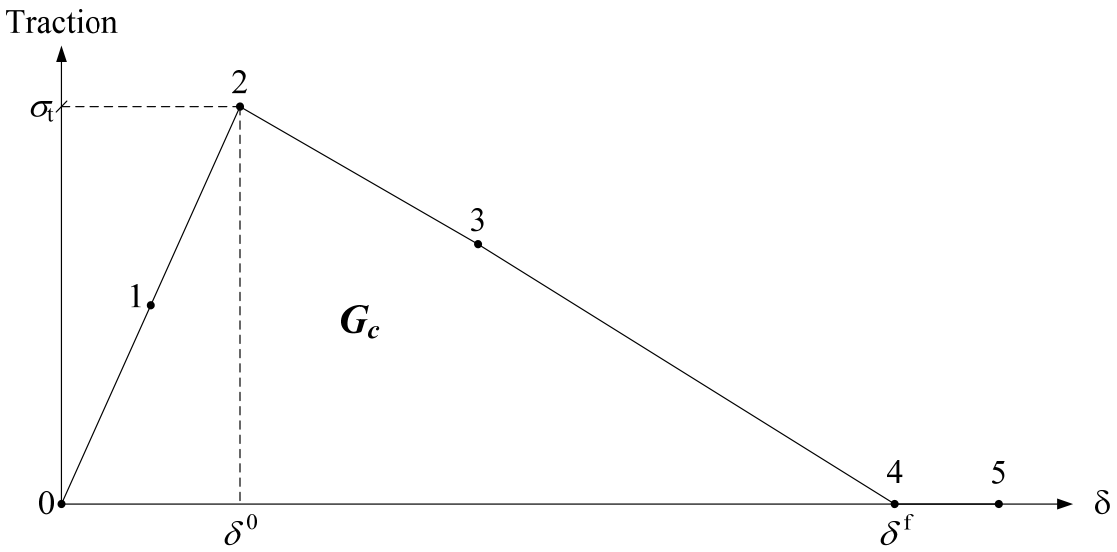

Figure 4.12 Cohesive element decohesion model.

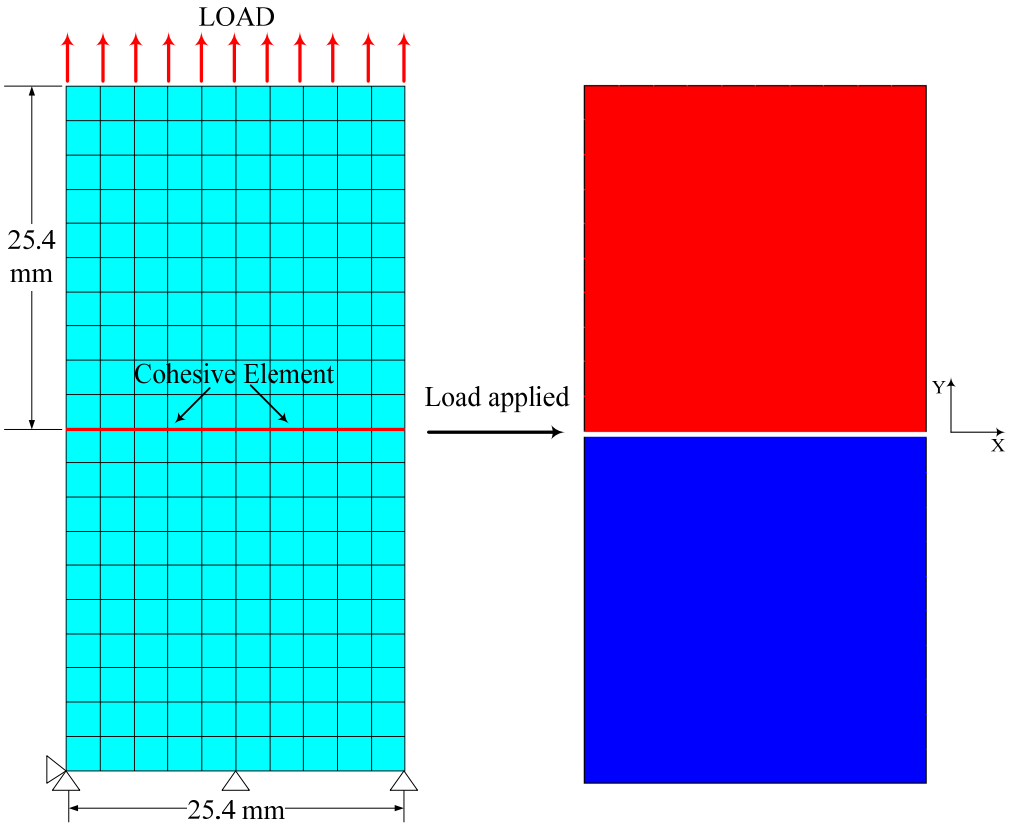

Figure 4.13 Two block Mode I model.

The results of the Mode I simulation to establish the effective tensile strength of the cohesive element are presented in Figure 4.14. From the plot, the maximum value of Mode I traction obtained is 62.5 MPa. Referring to Table 4.1, the maximum normal contact stress, σ_T input into the analysis was 62.4 MPa. Thus, the Mode I two-block simulation showed that an initial interface failure will be produced in the simulation when the interlaminar normal stress reaches the input value of the maximum normal contact stress, σ_T. Beyond this point, the interlaminar normal stress decreases according to the softening model and vanishes when complete decohesion occurs.

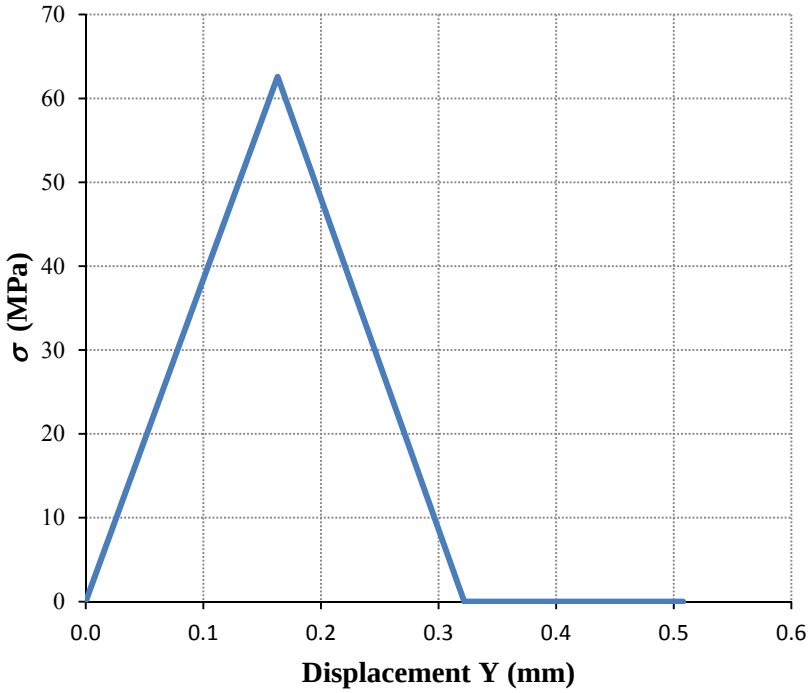

Figure 4.14 Traction from Mode I two-block model.

4.2.2 Two Block Mode II Simulation

A two-dimensional plain-strain finite element simulation of a pure shear test was performed under displacement control. The geometry and loading is shown in Figure 4.15. The mesh consisted of two blocks, each modeled with 64 four-node elements. The cohesive zone model (CONTA171 and TARGE169) was also employed to this model as the interface element.

The shear load was applied as an *x* direction displacement to the top row of elements as shown in Figure 4.15. Results of the Mode II simulation are shown in Figure 4.16. A shear failure of the cohesive elements, which appeared as a displacement or sliding of the interface in the *x* direction, occurred at a shear traction of 80 MPa. Referring to Table 4.1, the equivalent tangential contact stress, τ_T input into the analysis was 82.7 MPa. The slight variation in shear stress distribution across the interface is believed to be responsible for the small difference between the prediction and the input shear stress τ_T. Overall, however, the results of the Mode II two-block simulation were in acceptable agreement with the expected peak shear stress. After the maximum shear traction has achieved, the interlaminar shear stress also reduced in relation to the softening model and became zero at complete decohesion.

4.2.3 Two Block Mixed-Mode Simulation

In the analysis of delamination formation and growth due to layer waviness in composite laminates, delamination at the interface is believed to occur under mixed-mode loading. Thus, a two-block simulation was performed under mixed-mode loading. Equal magnitudes of displacement were applied in both the Mode I and Mode II orientations.

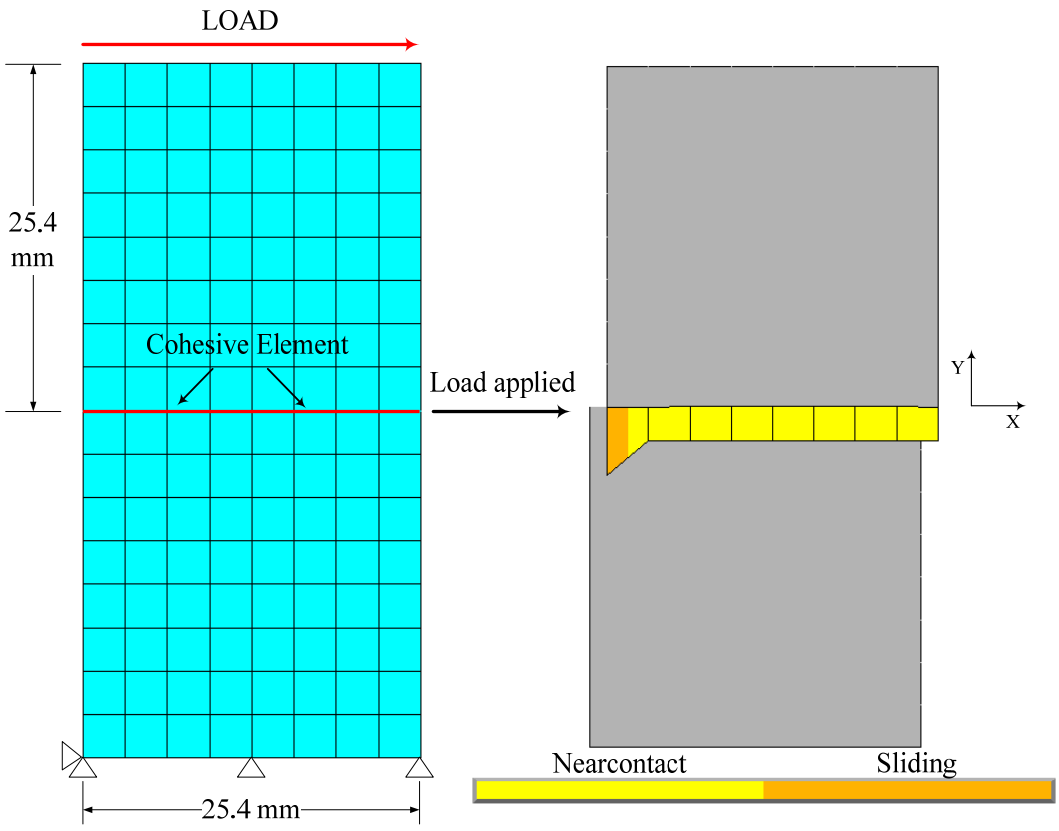

Figure 4.15 Two elements mode II model.

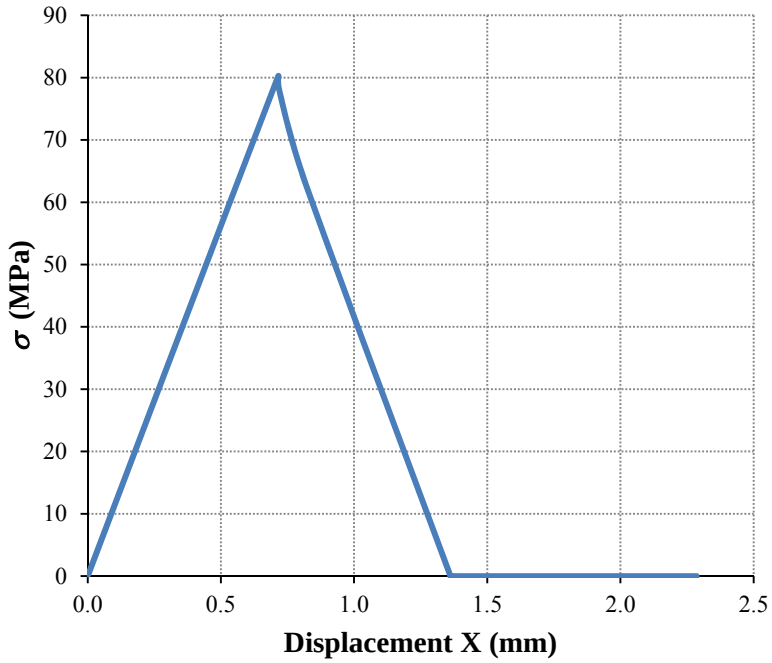

Figure 4.16 Traction from Mode II two-block model.

The geometry and loading are described in Figure 4.17 and the 400 element blocks of four-node elements are shown. The delamination was simulated with the cohesive zone model (CONTA171 and TARGE169).

For pure Mode I or Mode II loading, the onset of interfacial delamination can be specified by the respective traction components σ_T and τ_T. Results from the mixed-mode simulation show that the interfacial delamination forms at a lower stress level than the normal traction and shear strength. At softening onset (initiation of delamination), σ_x was 9.86 MPa and σ_y was 33.6 MPa. Thus, softening onset under mixed-mode loading occurs well before either of the relative traction components reaches their allowable strength, as expected.

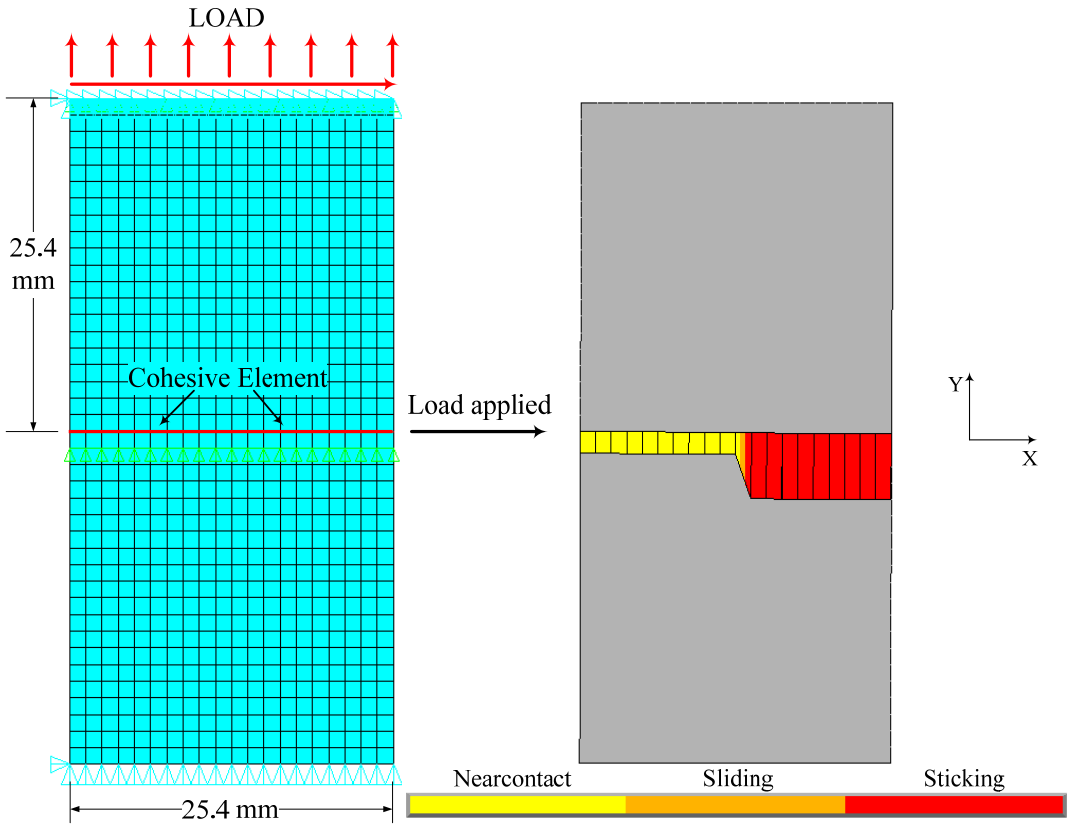

Figure 4.17 Two block mixed-mode model.

Following the mixed-mode loading of the two-block model, additional simulations with cohesive elements were performed for both the Mode I DCB and Mode II ENF tests prior to the initial analyses of layer waviness in composite laminates. Results of these simulations are presented in the following sections.

4.3 Mode I Double Cantilever Beam Model

In this section, result of the numerical simulation for the Mode I Double Cantilever Beam (DCB) specimen using cohesive elements is presented. The DCB simulation was performed to validate the debonding parameters of the Mode I cohesive zone model, which will be employed to model interlaminar delaminations in the layer waviness models. The DCB geometry and loading are those shown previously in Figure 4.1 and in Figure 4.2. Two-dimensional plane strain (PLANE42) elements were used. The interface elements were modeled by using a series of node pairs. Subsequently, CONTA171 and TARGE169 were used to define cohesive zone elements along the interface to be delaminated. CONTA171 is used to specify contact and sliding between 2-D "target" surfaces (TARGE169) and a deformable surface, defined by this element [8]. The interface elements were bonded along the crack direction from the tip of the initial crack to the other end of the specimen. The material properties associated with the debonding interface of the cohesive zone model was given in Table 4.2.

Table 4.2 Input Properties for DCB Cohesive Elements.

G_{Ic}	σ_T	K
0.731 KJ/m^2	62.4 MPa	8.8×10^6 N/mm

The results of the DCB simulation as illustrated in Figure 4.18 were found to be in good agreement with experiment. However, if 62.4 MPa is used, it was not possible to obtain a converged solution as discussed in more detail in references [52] and [53]. In reference [52], the authors explained that using the linear element in ABAQUS, it was not possible to obtain a converged solution if a higher value of initial tensile strength was used. A reduced value of σ_T was used instead in their work. To eliminate this problem, the σ_T value can be artificially reduced to obtain convergence while the G_{Ic} value is preserved. Such a decrease in the σ_T value was found to produce some differences in the interface behavior about the peak load, but had minimal effect on the delamination propagation. In this DCB simulation, σ_T is reduced to 8.62 MPa to obtain convergence. However, as shown in Figure 4.18, the peak load of the model at the first delamination occurs a little earlier than the experimental peak load (about 5% of the opening displacement). A contour plot of the deformation and the σ_y stress component within the DCB specimen is illustrated in Figure 4.19.

4.4 Mode II End-Notched Flexure Model

To validate the debonding parameters of the Mode II cohesive zone model, the End-Notched Flexure (ENF) test was modeled under displacement control. The dimensions and loading of the ENF test are as previously shown in Figure 4.8 and described in Section 4.1.2. The element type and cohesive elements used in the Mode II ENF model were identical to those used with the Mode I DCB model. Double nodes were generated to model the interfacial surfaces along the crack (interface).

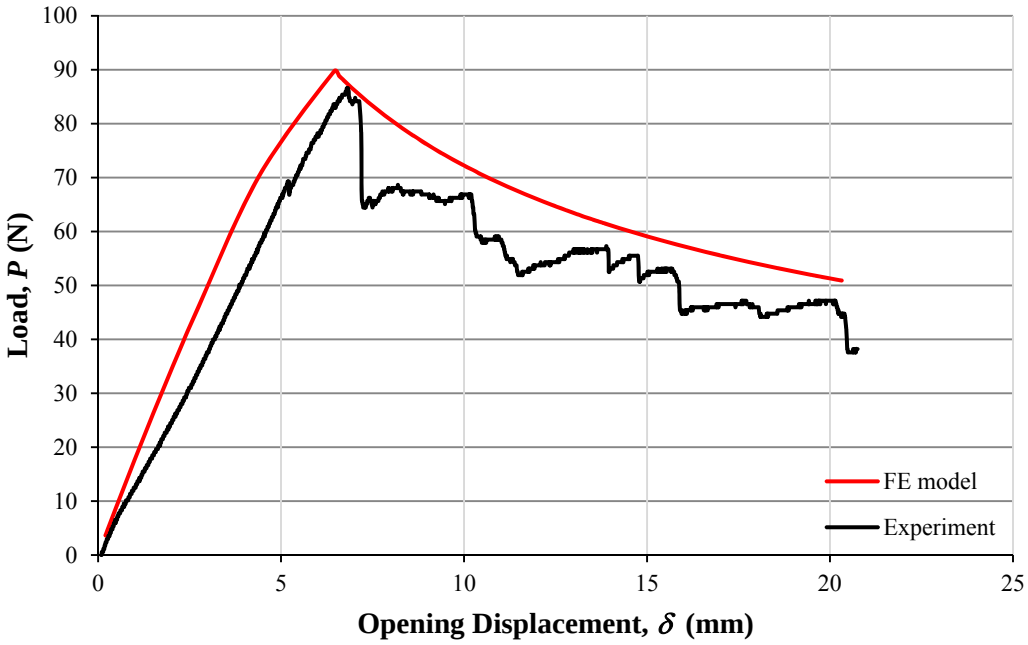

Figure 4.18 Comparison of predicted and experimental load versus displacement from DCB specimen.

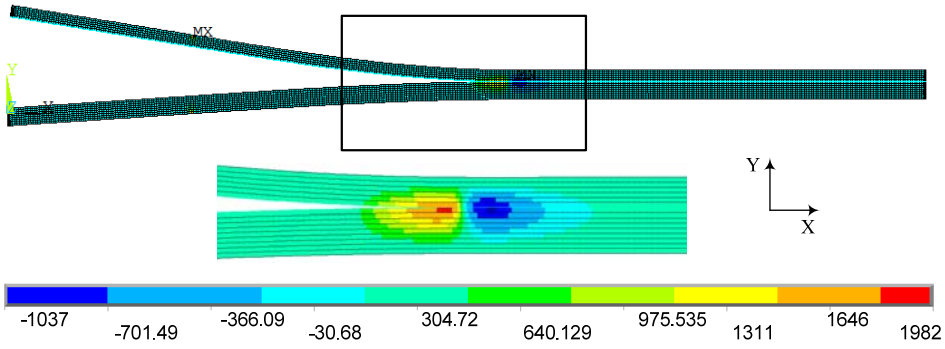

Figure 4.19 DCB contour plot of deformation and σ_y

The interface elements were positioned and bonded along the crack direction from the tip of the initial crack to the opposite end of the specimen. However, at the initial crack interface surfaces, contact and target elements were applied to each surface in order to avoid penetration, but they were not bonded. Input properties for the Mode II cohesive zone model are given in Table 4.3.

Results of the ENF simulation are shown in Figure 4.20. The applied load versus midspan deflection curves from the numerical solution is in good agreement with the experimental data. Additionally, a contour plot of the deformation and the stress component τ_{xy} within the ENF specimen are shown in Figure 4.21.

4.5 Layer Waviness Model

In this section, the compression strength effects of layer waviness are investigated in cross-ply laminates. Various layer wave formations were investigated using finite element modeling. The finite element models were based on previous works performed by Adams and Hyer [2], Bradley, Adams and Gascoigne [3], Adams and Bell [4], as well as Telegadas and Hyer [8]. Results of finite element analyses using cohesive elements will be compared to experimental data obtained from earlier referenced works as well as from mechanical testing performed as part of this research investigation.

Table 4.3 Input Properties for ENF Cohesive Elements.

G_{IIc}	τ_T	K
1.04 KJ/m^2	82.7 MPa	8.8×10^6 N/mm

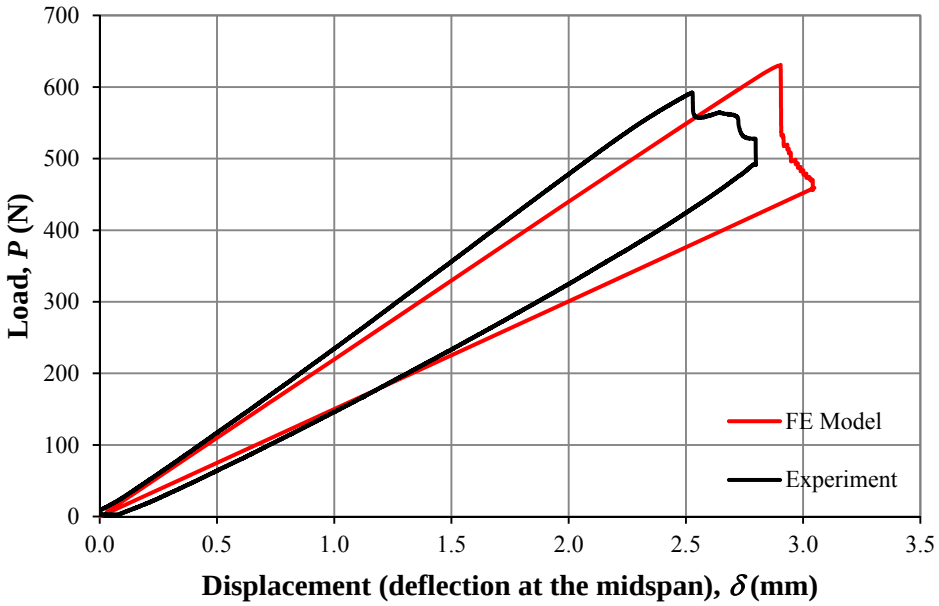

Figure 4.20 Comparison of predicted and experimental load versus displacement from ENF specimen.

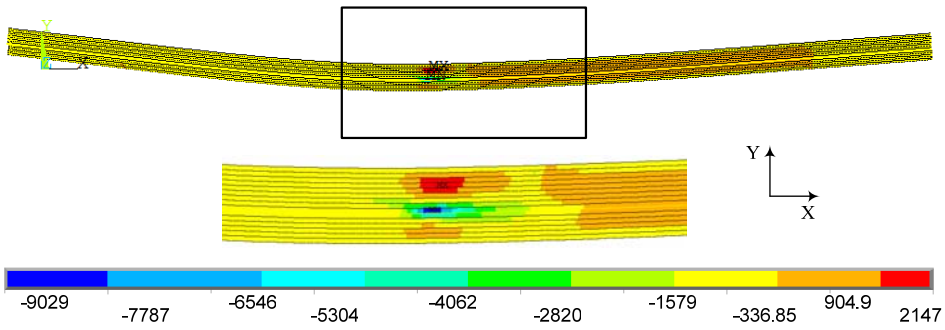

Figure 4.21 ENF contour plot of deformation and τ_{xy}.

4.5.1 Finite Element Modeling

Two-dimensional plane-strain finite element analyses were performed using four-noded PLANE42 elements and orthotropic material properties. Intentional fabrication of wavy layers into carbon/epoxy cross-ply laminates was previously accomplished by Adams and Bell [4] and Bradley, Adams and Gascoigne [3]. Photomicrographs of the manufactured wave geometries were digitized by Bradley, Adams and Gascoigne [3] and used to model layer waviness in the finite element models. IM7/8551-7A carbon/epoxy prepreg material properties were used, as summarized previously in Table 3.1 and Table 3.2.

Figure 4.22 illustrates an example of a cross-ply composite laminate with layer waviness that was analyzed. The stacking sequence of this laminate is denoted as $[90_2/0_2/90_2/0_2/90_2/\overline{0}_{2w}]_s$. This designation indicates alternating 0° and 90° layers with the wavy 0° layer (designated as $\overline{0}_{2w}$, the over bar indicating that these layers are not repeated in the symmetric stacking sequence) placed at the midplane of the cross-ply laminate. The wave fraction, F_w, is defined as the number of wavy 0° layers divided by the total number of 0° layers within the laminate. For this laminate, there is only one wavy 0° layer, and a total of five 0° layers. Thus, the wave fraction for this model is 0.2, and this model is referred to as the "one-of-five," or "2~2" model, where the "~" and the 2's represent the wavy and non-wavy 0° layer, respectively. Additionally, layer wave "severity" was characterized by the parameter, δ/λ, where the wave amplitude, δ and the wavelength, λ are defined as shown in Figure 4.22. For all wavy 0° layer fractions modeled, the measured value of δ/λ was 0.075 which was representative of the intentionally fabricated layer waviness [4, 5].

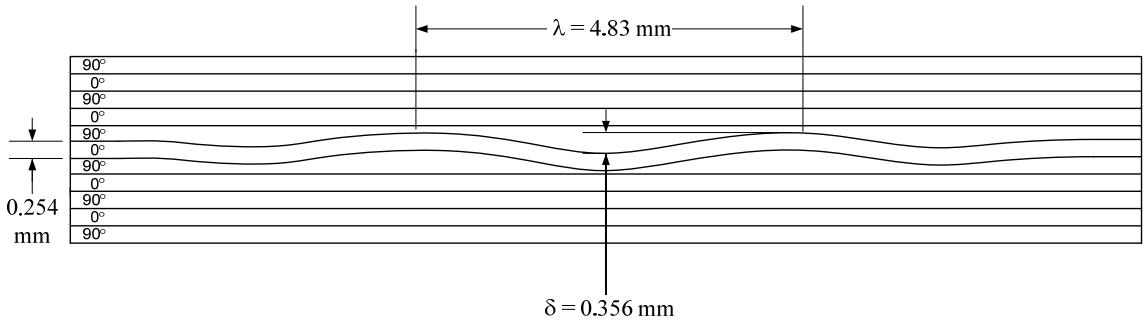

Figure 4.22 Layer waviness analyzed in cross-ply composite laminate.

A plane of symmetry was established at the central trough of the wave, and one-half of the actual wave geometry was modeled as shown in Figure 4.23. For the one-of-five finite element model, the geometry, boundary conditions, and loading are also described in Figure 4.23. From the picture, the purple and blue colors represent 90° layers and 0 ° layers, respectively. The finite element mesh used is shown in Figure 4.24.

The length of wavy layer region, L_w was defined as the length of a wavy 0° layer starting from the plane of symmetry to a point where the waviness completely ends, as shown in Figure 4.23. The length of the model region, L was the total length of the composite laminate modeled from the plane of symmetry, as shown in Figure 4.23. For this investigation, the length of the wavy layer region (L_w) and the model region (L) were selected to be 11.4 mm and 15.2 mm, respectively. Displacement boundary conditions were applied to enforce symmetry conditions. The nodes along the central plane of symmetry were constrained in the x-direction, and a single node at the opposite end of the mesh was constrained in the y-direction.

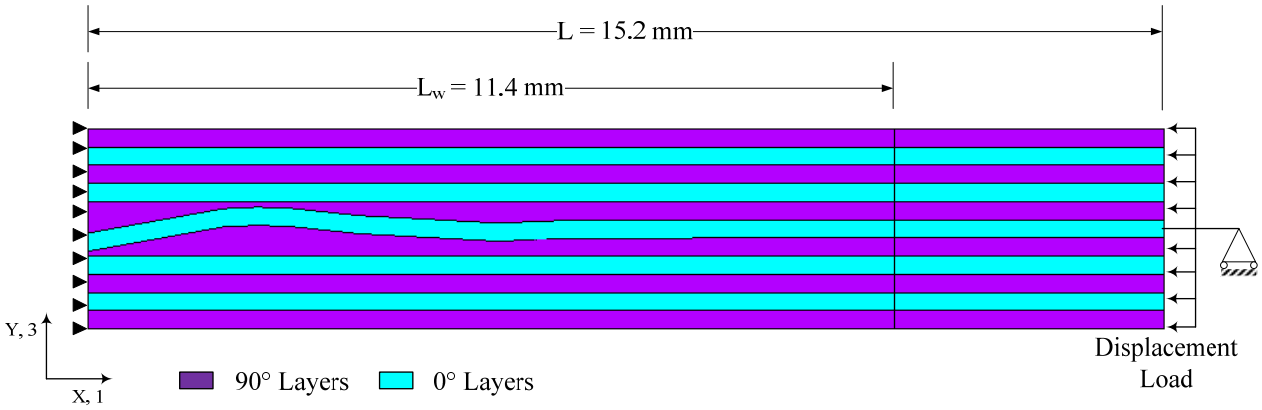

Figure 4.23 Plane of symmetry for finite element model.

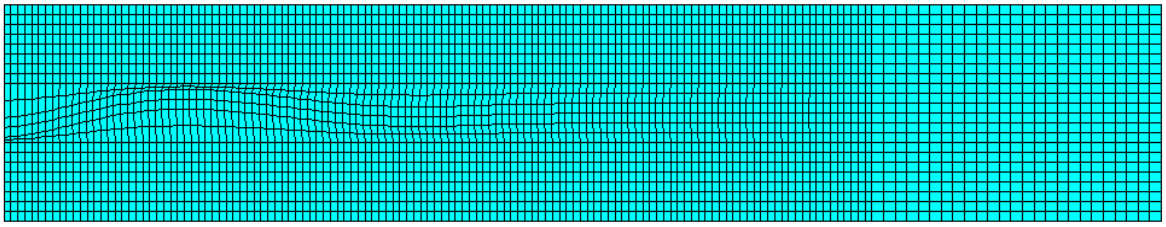

Figure 4.24 Finite element mesh for one-of-five or 2~2 layer waviness model.

Compressive loading was applied by prescribing U-displacement boundary condition at the end of the mesh away from the layer waviness.

Wavy layers modeled in the composite laminates were required to be sufficiently smooth to avoid producing localized disturbances in the stresses at the layer interfaces. Coordinates obtained from the digitization of actual layer waviness in fabricated laminates did not satisfy a smooth quadratic curve equation. Hence, a series of spline curves satisfying a quadratic equation were used to model the wavy layers in this investigation. To form the cohesive zone model at the interfaces of the wavy layer, double sets of two smooth splines, which were used to generate the "double-noding" were generated to connect 54 key points defined in ANSYS. Figure 4.25 (a) demonstrates a set of the smooth spline curves, two of which produce the boundaries of a wavy layer. Several other key points were also generated to define wave-free 0° and 90° layers. These splines and points were then used to define areas. A refined mesh of 0.091 mm × 0.127 mm elements was generated for the wavy region of the laminate as shown in Figure 4.25 (b).

All the composite laminates modeled are listed in Table 4.4 and Table 4.5. A specialized shorthand designation as described above is used to symbolize the number and position of wavy 0° layers within the laminate. A set of laminates modeled with wavy layers centered about the midplane is listed in Table 4.4. Composite laminate models having multiple sets of separated wavy layers with same horizontal orientation within the laminate are listed in Table 4.5.

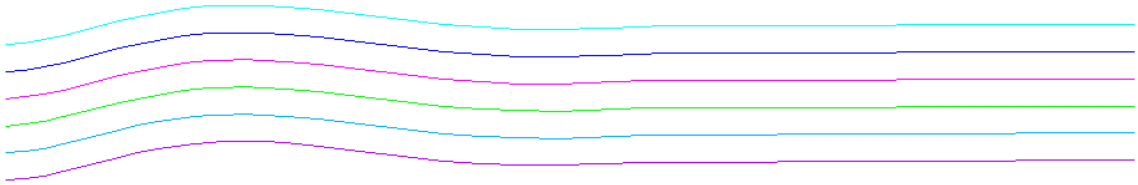

(a) A set of splines modeled for wavy 0° and 90° layers.

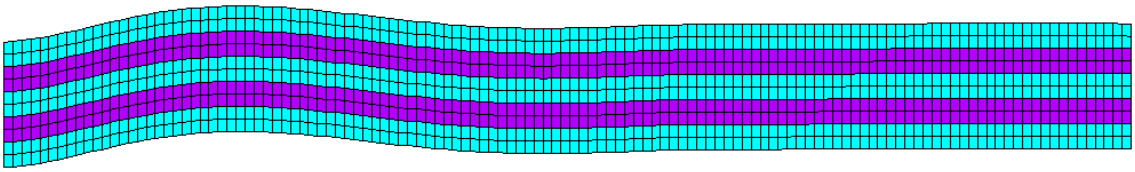

(b) Area meshed with 2-D elements

Figure 4.25 Spline curve.

Table 4.4 Laminates modeled with wavy layers centered about the midplane.

Laminate	Shorthand designation	Total no. of 0° layers	No. of Wavy 0° layers	Total no. of 90° layers	Wave fraction, F_w	Thickness of the laminate (mm)
$[90_2/0_2/90_2/\overline{0_{2w}}]_s$	1~1	3	1	4	0.333	1.78
$[90_2/0_2/90_2/0_{2w}/\overline{90_{2w}}]_s$	1~~1	4	2	5	0.5	2.29
$[90_2/0_2/90_2/0_2/90_2/\overline{0_{2w}}]_s$	2~2	5	1	6	0.2	2.79
$[90_2/0_2/90_2/0_{2w}/90_{2w}/\overline{0_{2w}}]_s$	1~~~1	5	3	6	0.6	2.79
$[90_2/0_2/90_2/0_2/90_2/0_{2w}/\overline{90_{2w}}]_s$	2~~2	6	2	7	0.333	3.30
$[90_2/0_2/90_2/0_{2w}/90_{2w}/0_{2w}/\overline{90_{2w}}]_s$	1~~~~1	6	4	7	0.666	3.30
$[90_2/0_2/90_2/0_2/90_2/0_2/90_2/\overline{0_{2w}}]_s$	3~3	7	1	8	0.143	3.81
$[90_2/0_2/90_2/0_2/90_2/0_{2w}/90_{2w}/\overline{0_{2w}}]_s$	2~~~2	7	3	8	0.4286	3.81
$[90_2/0_2/90_2/0_{2w}/90_{2w}/0_{2w}/90_{2w}/\overline{0_{2w}}]_s$	1~~~~~1	7	5	8	0.714	3.81
$[90_2/0_2/90_2/0_2/90_2/0_2/90_2/0_{2w}/\overline{90_{2w}}]_s$	3~~3	8	2	9	0.25	4.32
$[90_2/0_2/90_2/0_2/90_2/0_{2w}/90_{2w}/0_{2w}/\overline{90_{2w}}]_s$	2~~~~2	8	4	9	0.5	4.32
$[90_2/0_2/90_2/0_2/90_2/0_2/90_2/0_2/90_2/\overline{0_{2w}}]_s$	4~4	9	1	10	0.111	4.83
$[90_2/0_2/90_2/0_2/90_2/0_2/90_2/0_{2w}/90_{2w}/\overline{0_{2w}}]_s$	3~~~3	9	3	10	0.333	4.83
$[90_2/0_2/90_2/0_2/90_2/0_{2w}/90_{2w}/0_{2w}/90_{2w}/\overline{0_{2w}}]_s$	2~~~~~2	9	5	10	0.555	4.83
$[90_2/0_2/90_2/0_2/90_2/0_2/90_2/0_2/90_2/0_{2w}/\overline{90_{2w}}]_s$	4~~4	10	2	11	0.2	5.33
$[90_2/0_2/90_2/0_2/90_2/0_2/90_2/0_2/90_2/0_{2w}/90_{2w}/\overline{0_{2w}}]_s$	4~~~4	11	3	12	0.273	5.84
$[90_2/0_2/90_2/0_2/90_2/0_2/90_2/0_2/90_2/0_2/90_2/\overline{0_{2w}}]_s$	5~5	11	1	12	0.091	5.84
$[90_2/0_2/90_2/0_2/90_2/0_2/90_2/0_2/90_2/0_2/90_2/0_{2w}/\overline{90_{2w}}]_s$	5~~5	12	2	13	0.167	6.35
$[90_2/0_2/90_2/0_2/90_2/0_2/90_2/0_2/90_2/0_2/90_2/0_{2w}/90_{2w}/\overline{0_{2w}}]_s$	5~~~5	13	3	14	0.231	6.86

Table 4.5 Laminates modeled with separated multiple sets of wavy layers [10].

Laminate	Shorthand designation	Total no. of 0° layers	No. of wavy 0° layers	Total no. of 90° layers	Wave fraction, F_w	Thickness of the laminate (mm)
$90_2/0_2/(90_2/0_{2w})_2/90_2/0_2]_s$	1~~2~~1	8	4	9	0.5	4.32
$[(90_2/0_2)_2/90_2/0_{2w}/(90_2/0_2)_2]_s$	2~4~2	10	2	11	0.2	5.33
$[90_2/0_2/(90_2/0_{2w})_3/90_2/0_2]_s$	1~~~2~~~1	10	6	11	0.6	5.33
$[(90_2/0_2)_2/(90_2/0_{2w})_2/(90_2/0_2)_2]_s$	2~~4~~2	12	4	13	0.333	6.35
$[90_2/0_2/(90_2/0_{2w})_2/(90_2/0_2)_2/0_{2w}/\overline{90_{2w}}]_s$	1~~2~~2 ~~1	12	6	13	0.5	6.35
$[90_2/0_2/(90_2/0_{2w})_3/(90_2/0_2)_2/\overline{90_2}/\overline{0_2}]_s$	1~~~5~~~1	13	6	14	0.462	6.86
$[(90_2/0_2)_6/90_2/0_{2w}/\overline{90_{2w}}]_s$	6~~6	14	2	15	0.143	7.37
$[(90_2/0_2)_3/90_2/0_{2w}/(90_2/0_2)_3]_s$	3~6~3	14	2	15	0.143	7.37
$[(90_2/0_2)_2/90_2/0_{2w}/(90_2/0_2)_4]_s$	2~8~2	14	2	15	0.143	7.37
$[(90_2/0_2)_2/(90_2/0_{2w})_3/(90_2/0_2)_2]_s$	2~~~4~~~2	14	6	15	0.429	7.37
$[90_2/0_2/(90_2/0_{2w})_3/(90_2/0_2)_2/0_{2w}/90_{2w}/\overline{0_{2w}}]_s$	1~~~2~~~2 ~~~1	15	9	16	0.6	7.87
$[(90_2/0_2)_5/90_2/0_{2w}/(90_2/0_2)_4/90_2/\overline{0_{2w}}]_s$	5~4~4~5	21	3	22	0.143	10.9
$[(90_2/0_2)_3/90_2/0_{2w}/(90_2/0_2)_6/90_2/\overline{0_{2w}}]_s$	3~6~6~3	21	3	22	0.143	10.9
$[(90_2/0_2)_3/(90_2/0_{2w})_3/(90_2/0_2)_4/\overline{90_2}/\overline{0_2}]_s$	3~~~9~~~3	21	6	22	0.286	10.9
$[90_2/0_2/(90_2/0_{2w})_3/(90_2/0_2)_5/90_2/0_{2w}/90_{2w}/\overline{0_{2w}}]_s$	1~~~5~~~5 ~~~1	21	9	22	0.429	10.9

4.5.2 Progressive Failure Analysis

For predicting the compression failure of composite laminates with layer waviness, progressive failure analyses were performed. To model the formation and growth of interlaminar delaminations under general mixed-mode loading, interface cohesive elements were used. Additionally progressive failure within individual composite lamina was modeled by employing the Hashin failure criteria [9] and reducing material properties of failed elements according to the predicted failure mode. Each of these methods is described in the following sections.

4.5.2.1 Cohesive Elements for Interface Delamination

Initially, a conventional stress analysis was used to identify critical interfaces at which cohesive elements were to be employed. The use of cohesive elements allowed for an initial interface failure based on a stress-based failure criterion, followed by interface crack growth based on a fracture mechanics criterion. The two-dimensional interface elements CONTA171 and TARGE169 in ANSYS used a series of node pairs along the interface of interest. CONTA171 is used to specify contact and sliding between the 2-D "target" surface (TARGE169) [8]. The interface elements were joined along the crack direction from the end of the model to the remaining model length.

Input properties required for the cohesive elements were obtained from composite strength properties as well as fracture toughness values (G_{Ic} and G_{IIc}). Mode I Double Cantilever Beam (DCB) tests and Mode II End-Notched Flexure (ENF) tests were performed using the same IM7/8551-7A carbon/epoxy used to fabricate the layer waviness specimens. The cohesive element input properties used were listed in Table 4.1.

4.5.2.2 Laminar Progressive Failure

In this research a first-ply failure may consist of a matrix failure (90° composite layer), a delamination of a layer interface, or even a fiber failure (0° composite layer). To model the formation and growth of interface delaminations, progressive failure within the individual 0° and 90° composite layers was modeled by employing the Hashin failure criteria [9]. Failure of the 90° layers was predicted using the transverse normal strength, Y_t or Y_c and interlaminar shear strength S using the following expressions:

For tensile failure: $\sigma_2 + \sigma_3 > 0$

$$\frac{(\sigma_2 + \sigma_3)^2}{Y_t^2} + \frac{\sigma_{23}^2 - \sigma_2\sigma_3}{S_{23}^2} = \begin{cases} \geq 1 & failure \\ < 1 & no\ failure \end{cases} \tag{4.1}$$

For compressive failure: $\sigma_2 + \sigma_3 < 0$

$$\left[\left(\frac{Y_c}{2S_{23}}\right)^2 - 1\right]\left(\frac{\sigma_2 + \sigma_3}{Y_c}\right) + \frac{(\sigma_2 + \sigma_3)^2}{4S_{23}^2} + \frac{\sigma_{23}^2 - \sigma_2\sigma_3}{S_{23}^2} = \begin{cases} \geq 1 & failure \\ < 1 & no\ failure \end{cases}, \tag{4.2}$$

where σ_2 and σ_3 are the interlaminar normal stresses and σ_{23} is the interlaminar shear stress. A progressive damage analysis may be performed on the "failed" element(s) using a material degradation approach. If the failed 90° composite lamina element is identified at the certain load step before fiber failure occur, appropriate material properties of that element are reduced using appropriate degradation factors. To represent a failed 90° composite lamina element, E_2 and E_3 were reduced to 1% as well as G_{12} and G_{13} were reduced to 10% of their initial values. An incremental analysis is thus performed, such that elements are checked for failure and degraded if necessary at each load step.

The Hashin failure criterion [9] for fiber failure reduces to the maximum stress criterion if the contribution of shear stresses is not considered. This reduced failure criterion was used to predict fiber failure of the 0° composite lamina. Thus, failure was predicted when the longitudinal stress exceeds the longitudinal tensile or compressive strength, X_t or X_c, according to the following expression:

$$\left(\frac{1}{X_t}-\frac{1}{X_c}\right)\sigma_1+\left(\frac{1}{X_tX_c}\right)\sigma_1^2=\begin{cases}\geq 1 & failure\\ <1 & no\ failure\end{cases}, \tag{4.3}$$

where σ_1 is the longitudinal stress. If a failed 0° composite lamina element was identified at the certain load step, all elastic properties of that element (E_1, E_2, E_3, v_{12}, v_{13}, v_{23}, G_{12}, G_{13}, and G_{23}) were reduced to 1% of their original values.

For predicting interface failure and subsequent delamination growth, cohesive elements will be used. Initially, a conventional stress analysis is used to identify critical interfaces for which cohesive elements are to be employed. Such cohesive elements allow for an initial interface failure based on a stress-based failure criterion, followed by interface crack growth based on a fracture mechanics criterion. These elements simulate the behavior of a bonded interface until the element force reaches a critical stress value (interface failure), and then simulate the behavior of a debonded interface after this critical force value has been reached.

A series of finite element models were developed to analyze all of the cross-ply laminates with layer waviness listed in Table 4.4 and Table 4.5. The finite element modeling methodology presented in this chapter was used to identify the location of initial damage formation, describe the progression of damage under increasing

compressive load, and predict the ultimate compressive strength. Results obtained using finite element analyses are summarized in the following sections.

4.5.3 Analysis of Areas Susceptible to Damage Formation

Finite element analysis was performed to predict the compressive strength reductions for wavy composite laminates. Subsequently, the predictions will be compared with the experimental result from references [4] and [10] as well as from compression testing performed in this research investigation. Initially, the finite element modeling was performed to predict the location of initial failure or first-ply failure. The Hashin failure criteria [9] was employed to identify the region of initial damage formation under compression loading. Next, cohesive elements were used to investigate delamination propagation in the critical regions of the initial damage formation identified.

To identify the critical areas of initial failure, regions of high interlaminar normal and shear stresses, σ_{n} and τ_{ns} respectively were identified. Two regions associated with the layer waviness formations were identified. These regions are visible in contour plots of interlaminar normal and shear stresses. Figure 4.26, Figure 4.27, and Figure 4.28 show these interlaminar stress contour plots for the $[90_2/0_2/90_2/0_2/90_2/\overline{0}_{2w}]_{\mathrm{s}}$ (2~2), $[90_2/0_2/90_2/0_2/90_2/0_2/90_2/0_{2\mathrm{w}}/90_{2\mathrm{w}}/\overline{0_{2w}}]_{\mathrm{s}}$ (3~~~3), and $[90_2/0_2/(90_2/0_{2\mathrm{w}})_3/90_2/0_2]_{\mathrm{s}}$ (1~~~2~~~1) layer waviness models, respectively. Stresses are nondimensionalized by the magnitude of the applied compressive stress, $\left|\overline{\sigma_x}\right|$, defined as the total applied compressive force divided by the cross-sectional area of the laminate. Beyond the right ends of the region plotted, the effect of the layer waviness was negligible and did not result in additional stress contours.

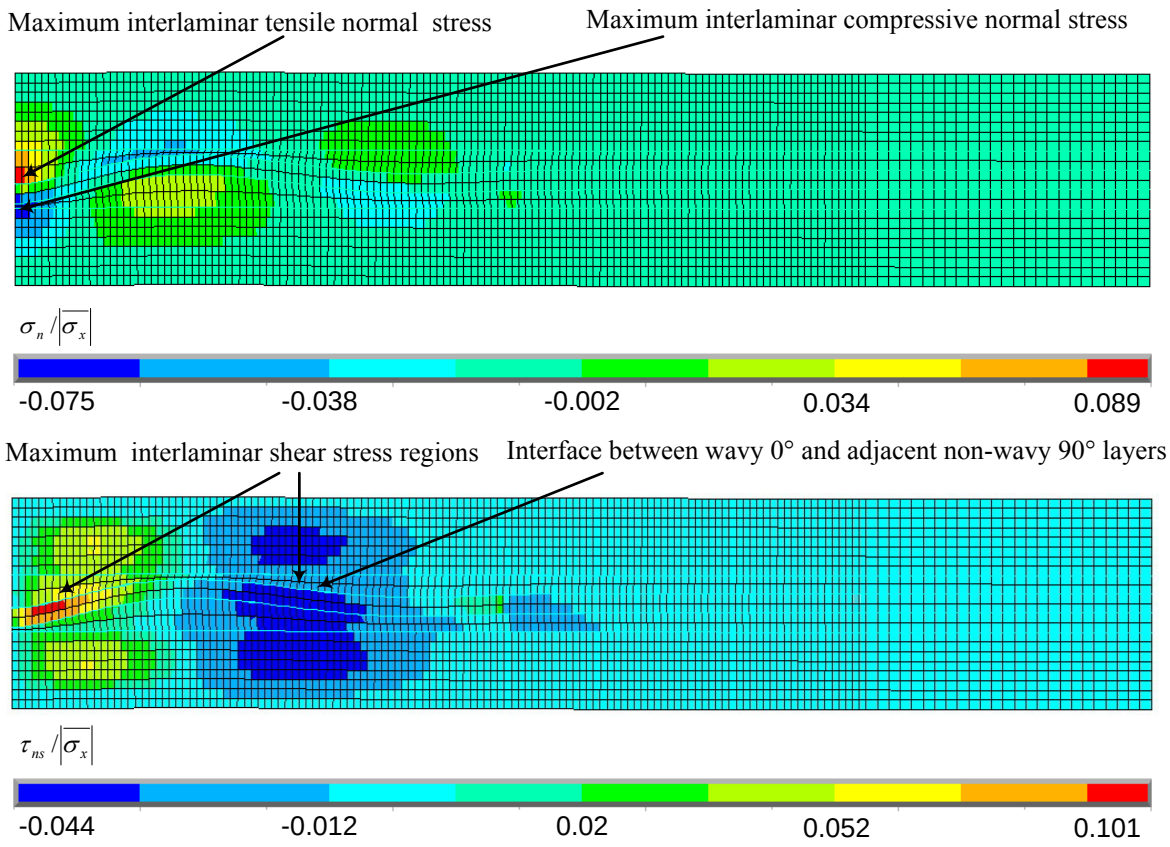

Figure 4.26 Normalized σ_n and τ_{ns} contour plot for 2~2 laminate.

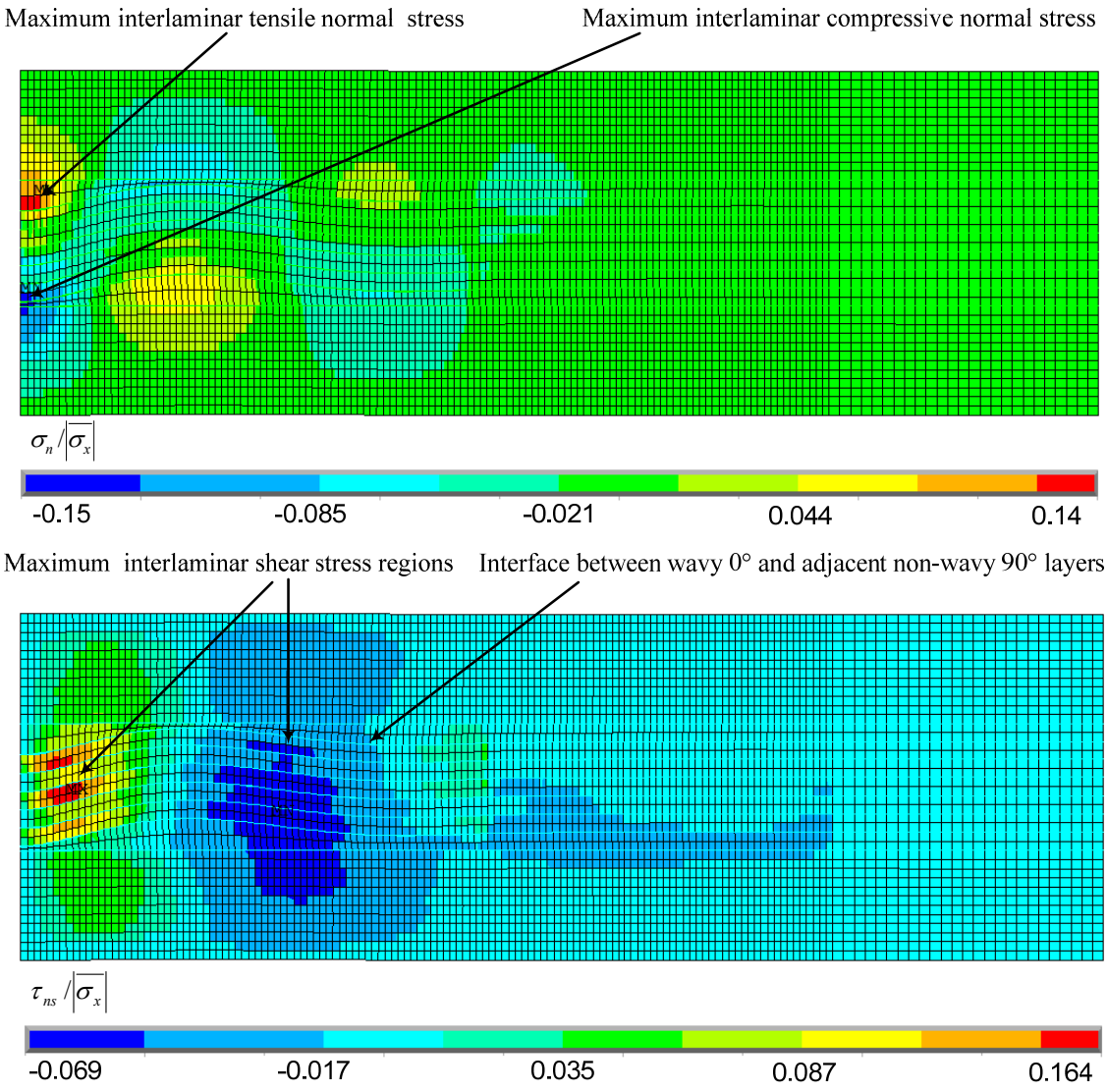

Figure 4.27 Normalized σ_n and τ_{ns} contour plot for 3~~~3 laminate.

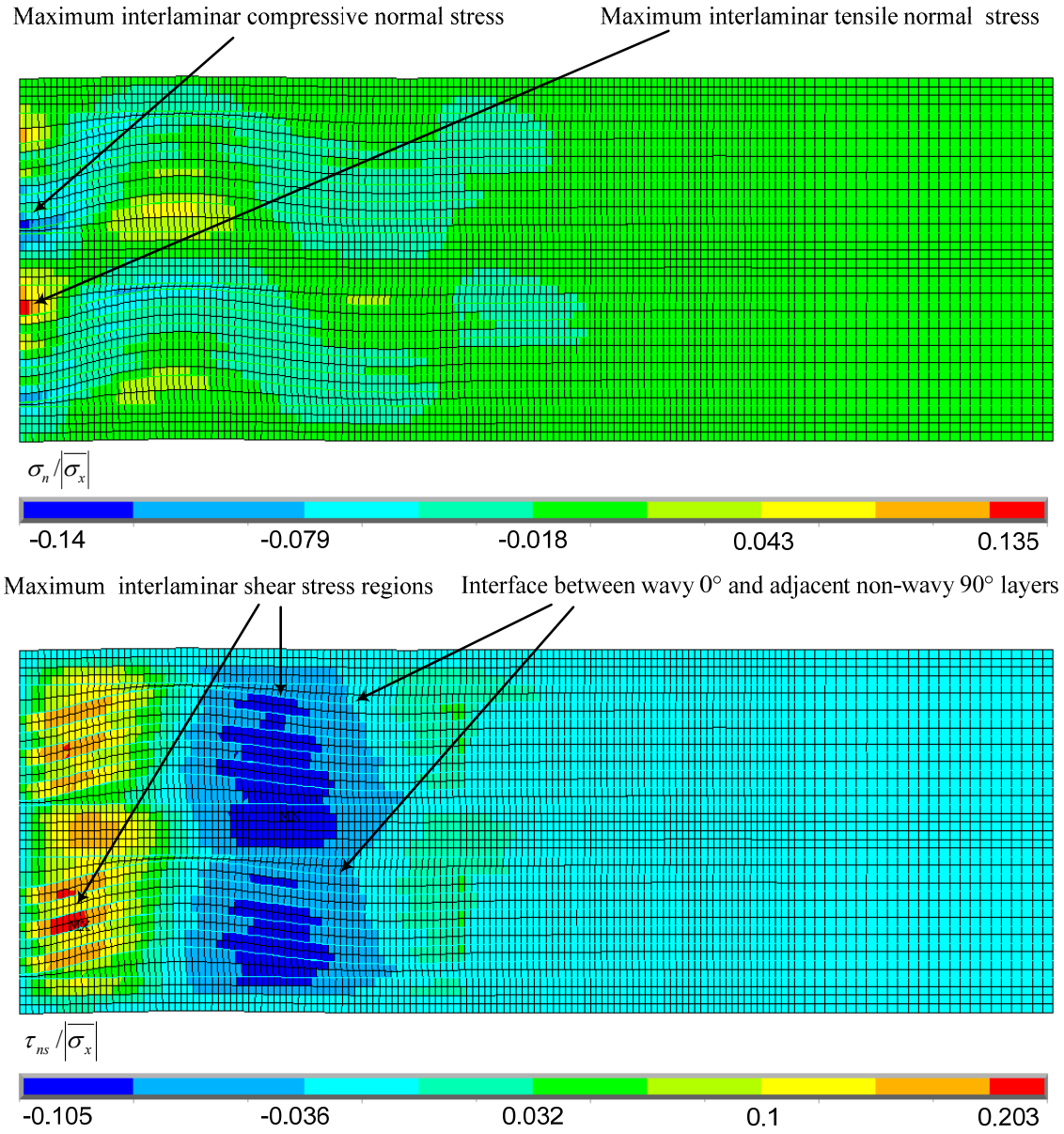

Figure 4.28 Normalized σ_n and τ_{ns} contour plot for 1~~~2~~~1 laminate.

The locations of the highest interlaminar normal and shear stresses for all layer waviness models were in similar areas relative to the wavy layers. There are two critical regions of high interlaminar stresses, which were identified. The first region is associated with the location of maximum interlaminar normal stresses. For composite laminates of varying laminate thickness with layer waviness centered about the laminate midplane, the location of maximum interlaminar normal tensile stress was identified near the plane of symmetry, in the center of the 90° layer immediately above the top wavy 0° layer as shown in Figure 4.26 and Figure 4.27. Correspondingly, the location of maximum interlaminar normal compressive stress was identified near the plane of symmetry, in the center of the 90° layer immediately below the bottom wavy 0° layer. For the laminates having separated multiple wavy layers, the location of maximum interlaminar normal tensile stress was also identified near the plane of symmetry. The maximum tensile stress, located within the lower set of wavy layers, occurred in the center of the 90° layer immediately above the top wavy 0° layer as shown in the Figure 4.28. Correspondingly, the location of maximum interlaminar normal compressive stress was identified within the upper set of wavy layers, and in the center of the 90° layer below the bottom wavy 0° layer.

The second region of high interlaminar stress is associated with the location of the maximum interlaminar shear stresses. For the composite laminates of varying laminate thickness with layer waviness centered about the laminate midplane, the maximum interlaminar shear stresses occurred where the slope of the wavy 0° layers was maximum as shown in Figure 4.26 and Figure 4.27.

For the laminates having separated multiple wavy layers, the maximum interlaminar shear stresses occurred within the wavy layers where the slope is maximum as shown in Figure 4.28. This position of maximum slope is also the inflection point of the wavy 0° layers, midway between the central trough and adjacent crest of the wave. These two regions of the maximum interlaminar stresses were considered as the critical areas for initial failure under an applied compression load. Values of the maximum interlaminar stresses (interlaminar tension, compression, and shear) for a variety of layer waviness formations centered about the laminate midplane are presented in Table 4.6. These layer waviness formations are categorized as laminates which contains single, double, or triple wavy 0° layers. An increasing number of nonwavy 0° layers was modeled with the single, double, and triple wavy layer formations listed in Table 4.6.

Figure 4.29 and Figure 4.30 show the maximum values of compressive and tensile interlaminar normal stress, respectively, as a function of wave fraction, F_w. With the exception of the thinnest laminates with only one nonwavy 0° layer near the outside surfaces of the laminates (1~1, 1~~1, and 1~~~1), both the compressive and tensile values of the maximum interlaminar normal stress remained relatively constant with increases in wave fraction. For the thinnest laminates, (1~1, 1~~1, and 1~~~1), however, the maximum interlaminar normal stress values are reduced relative to laminates with higher wave fractions. These reductions are believed to result from bending produced during compression loading.

Figure 4.31 shows that the maximum interlaminar shear stress values as a function of wave fraction, F_w. The magnitude of the maximum interlaminar shear stress is shown to increase with increasing wave fraction.

Table 4.6 Stress values for a variety of layer waviness model with different wave fraction.

Laminates	Configuration for laminates	Shorthand designation	Wave fraction, F_w	Maximum compressive stress ($\sigma_n/\lvert\overline{\sigma_x}\rvert$)	Maximum tensile stress ($\sigma_n/\lvert\overline{\sigma_x}\rvert$)	Maximum shear stress ($\tau_{ns}/\lvert\overline{\sigma_x}\rvert$)
Single wave	$[90_2/0_2/90_2/\overline{0_{2w}}]_s$	1~1	0.333	-0.06	0.08	0.128
	$[90_2/0_2/90_2/0_2/90_2/\overline{0_{2w}}]_s$	2~2	0.2	-0.075	0.089	0.101
	$[90_2/0_2/90_2/0_2/90_2/0_2/90_2/\overline{0_{2w}}]_s$	3~3	0.143	-0.078	0.09	0.094
	$[90_2/0_2/90_2/0_2/90_2/0_2/90_2/0_2/90_2/\overline{0_{2w}}]_s$	4~4	0.111	-0.079	0.09	0.091
	$[90_2/0_2/90_2/0_2/90_2/0_2/90_2/0_2/90_2/0_2/90_2/\overline{0_{2w}}]_s$	5~5	0.091	-0.08	0.087	0.09
Double wave	$[90_2/0_2/90_2/0_{2w}/\overline{90_{2w}}]_s$	1~~1	0.5	-0.103	0.1	0.178
	$[90_2/0_2/90_2/0_2/90_2/0_{2w}/\overline{90_{2w}}]_s$	2~~2	0.333	-0.121	0.123	0.14
	$[90_2/0_2/90_2/0_2/90_2/0_2/90_2/0_{2w}/\overline{90_{2w}}]_s$	3~~3	0.25	-0.125	0.121	0.132
	$[90_2/0_2/90_2/0_2/90_2/0_2/90_2/0_2/90_2/0_{2w}/\overline{90_{2w}}]_s$	4~~4	0.2	-0.125	0.12	0.129
	$[90_2/0_2/90_2/0_2/90_2/0_2/90_2/0_2/90_2/0_2/90_2/0_{2w}/\overline{90_{2w}}]_s$	5~~5	0.167	-0.125	0.12	0.127
Triple wave	$[90_2/0_2/90_2/0_{2w}/90_{2w}/\overline{0_{2w}}]_s$	1~~~1	0.6	-0.118	0.11	0.213
	$[90_2/0_2/90_2/0_2/90_2/0_{2w}/90_{2w}/\overline{0_{2w}}]_s$	2~~~2	0.429	-0.144	0.135	0.174
	$[90_2/0_2/90_2/0_2/90_2/0_2/90_2/0_{2w}/90_{2w}/\overline{0_{2w}}]_s$	3~~~3	0.333	-0.15	0.14	0.164
	$[90_2/0_2/90_2/0_2/90_2/0_2/90_2/0_2/90_2/0_{2w}/90_{2w}/\overline{0_{2w}}]_s$	4~~~4	0.273	-0.15	0.15	0.159
	$[90_2/0_2/90_2/0_2/90_2/0_2/90_2/0_2/90_2/0_2/90_2/0_{2w}/90_{2w}/\overline{0_{2w}}]_s$	5~~~5	0.231	-0.15	0.144	0.156

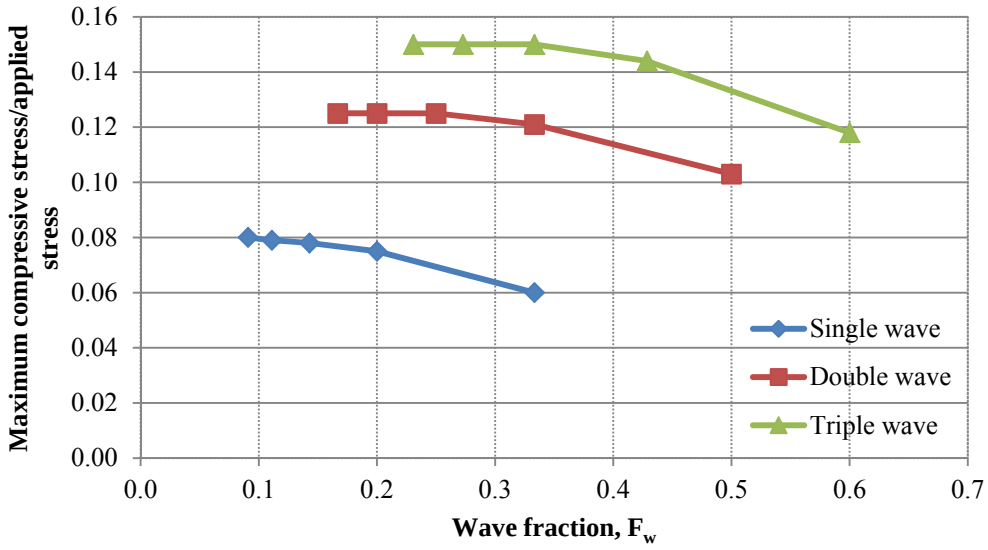

Figure 4.29 Variation of maximum compressive interlaminar normal stress with wave fraction.

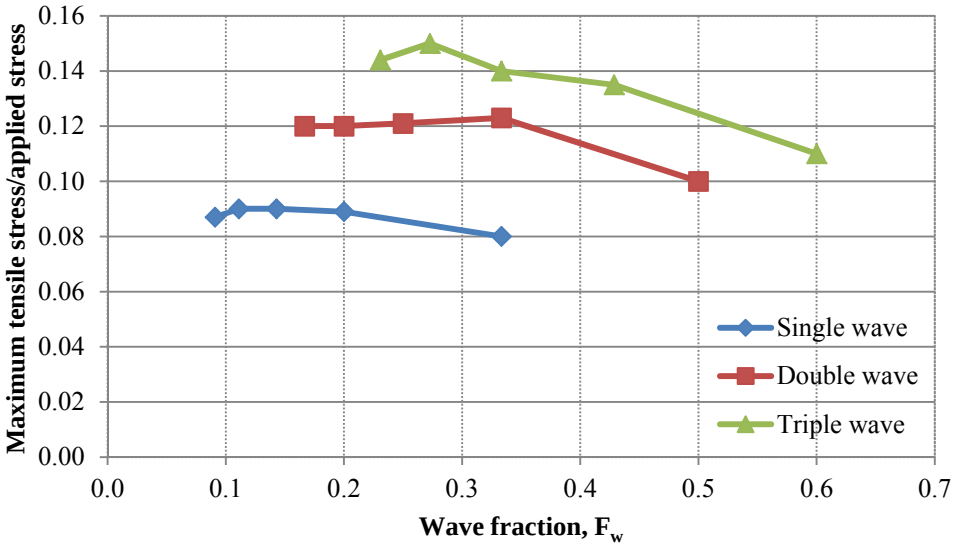

Figure 4.30 Variation of maximum tensile interlaminar normal stress with wave fraction.

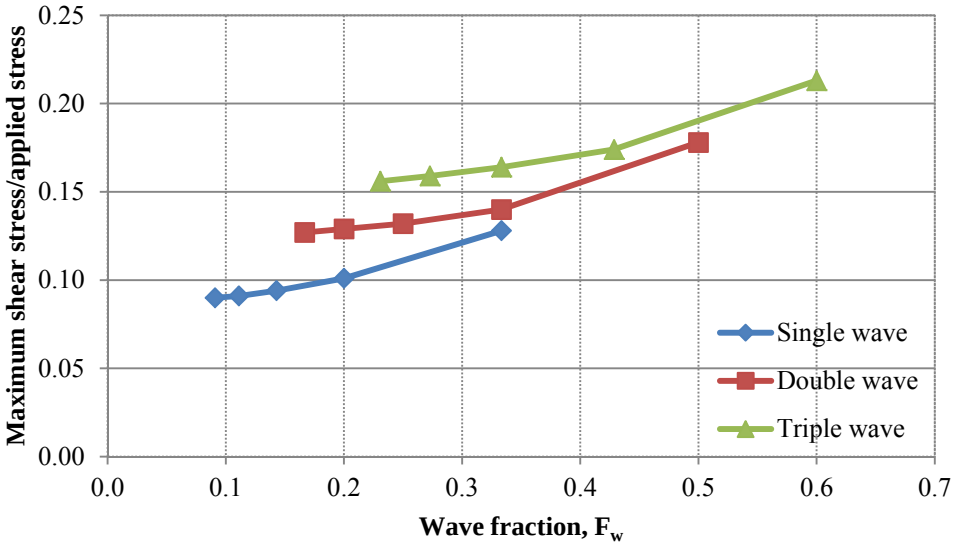

Figure 4.31 Variation of maximum interlaminar shear stress with wave fraction.

An additional comparison between the single, double, and triple wavy 0° layer formations was made by considering equal number of nonwavy 0° layers on either side of the central wavy 0° layer formation within the cross-ply laminate. Figure 4.32 compares the maximum interlaminar normal and shear stresses for the thinnest laminates with one nonwavy 0° layer on either side of the central wavy 0° layer formation: 1~1, 1~~1, and 1~~~1. Similarly, Figure 4.33 compares the maximum interlaminar stresses for thicker laminates with five nonwavy 0° layers on either side of the laminate: 5~5, 5~~5, and 5~~~5. For both sets of laminates, the maximum interlaminar normal and shear stress values increase as the number of wavy 0° layers at the center of the laminate increases. These results suggest that the presence of multiple "stacked" wavy 0° layers may produce a greater compression strength reduction in comparison with single wavy 0° layers of the same severity.

4.5.4 Predictions of First-ply Failure

Using a conventional finite element analysis suitable for stress analysis, the initial "first-ply" failure in a laminate may be predicted using a selected failure criterion. As discussed in section 4.5.2, the first-ply failure can be a 90° layer failure, a layer interface failure, or a 0° layer failure. For the laminates modeled with layer waviness, a first-ply failure strength ratio (F_{fp}) was defined as the ratio of applied stress at first-ply failure to the predicted ultimate strength of the wave-free laminate. First-ply failure strength ratios (F_{fp}) of the laminates with layer waviness were analyzed based on Hashin failure criteria. As discussed previously, matrix failure is based on the transverse tensile normal strength

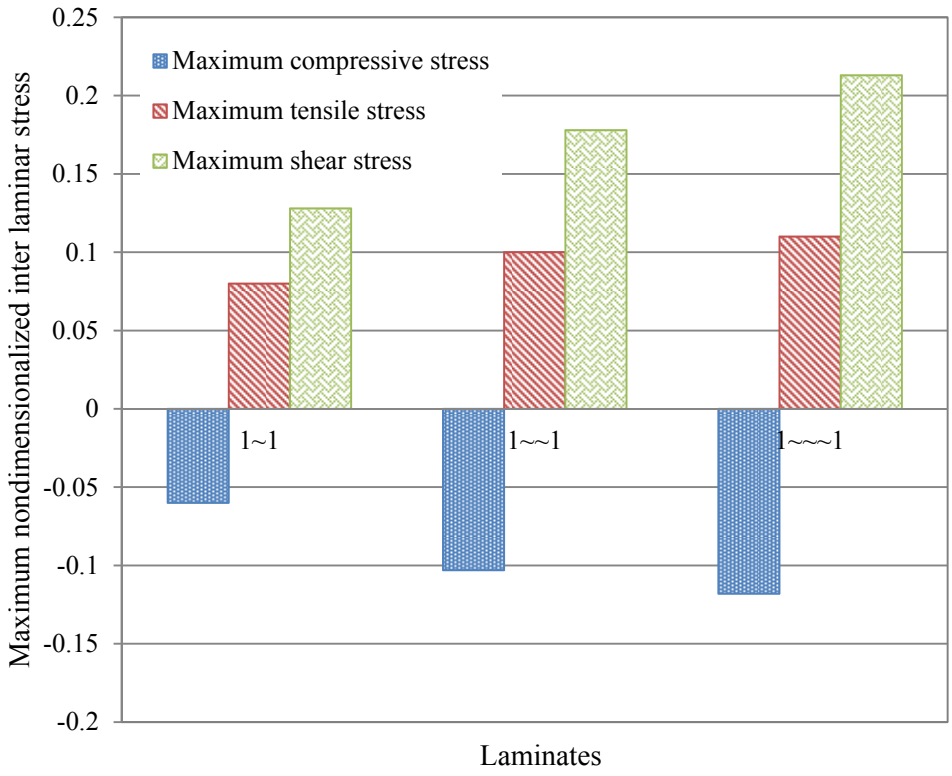

Figure 4.32 Comparison of maximum interlaminar stresses for one nonwavy 0° layer laminates.

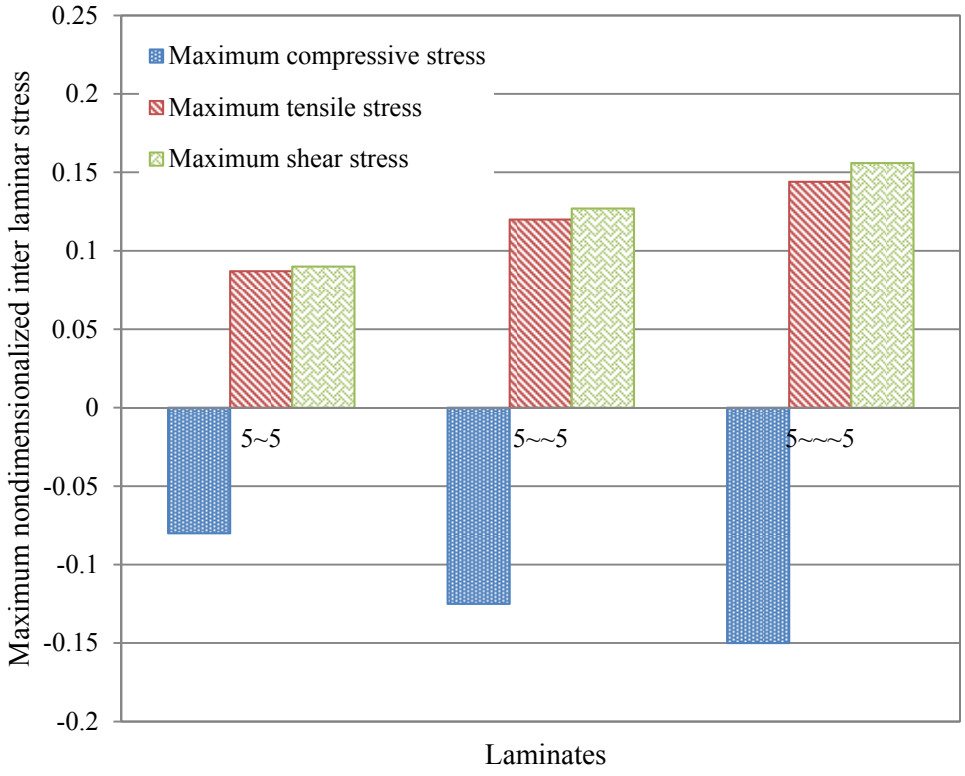

Figure 4.33 Comparison of maximum interlaminar stresses for five nonwavy 0° layers laminates.

(Y_t), the transverse compressive normal strength (Y_c), and the interlaminar shear strength (S). Based on the maximum stress criterion, compressive fiber failure is predicted when the longitudinal compressive stress exceeds the longitudinal compressive strength (X_c). The above strength values were input into an ANSYS user subroutine for the purpose of identifying the initial failed element(s) and the corresponding applied stress level. Although not required, the use of cohesive elements allowed for the determination of initial failure at the layer interfaces based on a stress-based failure criterion.

First-ply failure analyses were performed for all of the layer waviness formations at the laminate midplane listed in Table 4.6. Interface failure was identified as the first-ply failure for all layer wave formations investigated with the exception of the 1~1, 1~~1, and 1~~~1 formations. Matrix failures in a 90° layer occurred prior to interface failure in the 1~1, 1~~1, and 1~~~1 formations. To illustrate the stress state producing first-ply failure, two representative layer wave formations are considered: the 2~2 and 3~~~3 laminates. Contour plots of interlaminar shear and normal stresses for these two laminates were presented previously in Figure 4.26 and Figure 4.27. Additionally, contour plots of the nondimensionalized compressive stress in the loading direction, σ_c, for the two laminates are presented in Figure 4.34. The highest compressive stress values in the 0° layers were located along the central plane of the layer waviness formation, either in one of the wavy 0° layers or an adjacent nonwavy 0° layer. As shown previously, the highest tensile interlaminar normal stresses were located near the central trough of the layer waviness, at the interface between the uppermost wavy 0° layer and the top adjacent 90° layer. Additionally, the regions of highest interlaminar shear stresses were produced along the wavy 0° layer interfaces where their slope was maximum.

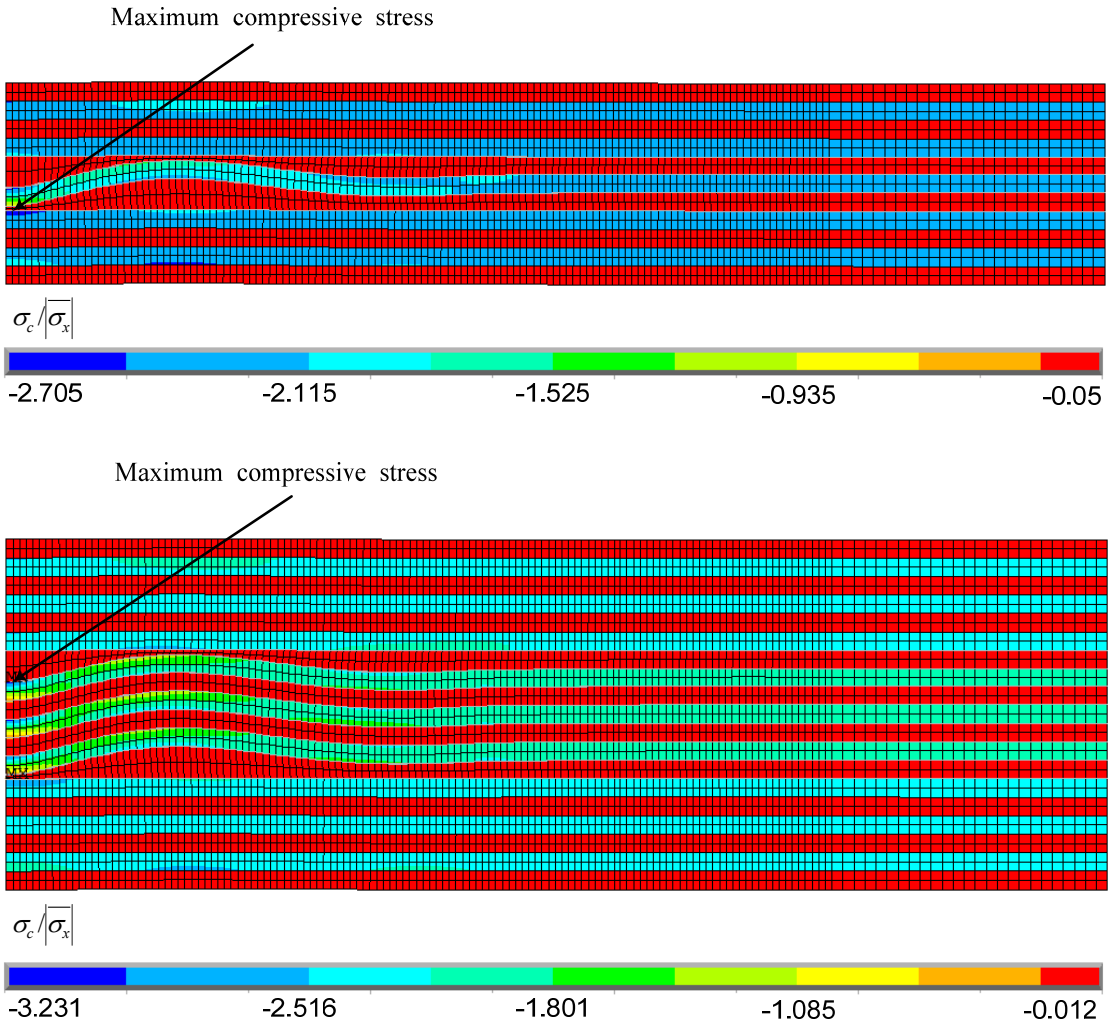

Figure 4.34 Normalized σ_c contour plot for 2~2 and 3~~~3 laminates.

4.5.5 Failure Progressions

Following the initial interface failure in all layer wave formations investigated (with the exception of the 1~1, 1~~1, and 1~~~1 formations), delaminations were predicted to propagate until ultimate fiber failure occurred in the 0° layers. During the failure progression, failure of the 90° layers (matrix failures) were identified in all layer wave formations investigated with the exception of the 2~2, 3~3, 4~4, 5~5, and 2~~2 formations. Figure 4.35 shows the delamination produced following initial failure above the wavy 0° layers in the 2~~~2 layer waviness model. Following the formation of this initial delamination, the input load was increased incrementally. The delamination, modeled using interface cohesive elements, subsequently propagated along the layer interface. Delamination lengths in laminates having single and double wavy 0° layer extended to a maximum length of 7 element lengths (0.640 mm) versus 10 element lengths (0.914 mm) for laminates with triple wavy 0° layers.

Following the initial delamination above the wavy 0° layer in the 2~~~2 layer waviness model, elements within the 90° layers failed both above and below the wavy 0° layers as shown in Figure 4.36(a). The material properties of these failed elements (pink colored elements) were reduced using the prescribed degradation factors, and the loading was increased incrementally. Figure 4.36(b) and Figure 4.36(c) show the progression of matrix failure in the 90° layers with increased loading, prior to ultimate laminate failure. Note that at the damage state shown in Figure 4.36(c), both interface delamination as well as 90° element failure is present in the model without any fiber failure in any of the 0° layers.

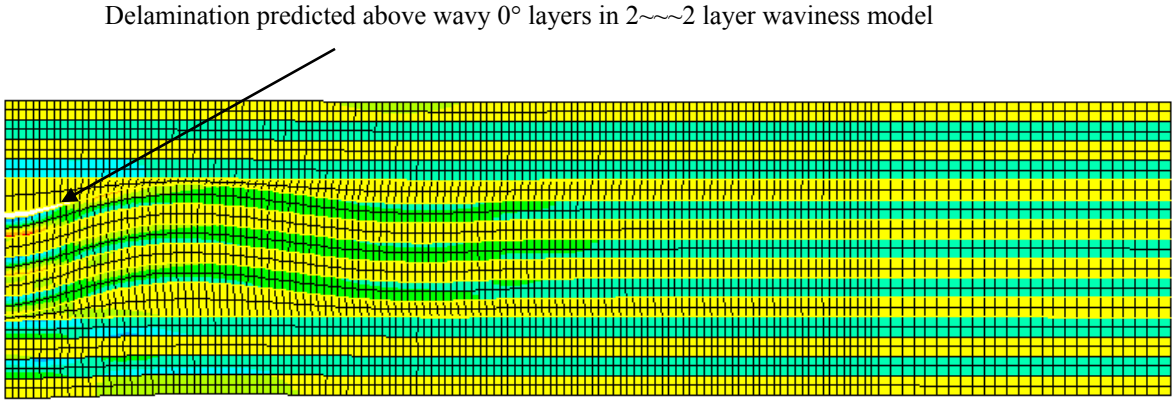

Figure 4.35 Delamination above wavy 0° layers in 2~~~2 layer waviness model.

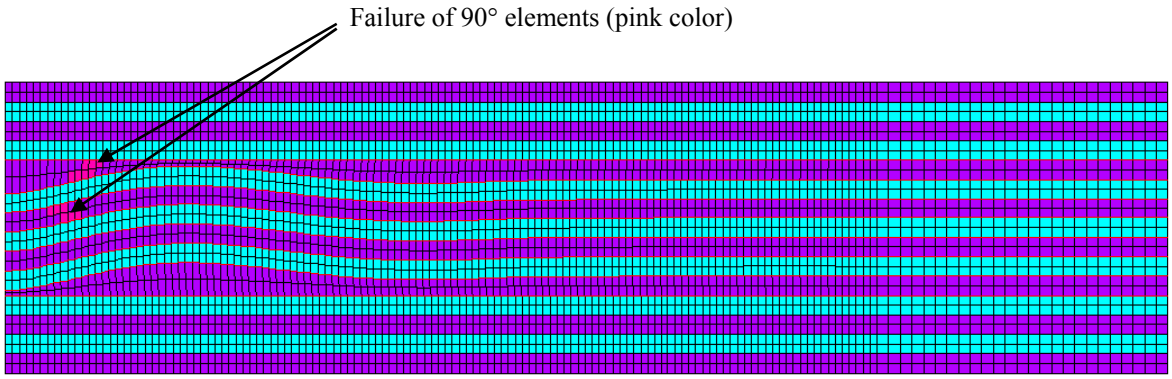

(a) Initial failure of 90° elements of 2~~~2 layer waviness model.

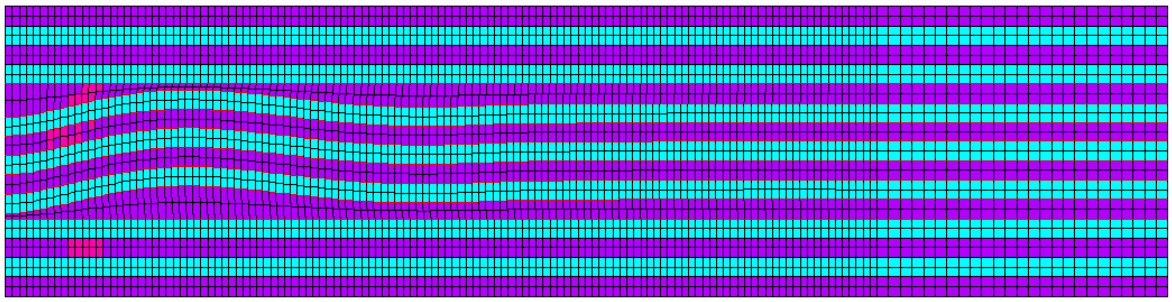

(b) Progressive failure of 90° elements of 2~~~2 layer waviness model.

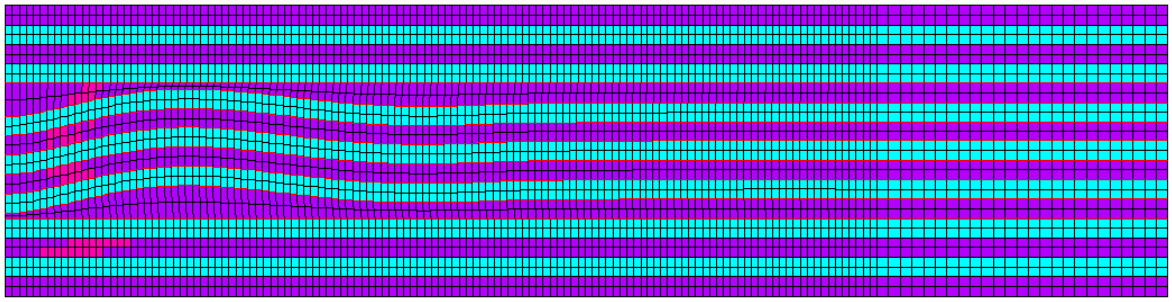

(c) Continued progressive failure of 90° elements of 2~~~2 layer waviness model.

Figure 4.36 Progressive failure of the 90° elements for 2~~~2 layer waviness model.

4.5.6 Predictions of Ultimate Failure

After predicting first-ply failure using the Hashin failure criteria and subsequent progressive failure analysis, ultimate failure was predicted for all laminates investigated with layer waviness formations. The maximum stress failure criterion was used to predict fiber failure of the 0° layers; failure was predicted when the longitudinal compression stress exceeds the longitudinal compressive strength, X_c.

The progression of damage leading to ultimate failure is once again illustrated using the 2~~~2 layer waviness model. The initial fiber failures within a 0° layer is indicated by the green colored elements in Figure 4.37(a). For this laminate, the first failure of a 0° layer element occurred above the failed 90° elements. Following the reduction of material properties for the failed elements, an additional load increment was applied and the failure progression continued. Additional failed 90° and 0° elements were identified prior to ultimate failure as shown in Figure 4.37(b) and Figure 4.37(c). Following this one additional load step, ultimate failure occurred for the laminate.

As shown in Figure 4.37, both 90° and 0° elements failed in the wavy layer region prior to ultimate failure of the laminate. The resulting predicted stress versus strain response of the 2~~~2 layer waviness model is shown in Figure 4.38. A relatively linear stress versus strain response is observed until the maximum stress at which fiber failure occurred. The stress levels corresponding to the onset of delamination, matrix failure and fiber failure for this laminate are indicated. Similar stress-strain relationships were predicted for all laminates modeled. However, differences existed in the progression of damage; in some laminates, failure of 90° layer elements occurred prior to the onset of delamination as discussed previously.

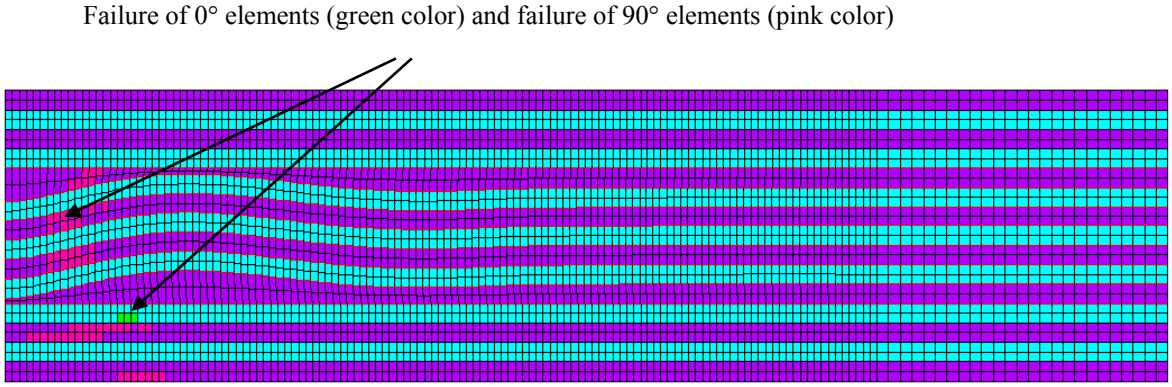

(a) Initial failure of 0° elements of 2~~~2 layer waviness model.

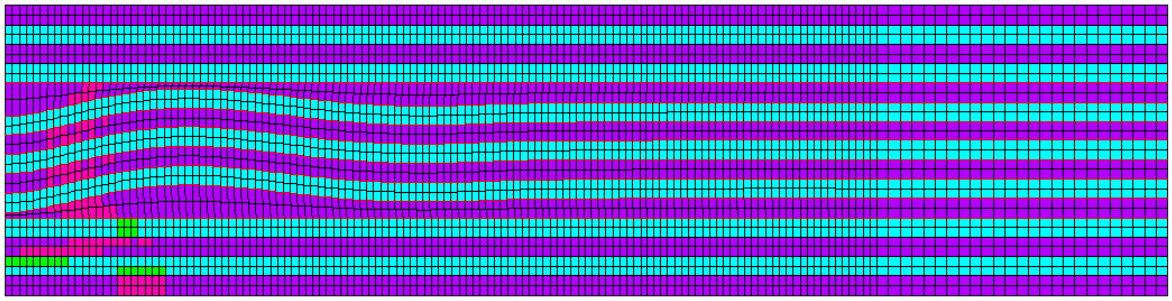

(b) Progressive failure of 0° and 90° elements of 2~~~2 layer waviness model.

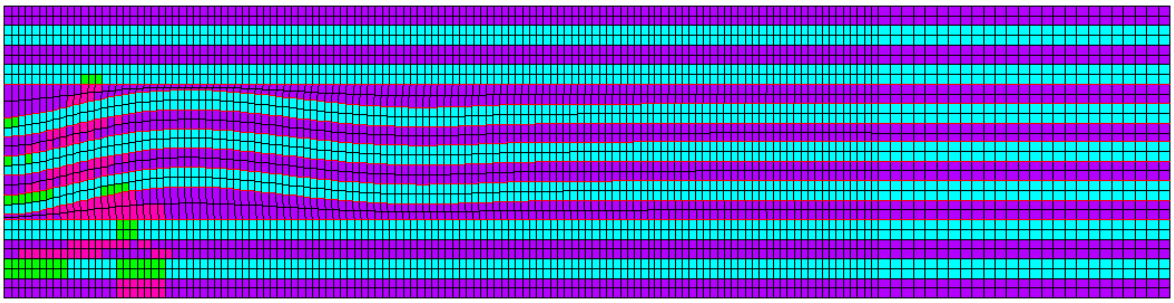

(c) Continued progressive failure of 0° and 90° elements of 2~~~2 layer waviness model.

Figure 4.37 Progressive failure of the 0° layers leading to ultimate failure, 2~~~2 layer waviness model.

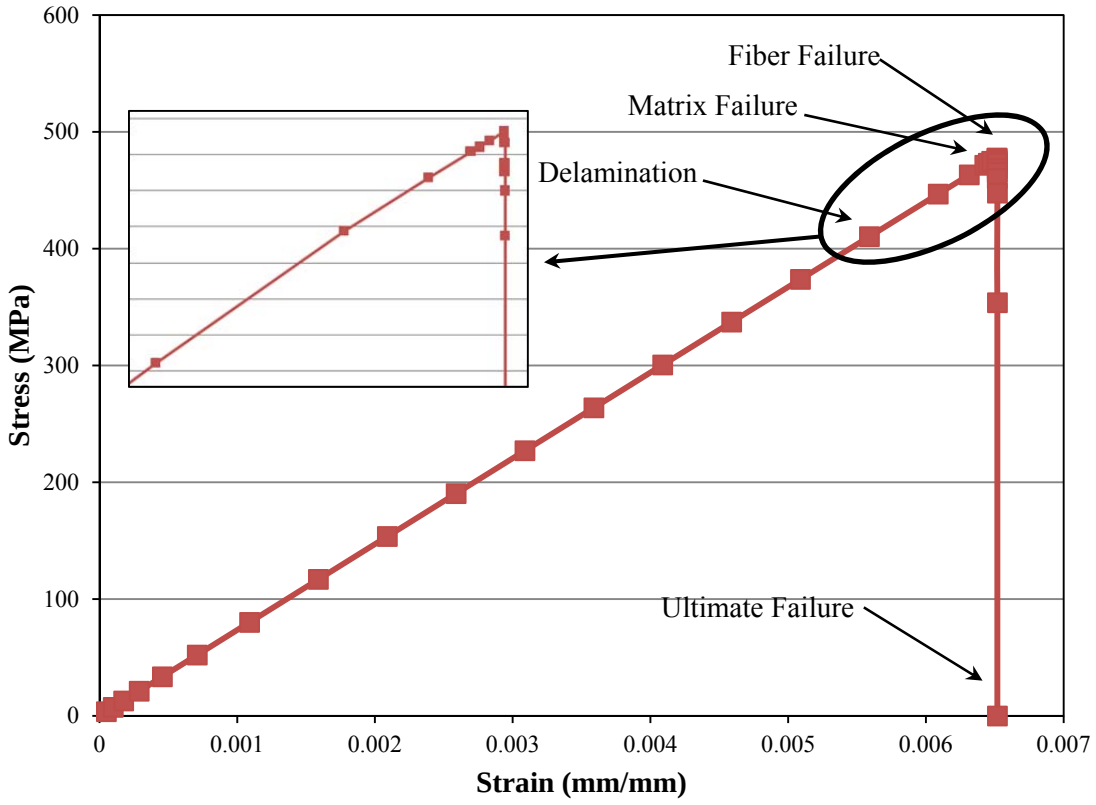

Figure 4.38 Stress versus strain response of 2~~~2 layer waviness model.

Table 4.7 compares first-ply failure predictions with ultimate strength predictions for the composite laminates with layer waviness centered about the laminate midplane. The first-ply (F_{fp}) and ultimate (F_u) compression strength ratios presented are defined as the ratio of the predicted failure strength of a laminate with waviness to the predicted failure strength of that laminate without waviness.

With the exception of the thinnest 1~1 laminate, first-ply compression strength ratios (F_{fp}) for laminates containing single wavy 0° layers ranged from 0.841 to 0.850, corresponding to a first-ply strength reduction from 15.0% to 15.9%. For the 1~1 laminate, the first-ply strength ratios was 0.548, a 45.2% strength reduction. This greater strength reduction in this 1~1 laminate is believed to be caused by the bending produced in this relatively thin laminate due to the localized laminate nonsymmetry at the location due to the layer waviness. Ultimate compression strength ratios (F_u), for laminates containing single wavy 0° layers varied from 0.863 to 0.926, corresponding to ultimate strength reductions from 7.4% to 13.7%. For the 1~1 laminate, an ultimate strength ratio of 0.544 was predicted, a 45.6% strength reduction.

First-ply strength reductions in laminates containing double and triple wavy 0° layers ranged from 37.5% to 43.4% and from 44.8% to 48.8%, respectively. Ultimate strength reduction in laminates containing double and triple wavy 0° layers ranged from 23.9% to 35.6% and from 34.3% to 36.7%, respectively.

Comparing the sets of laminates with single, double and triple wavy 0° layers, the first-ply and ultimate strength reductions greatly increase as the number of wavy 0° layers increases as shown in Table 4.7.

Table 4.7 Predicted compression strengths for laminates with layer waviness centered about the laminate midplane.

Laminate	Total no. of 0° layers	No. of wavy 0° layers	Wave fraction, F_w	Predicted ultimate strength (wave free) (MPa)	First-ply failure			Ultimate failure		
					Stress (MPa)	Strength ratio, F_{fp}	Strength reduction (%)	Stress (MPa).	Strength ratio, F_u	Strength reduction (%)
1~1	3	1	0.333	689	378	0.548	45.2	375	0.544	45.6
2~2	5	1	0.2	726	617	0.850	15.0	627	0.863	13.7
3~3	7	1	0.143	743	625	0.841	15.9	666	0.896	10.4
4~4	9	1	0.111	753	634	0.843	15.7	697	0.926	7.40
5~5	11	1	0.091	759	641	0.844	15.6	693	0.913	8.67
1~~1	4	2	0.5	712	403	0.566	43.4	459	0.644	35.6
2~~2	6	2	0.333	736	448	0.609	39.1	560	0.761	23.9
3~~3	8	2	0.25	749	462	0.617	38.3	526	0.703	29.7
4~~4	10	2	0.2	756	471	0.623	37.7	554	0.733	26.7
5~~5	12	2	0.167	762	476	0.625	37.5	569	0.747	25.3
1~~~1	5	3	0.6	726	382	0.527	47.3	476	0.656	34.4
2~~~2	7	3	0.429	743	410	0.552	44.8	470	0.633	36.7
3~~~3	9	3	0.333	753	407	0.541	45.9	478	0.634	36.6
4~~~4	11	3	0.273	759	388	0.512	48.8	489	0.643	35.7
5~~~5	13	3	0.231	764	391	0.512	48.8	502	0.657	34.3

Values obtained for ultimate failure strength ratio, F_u, for every set of laminate containing single, double and triple wavy 0° layers are greater than corresponding first-ply failure strength ratio, F_{fp}. Additionally, different values for first-ply and ultimate failure strength ratios were obtained for laminates with different layer wave formations, but having same wavy 0° layer fraction, F_w (0.20 or 0.33). This result suggests that the prediction of compression strength reductions due to layer waviness cannot be based solely on the wavy 0° layer fraction, F_w. The compression strength predictions for laminates with layer waviness centered about the laminate midplane are compared with experimental results in the following section.

4.5.7 Comparison of Experimental, First-ply and Ultimate Failure Strength Results

Table 4.8 presents a comparison of finite element predictions with mechanical test results published previously by Adams and Bell [4]. The object of these static compression tests was to determine the effects of multiple layer wave regions on compression strength. Four different thicknesses of cross-ply laminates with intentionally-fabricated layer waviness were tested. Although the wave fraction F_w was varied, the layer wave severity, δ/λ was held constant (average δ/λ = 0.07). It is noted that the 4~~4 laminate listed in Table 4.8 was fabricated and tested by the author, and the wave severity of this laminate, δ/λ = 0.04, was lower than the average value obtained by Adams and Bell [6]. This reduced layer wave severity in the 4~~4 laminate is believed to be responsible for the relatively high experimental strength ratio, F_{ex}. To demonstrate the comparison of finite element prediction with mechanical test result, compression strength ratios F_s for the 2~2 layer waviness model are shown in Table 4.8.

Table 4.8 Comparison of predicted first-ply and ultimate compression strengths with mechanical test results for laminates with increasing wave fractions.

Laminate	Total no. of 0° layers	No. of wavy 0° layers	Wave fraction, F_w	Predicted ultimate strength (wave free) (MPa)	Failure stress (Experimental results)			First-ply failure			Ultimate failure		
					Stress (MPa)	Strength ratio, F_{ex} Avg.	Strength reduction (%)	Stress (MPa)	Strength ratio, F_{fp}	Strength reduction (%)	Stress (MPa)	Strength ratio, F_u	Strength reduction (%)
3~3	7	1	0.143	743	653	0.879	12.1	625	0.841	15.9	666	0.896	10.4
2~2	5	1	0.2	726	592	0.816	18.4	617	0.850	15.0	627	0.863	13.7
4~~4*	10	2	0.2	756	659	0.871	12.9	471	0.623	37.7	554	0.733	26.7
2~~2	6	2	0.333	736	480	0.652	34.8	448	0.609	39.1	560	0.761	23.9
2~~~2	7	3	0.429	743	477	0.642	35.8	410	0.552	44.8	470	0.633	36.7
1~~1	4	2	0.5	712	479	0.672	32.8	403	0.566	43.4	459	0.644	35.6
1~~~1	5	3	0.6	726	445	0.613	38.7	382	0.527	47.3	476	0.656	34.4
1~~~~~1	7	5	0.714	743	456	0.613	38.7	325	0.438	56.2	440	0.592	40.8

* Laminate fabricated and tested by the author, $\delta/\lambda = 0.04$

After analyzing the area susceptible to initial damage formation, the region having the highest tensile normal stresses, located above the wavy 0° layer at the central trough of the wave indicated in Figure 4.26, was found to be the most critical under compressive loading. Therefore, the location for initial delamination formation was identified as the first-ply failure at the interface at the top of the wavy 0° layer. This delamination was predicted to initiate at an applied compressive stress of 617 MPa. From previous compression testing of wave-free laminates [4], the ultimate strength (wave-free) of this laminate was 726 MPa. Thus, the predicted strength reduction associated with first-ply failure was 15.04%.

Note that at this point of interface delamination formation, no matrix-dominated failures were predicted to occur in the 90° layers and no fiber failure was predicted to occur in any of the 0° layers. Following the progression of this initial delamination, the input load was increased incrementally until ultimate fiber failure occurred. The delamination, modeled using interface cohesive elements, subsequently propagated, but remained at a length of only one element before the ultimate failure was predicted to occur in the form of compressive fiber failure. Thus, minimal damage progression was predicted in this laminate. The ultimate failure (compressive 0° fiber failure) was predicted to occur at 627 MPa, producing a reduced strength reduction of 13.67%. From previous static compression testing of layer waviness in the 2~2 laminate [4], the average compression strength was 592 MPa, an 18.4% strength reduction in comparison with the wave-free laminate. It is noted, however, that it was not possible to fabricate the ideal single wavy layer in the laminate, and some waviness also was present in the adjacent 0°

layers. Such additional waviness could be responsible to produce the additional strength reduction.

Compression strength ratios presented in Table 4.8 are plotted as a function of wave fraction F_w in Figure 4.39. The experimentally determined strength ratio F_{ex} obtained previously [4] from mechanical testing are compared with predicted strength ratios based on first-ply failure and ultimate failure. Compression strength reductions predicted from first-ply failure analysis ranged from a low of 15.04% (F_{fp}=0.850) to a high of 56.22% (F_{fp}=0.438). Predicted strength reductions based on ultimate failure ranged from a low of 10.39% (F_u=0.896) to a high of 40.77% (F_u=0.592). The experimentally determined strength reductions [4] ranged from a low of 12.1% (F_{ex}=0.879) to a high of 38.7% (F_{ex}=0.613).

In general, both predicted strength ratios as well as the experimental strength ratio indicate increasing strength reductions with increasing wave fraction F_w. However, ultimate strength ratios for the 1~~~1 laminate (F_w=0.6) and 1~~1 (F_w=0.5) were greater than ultimate strength ratio predicted for 2~~~2 laminate having a lower wave fraction F_w of 0.429. Additionally, it is noted that the relationship between strength ratio and wave fraction F_w, is not linear.

Comparing the predicted strength ratios plotted in Figure 4.39 shows significant difference between the predicted first-ply and ultimate failure strengths, especially for laminates with larger wave fractions. In general, the experimental strength ratio F_{ex} is between the first-ply failure strength ratio F_{fp} and the ultimate failure strength ratio F_u.

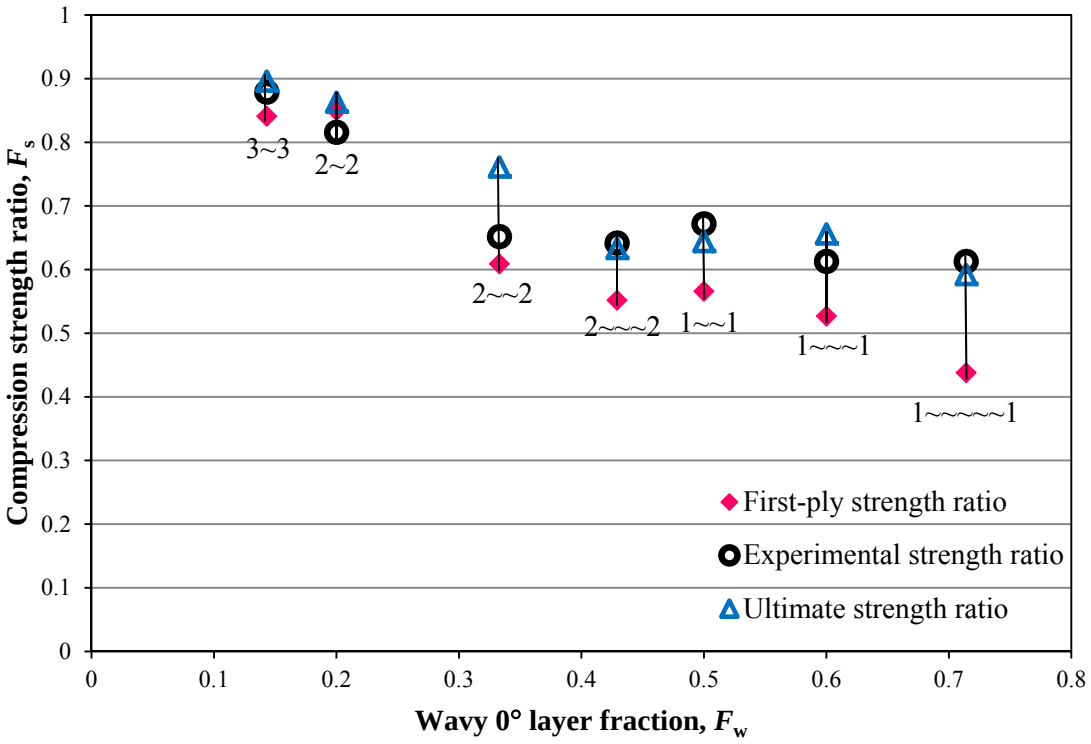

Figure 4.39 Compression strength ratios versus wavy 0° layer fraction.

For the laminates with wave fractions of 0.4 and greater, the ultimate failure strength ratio F_u was found to be in better agreement with the experimental strength ratio F_{ex} than the first-ply failure strength ratio F_{fp}. The difference between the predicted first-ply failure and ultimate failure is shown to increase with increasing wave fraction F_w, an indication of an increasing degree of damage progression.

In virtually all of the compression tests performed, failure was sudden and catastrophic [4, 10]. Further, the post failure determination of failure initiation and damage progression typically was not possible. However, post failure observation determined that the wavy 0° layers commonly fractured at or near an inflection point of the layer wave (midway between the central trough and adjacent crest).

4.5.8 Separated Waves with Midplane Symmetry

Wavy layer laminates with midplane symmetry were used to investigate the interaction of opposing wave formations. Through the use of symmetry boundary conditions, only one-half of the laminate thickness was modeled. Two cases of layer wave symmetry were considered as shown in Figure 4.40 and Figure 4.41. By applying symmetry boundary conditions along the top of the modeled region as shown in Figure 4.40(a), opposing formations of layer waviness were modeled with the central crest and trough spread apart as shown in Figure 4.40(b). By applying symmetry boundary conditions along the bottom of the modeled region as shown in Figure 4.41(a), however, opposing formations of layer waviness were modeled with the central crest and trough brought together as shown in Figure 4.41(b).

Finite element analyses were initially performed to predict the first-ply failure using the Hashin failure criteria. Typically the regions of highest tensile interlaminar

normal stresses were located at the interface between the top wavy 0° layer and the above adjacent 90° layer, near the central trough of the layer waviness. The highest interlaminar shear stresses were generated at the locations where the wavy 0° layer interfaces had the greatest slope. The first-ply failure for nearly all layer wave formations investigated in this section was similar to that of the laminates with waviness at the laminate midplane as discussed previously in Sections 4.5.4 to 4.5.6. The exception was the 1~~~~~1 laminate with bottom 90° layer symmetry formation. In this laminate, matrix failures in a 90° layer occurred prior to interface failure.

Following the prediction of initial failure, a progressive failure analysis was performed as discussed in the previous section. While the input load was increased incrementally, failed elements within the 90° and 0° layers were identified. The material properties of these failed elements were reduced using the prescribed degradation factors. Delaminations were modeled at critical layer interfaces using cohesive elements. In summary, the failure progressions for the separated layer wave formations were similar to those predicted for waviness formations at the laminate midplane as discussed previously in Sections 4.5.4 to 4.5.6.

First-ply and ultimate strength ratios for laminates with and without top horizontal symmetry are shown in Table 4.9. Even though the first-ply strength ratios with top symmetry are lower than those for the corresponding laminates having no symmetry boundary conditions, the ultimate strength ratios are predicted to be similar. All laminates show similar trends of decreasing strength ratios with increasing wave fraction F_w as shown in Figure 4.42.

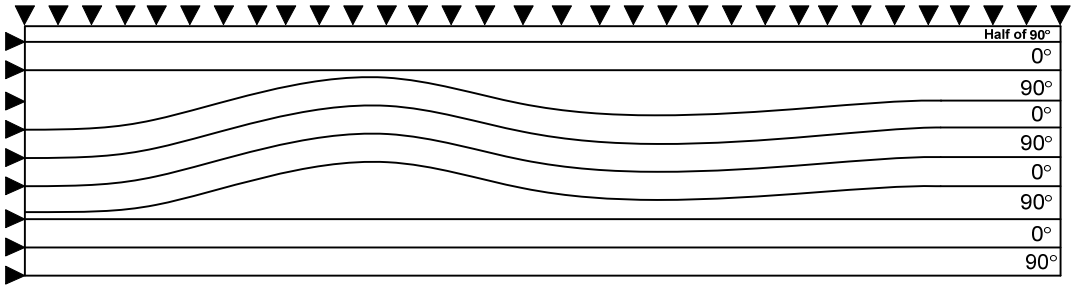

(a) Symmetric boundary condition above the top 90° layer of the laminate.

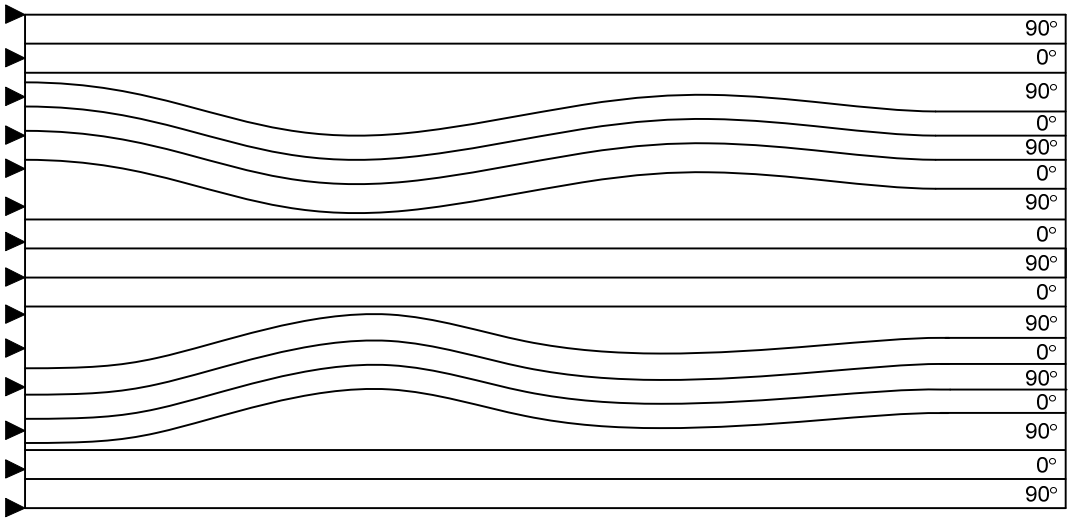

(b) Expanded view of the laminate with top 90° layer symmetry.

Figure 4.40 Opposing formation of layer waviness with symmetry above the top 90° layer.

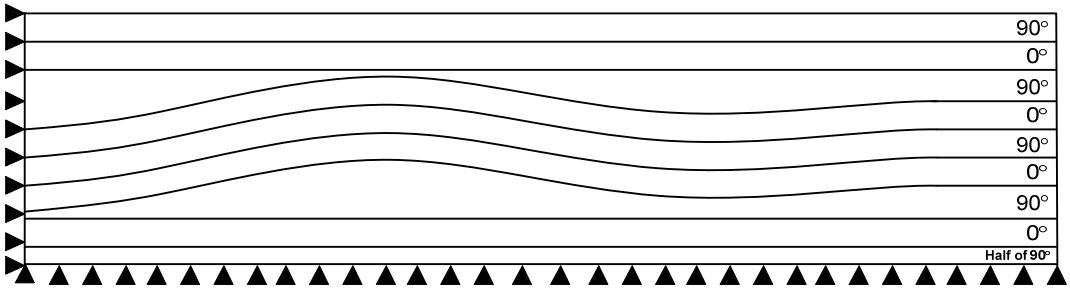

(a) Symmetric boundary condition below the bottom 90° layer of the laminate.

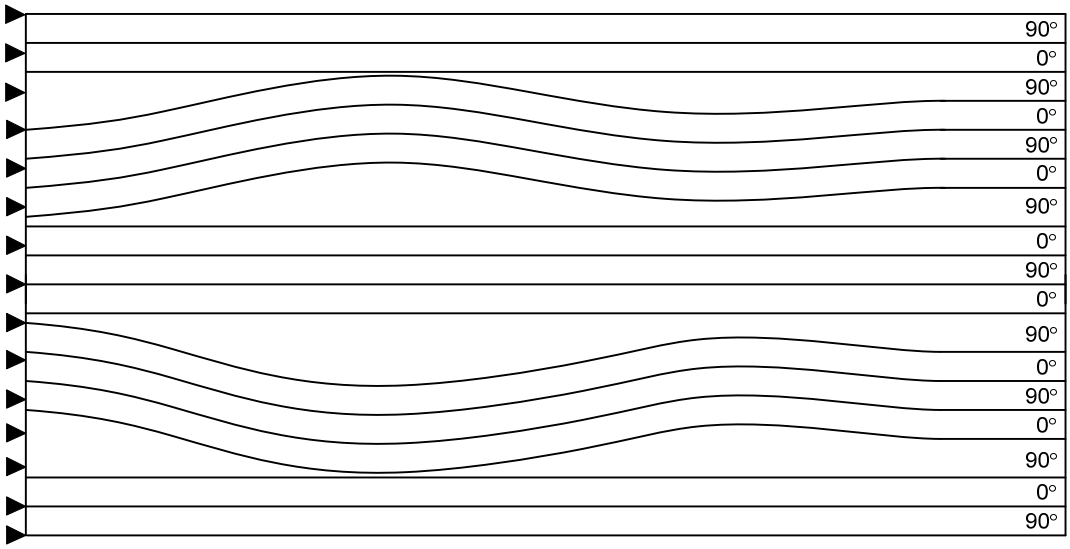

(b) Expanded view of the laminate with bottom 90° layer symmetry.

Figure 4.41 Opposing formation of layer waviness with symmetry below the bottom 90° layer.

Table 4.9 Predicted compression strength ratios for laminates with and without top horizontal symmetry.

Laminate (Top symmetry)	Total no. of 0° layers	No. of wavy 0° layers	Wave fraction, F_w	Predicted ultimate strength (wave free) (MPa)	First-ply failure		Ultimate failure	
					Strength ratio, F_{fp} (without symmetry)	Strength ratio, F_{fp} (with top symmetry)	Strength ratio, F_u (without symmetry)	Strength ratio, F_u (with top symmetry)
4~4	9	1	0.111	753	0.843	0.808	0.926	0.919
3~3	7	1	0.143	743	0.841	0.779	0.896	0.904
2~2	5	1	0.2	726	0.850	0.717	0.863	0.867
3~~3	8	2	0.25	749	0.617	0.554	0.703	0.706
2~~2	6	2	0.333	736	0.609	0.510	0.761	0.695
2~~~2	7	3	0.429	743	0.552	0.452	0.633	0.636
2~~~~2	8	4	0.5	749	0.492	0.430	0.535	0.587
2~~~~~2	9	5	0.555	753	0.459	0.390	0.525	0.516
1~~~~~1	7	5	0.714	743	0.438	0.356	0.592	0.463

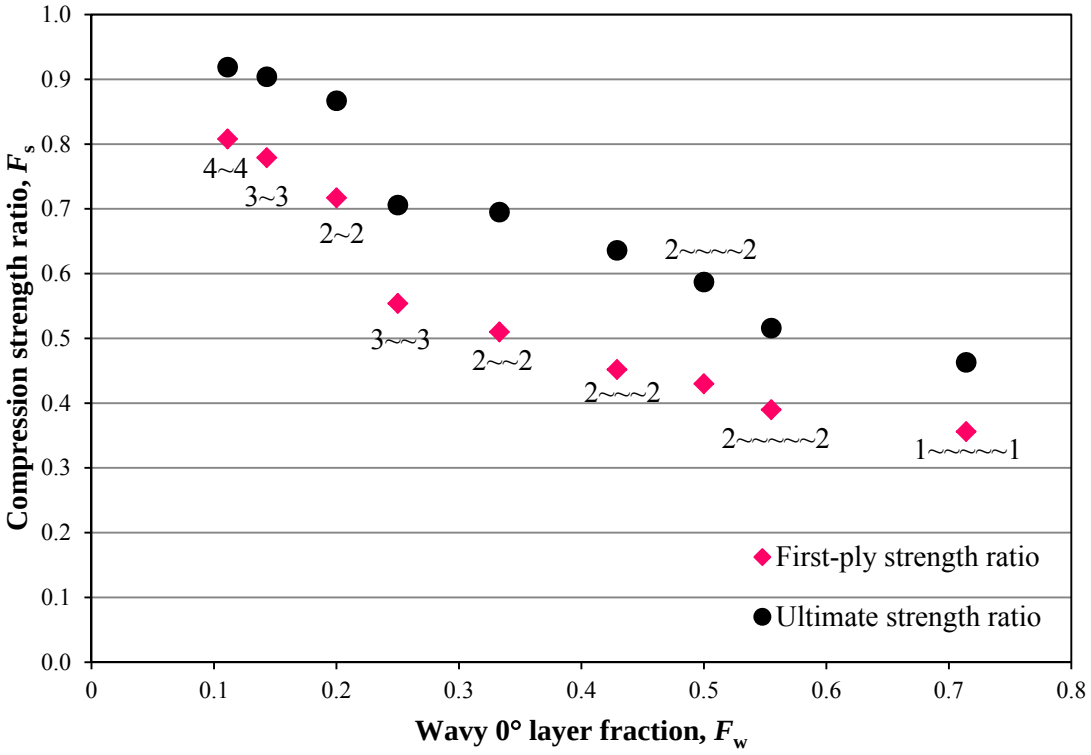

Figure 4.42 Compression strength ratios with top horizontal symmetry versus wavy 0° layer fraction.

First-ply and ultimate strength ratios for laminates with and without bottom horizontal symmetry are shown in Table 4.10. The first-ply and ultimate strength ratios for laminates with bottom symmetry are similar to the corresponding laminates having no symmetry boundary conditions. Once again, the laminates show a general trend of decreasing strength ratios with increasing wave fraction F_w as shown in Figure 4.43. One exception, however, was the compression strength ratio for the 2~~2 laminate (F_w = 0.333), which was greater than strength ratio for the 3~~3 laminate (F_w = 0.25). It was determined that for the 2~~2 laminate, this higher strength was associated with no 90° element failures prior to 0° fiber failure.

Further, two additional laminates with opposing horizontal wavy layers were modeled for comparison with layer wave formations fabricated and tested in this investigation. Note that both the laminate thickness and the total numbers of 0° layers is the same for the two laminates; only the through the thickness positions of the wavy 0° layers are different. The layer waviness model and boundary conditions for the 2~~2 laminate with bottom symmetry is shown in Figure 4.44. For this laminate, a set of two nonwavy 0° layers was placed at the laminate midplane (adjacent to the line of bottom symmetry). The severity of the layer waviness modeled was δ/λ = 0.075. For the first-ply failure analysis, delamination was identified at the interface between the top wavy 0° layer and the upper adjacent 90° layer. In the subsequent progressive failure analysis, this delamination propagated approximately 0.09 mm (1 element length) prior to 0° fiber failure. First-ply and ultimate strength ratios were 0.613 and 0.85, respectively. As discussed in Chapter 3, the experimental strength ratio for this laminate was 0.835.

Table 4.10 Predicted compression strength ratios for laminates with and without bottom horizontal symmetry.

Laminate (Bottom symmetry)	Total no. of 0° layers	No. of wavy 0° layers	Wave fraction, F_w	Predicted ultimate strength (wave free) (MPa)	First-ply failure		Ultimate failure	
					Strength ratio, F_{fp} (without symmetry)	Strength ratio, F_{fp} (with bottom symmetry)	Strength ratio, F_u (without symmetry)	Strength ratio, F_u (with bottom symmetry)
4~4	9	1	0.111	753	0.843	0.849	0.926	0.933
3~3	7	1	0.143	743	0.841	0.883	0.896	0.938
2~2	5	1	0.2	726	0.850	0.852	0.863	0.900
3~~3	8	2	0.25	749	0.617	0.618	0.703	0.725
2~~2	6	2	0.333	736	0.609	0.613	0.761	0.850
2~~~2	7	3	0.429	743	0.552	0.556	0.633	0.701
2~~~~2	8	4	0.5	749	0.492	0.495	0.535	0.644
2~~~~~2	9	5	0.555	753	0.459	0.462	0.525	0.533
1~~~~~1	7	5	0.714	743	0.438	0.472	0.592	0.517

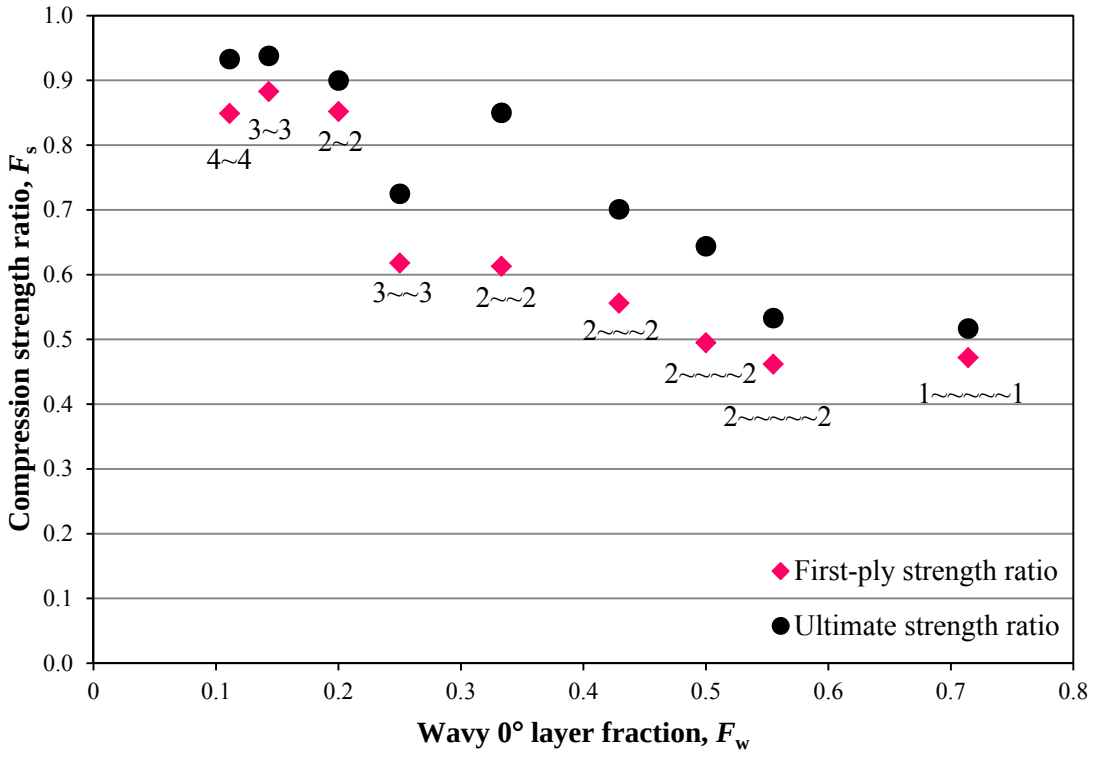

Figure 4.43 Compression strength ratios with bottom horizontal symmetry versus wavy 0° layer fraction.

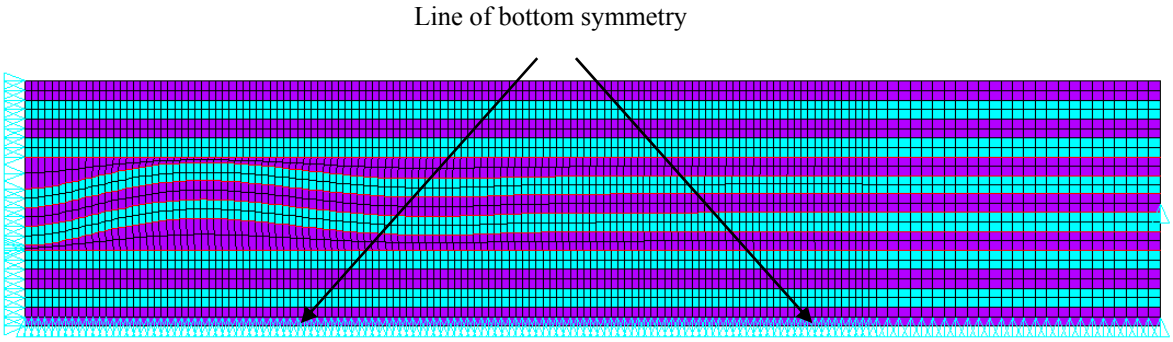

Figure 4.44 Layer waviness model for 2~~2 with bottom symmetry.

Thus, the predicted ultimate compression strength using progressive failure analysis was in agreement with experimental result.

The layer waviness model and boundary conditions for the 3~~1 laminate with bottom symmetry is shown in Figure 4.45. For this laminate, only one nonwavy 0° layer was placed at the laminate midplane (adjacent to the line of bottom symmetry). Thus, greater interaction between the opposing wavy 0° layers was expected to occur. Once again, the severity of the layer waviness was $\delta/\lambda = 0.075$. For the first-ply failure analysis, delamination was identified at the interface between the top wavy 0° layer and the upper adjacent 90° layer. In the subsequent progressive failure analysis, this delamination propagated approximately 0.18 mm (2 element lengths) prior to 0° fiber failure. First-ply and ultimate strength ratios were 0.615 and 0.80, respectively. As discussed in Chapter 3, the experimental strength ratio for this laminate, averaged from four samples, was 0.906. Thus, the predicted ultimate strength ratio was significantly lower than the experimental results.

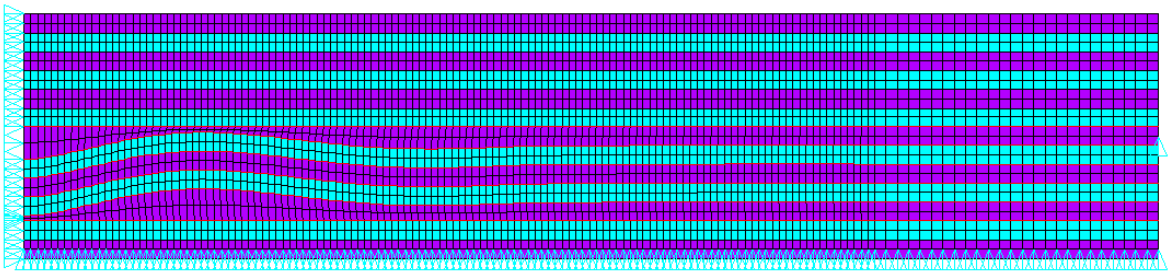

(a) Layer wave severity δ/λ = 0.075.

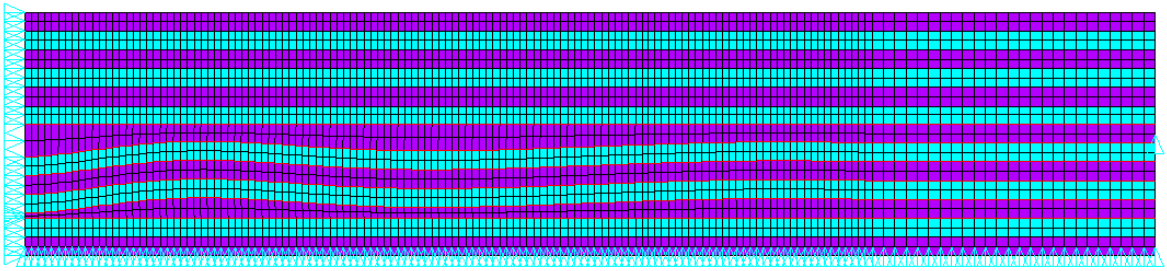

(b) Layer waviness severity δ/λ = 0.043.

Figure 4.45 Layer waviness severities modeled in 3~~1 laminate with bottom symmetry.

It is noted, however, that the wave severity of the tested specimens (δ/λ = 0.043) was significantly lower than modeled the modeled severity (δ/λ = 0.075). To provide a comparison of the ultimate strength ratios for laminates having the identical wave severity (δ/λ = 0.075), the 2~~2 and 3~~1 laminates with bottom symmetry may be compared. The ultimate strength ratios of 3~~1 laminate with bottom symmetry was 0.80 as compared to 0.85 for the 2~~2 laminate. Hence, the laminate with the reduced number of nonwavy 0° layers separating the regions of layer waviness appear to have a greater reduction in compression strength.

In an effort to further understand the effects of layer wave severity on compression strength, additional finite element modeling was performed for the 3~~1 laminate with bottom symmetry with a reduced wave severity of δ/λ = 0.043 as shown in Figure 4.45(b). With this reduced wave severity, the predicted ultimate strength ratio increased to 0.90, in agreement with the average experimental strength ratio of 0.906.

4.5.9 Separated Waves with the Same Horizontal Orientation

In this section, the use of cohesive elements and progressive failure analysis was employed for predicting compression strength reductions due to layer waviness in thicker composite laminates. As mentioned previously, cohesive elements allow for an interface within a wavy finite element model to experience delamination failure based on stress-based failure criteria, followed by interface crack growth based on fracture mechanics criteria. The use of cohesive elements and progressive failure analysis for investigating simple, idealized formations layer waviness has been demonstrated, as discussed in previous sections. However, in reality, layer waviness is commonly observed in thick-section composite laminates as a group of wavy layers within the laminates. Thus, to

further understand the compression strength reductions due to layer waviness in actual composite structures, more realistic wave formations were considered.

Thick laminates fabricated and tested by Adams [10] containing multiple sets of separated wavy 0° layers within the laminate with same horizontal orientation were modeled in this section. Laminates fabricated by Adams [10] were given three different classifications based on the thickness and the multiple sets of wave formations within the laminate as presented in Table 4.11 and Table 4.12. Thinner laminates containing one and two sets of single, double, and triple wavy 0° layers within the laminate were included into the "THIN" classification. Thicker laminates containing three sets of double and triple wavy 0° layers were grouped into the "THICK1" classification. Finally the thickest laminates with two and three sets of single and triple wavy 0° layers were grouped into the "THICK2" classification. Results [10] for compression strength reduction for all specimens tested are presented in Figure 4.46 and Figure 4.47.

Results shown in Figure 4.46 and Figure 4.47 show the general tendencies of decreasing compression strength ratio with increasing wave fraction F_w. However, significant variations in this decreasing trend are observed. As an example, the average experimental compression strength ratio F_{ex} for laminate 1~~~5~~~1 (F_w = 0.462) was determined as 0.676, which was slightly greater than F_{ex} for laminate 2~~4~~2 (F_w = 0.333) as 0.621. Another example is the three different wave formations as part of the THIN laminates, resulting in the same wave fraction (0.143) and laminate thickness (and 7.37 mm). However, one of the laminates (6~~6) produced a lower compression strength ratio than the other two laminates (2~8~2 and 3~6~3).

Table 4.11 Results from THIN laminates [10].

Shorthand designation	Type	Wave fraction, F_w	Laminate thickness, T (mm)	Predicted ultimate strength (wave free) (MPa)	Experimental failure			
					Stress (MPa)	Stress Avg. (MPa)	Strength ratio, F_{ex} Avg.	Strength reduction (%)
6~~6	(Double wave-one set)	0.143	7.37	766	566 550	558	0.729	27.1
2~8~2	(Single wave-two set)	0.143	7.37	766	600 653 653 715	655	0.856	14.4
3~6~3	(Single wave-two set)	0.143	7.37	766	678 660 651 754	686	0.896	10.4
2~4~2	(Single wave-two set)	0.200	5.33	756	610 609	610	0.806	19.4
2~~4~~2	(Double wave-two set)	0.333	6.35	762	419 517 484	473	0.621	37.9
2~~~4~~~2	(Triple wave-two set)	0.429	7.37	766	486 528 474 409	474	0.619	38.1
1~~~5~~~1	(Triple wave-two set)	0.462	6.86	764	514 525 511	517	0.676	32.4
1~~2~~1	(Double wave-two set)	0.500	4.32	749	427 473 488 460	462	0.618	38.3
1~~~2~~~1	(Triple wave-two set)	0.600	5.33	756	452 421 370 371	403	0.533	46.7

Table 4.12 Results from THICK1 and THICK2 laminates [10].

Shorthand designation	Type	Wave fraction, F_w	Laminate thickness, T (mm)	Predicted ultimate strength (wave free) (MPa)	Experimental failure			
					Stress (MPa)	Stress Avg. (MPa)	Strength ratio, F_{ex} Avg.	Strength reduction (%)
1~~~5~~~5~~~1	TH3 (Triple wave-three set)	0.429	10.9	774	442 483 442 426 442	447	0.578	42.2
1~~2~~2~~1	TH3 (Double wave-three set)	0.500	6.35	762	523 519 454 464 547	501	0.658	34.2
1~~~2~~~2~~~1	TH3 (Triple wave-three set)	0.600	7.87	767	379 408 351 381 358	375	0.489	51.1
3~6~6~3	THC23 (Single wave-three set)	0.143	10.9	774	600 611 737 688	659	0.852	14.8
5~4~4~5	THC23 (Single wave-three set)	0.143	10.9	774	512 590 493 565	540	0.698	30.2
3~~~9~~~3	THC23 (Triple wave-two set)	0.286	10.9	774	476 457 441 404	445	0.575	42.5

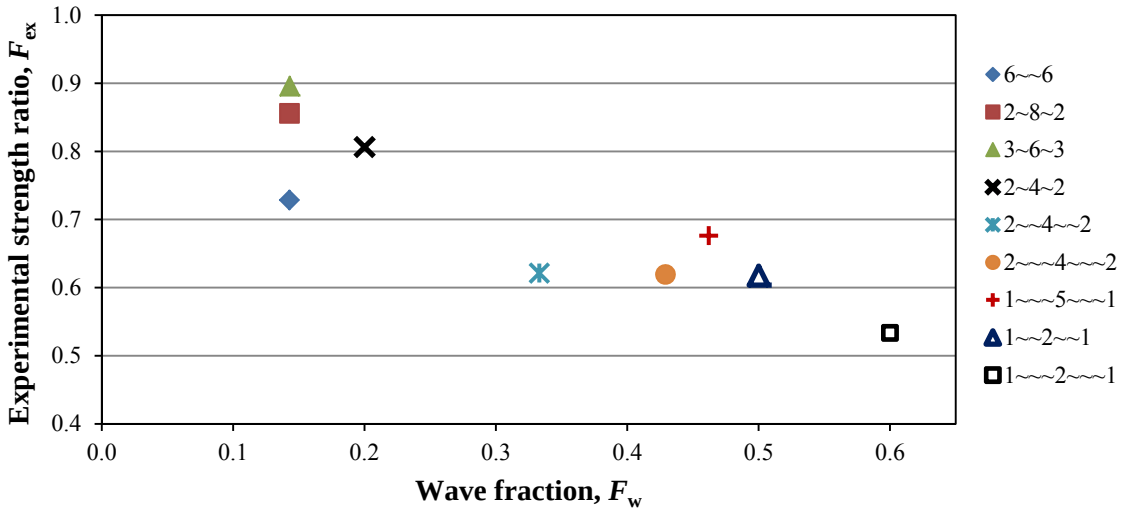

Figure 4.46 Experimental strength ratios versus wavy 0° layer fraction for THIN laminates.

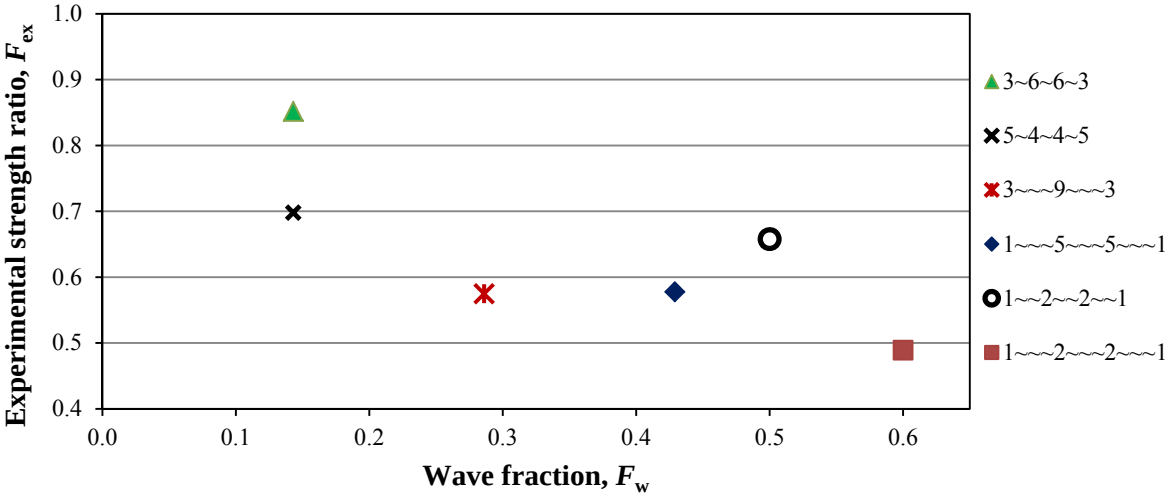

Figure 4.47 Experimental strength ratios versus wavy 0° layer fraction for THICK1 and THICK2 laminates.

As a third example, laminates containing two sets of single waves and a greater number of nonwavy layers at the midplane of the laminate (2~8~2 and 3~6~3) exhibit greater compression strength ratios compared to the 6~~6 laminate containing the same wave fraction and laminate thickness. Thus, strength reductions in cross-ply laminates due to layer waviness appear to be dependent on the relevant location of wavy and nonwavy layers in addition to simply the wave fraction.

To further explore the role of layer waviness on compression strength reductions, other comparisons of experimental results are of interest. Test results show that the 2~4~2 laminate produced a higher compression strength ratio (F_{ex} = 0.806) than both the 2~~4~~2 laminate (F_{ex} = 0.621) and the 2~~~4~~~2 laminate (F_{ex} = 0.619) laminate. This finding suggests that the presence of multiple nested layers of waviness at specific locations produce greater strength reductions with increasing wave fraction F_w.

Also of interest is a comparison of laminates having the same wave fraction and laminate thickness, but different through-the-thickness placements of layer waviness. For example, laminate 3~6~6~3 produced a higher strength ratio (F_{ex} = 0.852) than laminate 5~4~4~5 (F_{ex} = 0.698). These results suggest that a greater number of non-wavy 0° layers in the central region of the laminate produce higher compression strength ratios. Thus, the presence of layer waviness in the central portions of the laminate appears to produce a greater reduction in compression strength ratio.

A comparison of compression strength ratios for the 5~4~4~5 laminate (F_{ex} = 0.698) and the 3~~~9~~~3 laminate (F_{ex} = 0.575) is of some interest, as both laminates have the same overall laminate thickness. Result indicates that decreasing and

distributing the waviness throughout the laminate thickness results in a higher compression strength ratio.

In virtually all of the compression tests of laminates with layer waviness performed previously by Adams and Bell [4] and Adams [10], specimen failure was sudden and catastrophic, producing post failure specimen conditions as shown in Figure 4.48 and Figure 4.49. The extensive level of damage and post-failure crushing of the failed regions of the specimens made post failure determination of failure initiation impossible. In a few specific tests, however, failure initiation was detected audibly such that loading could be immediately stopped after failure initiation. In these cases, stopping the loading prior to ultimate catastrophic failure made the determination of failure initiation possible. As shown in Figure 4.49, initial failure in the 1~~~2~~~1 laminate appears to have involved fracture of the wavy 0° layers at or near an inflection point of the layer wave. In laminate 1~~~2~~~2~~~1, delaminations were produced at the outermost wavy 0° layer interfaces and fracture of the wavy 0° layers occurred near an inflection point of the wavy layers.

To further investigate the effects of variable groups of wavy layers, finite element models similar to that shown in Figure 4.50 were analyzed. All of the thick laminates fabricated and tested by Adams [10] containing multiple sets of separated wavy 0° layers within the laminate were analyzed. Initially, a stress analysis was performed for each laminate as described previously in section 4.5.3. These analyses were used to identify the areas susceptible to damage formation. To predict the location of first-ply failure, the Hashin failure criteria [9] was used.

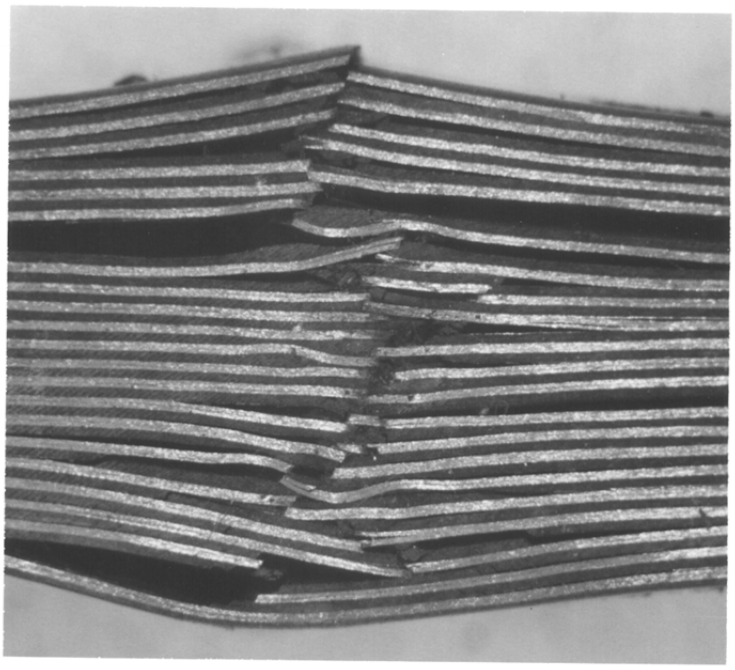

5~4~4~5

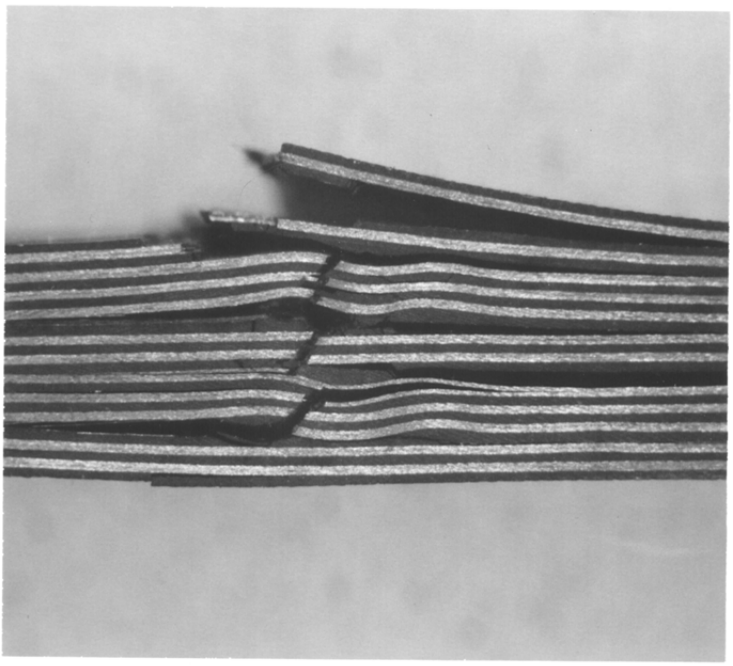

2~~~2~~~2

Figure 4.48 Specimens prepared and tested by Adams [10].

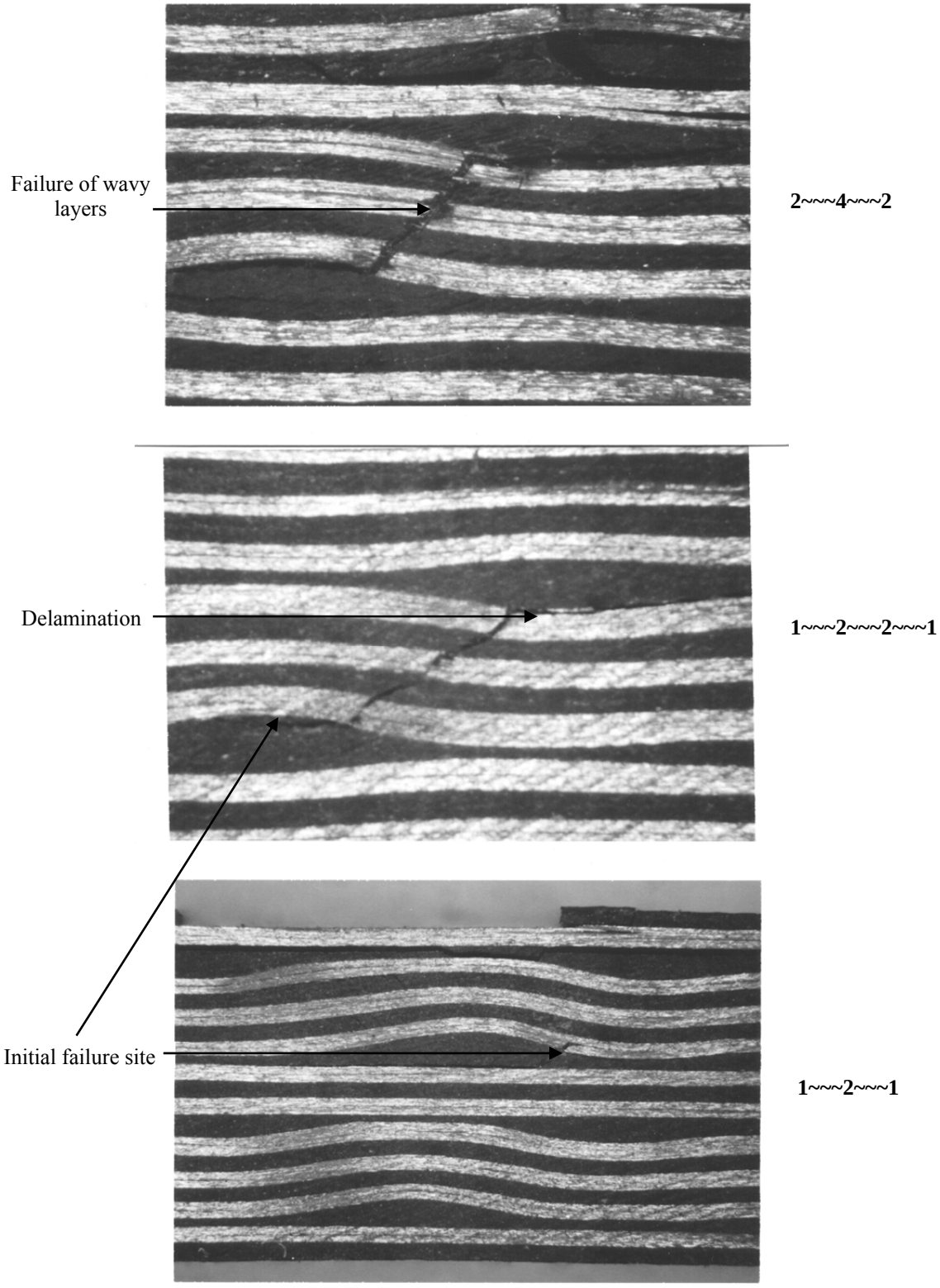

Figure 4.49 Specimens prepared and tested by Adams [10].

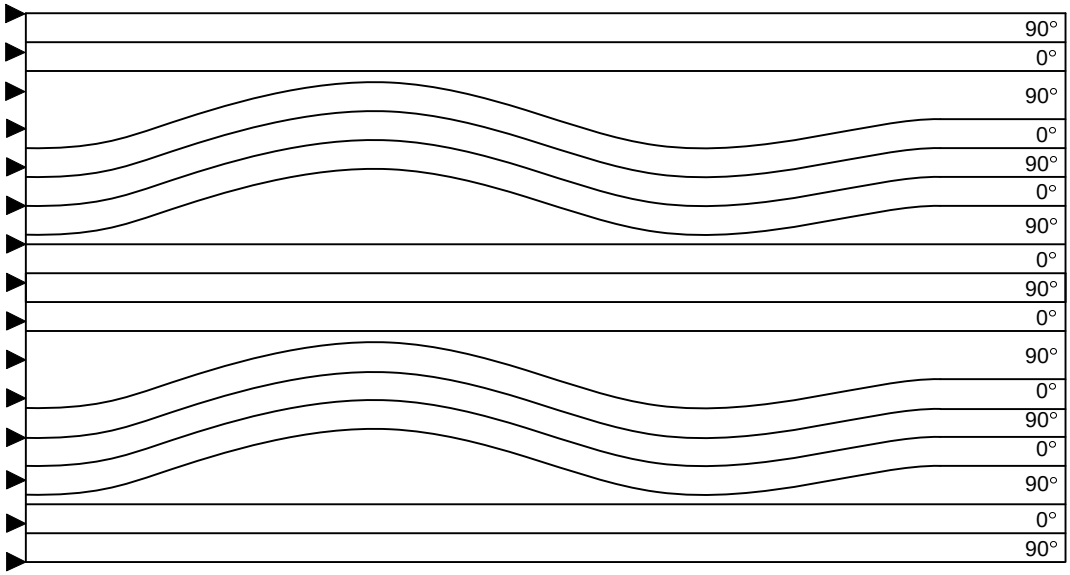

Figure 4.50 Finite element model used for 1~~2~~1 laminate.

Cohesive elements were used to investigate delamination propagation at layer interfaces determined to be candidate locations for damage formation. Next, a progressive damage analysis was performed using an ANSYS user subroutine as described previously.

As a representative model for the thick composite laminate, the 1~~~2~~~1 layer waviness model is employed to explain the failure progression observed. First, the critical areas of initial failure were analyzed. Contour plots of the nondimensionalized stresses for the 1~~~2~~~1 laminate are shown in Figure 4.51 to Figure 4.53. Maximum compressive stress values in the loading direction, shown in Figure 4.51, were located along the central plane of the layer waviness formation, either in one of the wavy 0° layers or an adjacent nonwavy 0° layer.

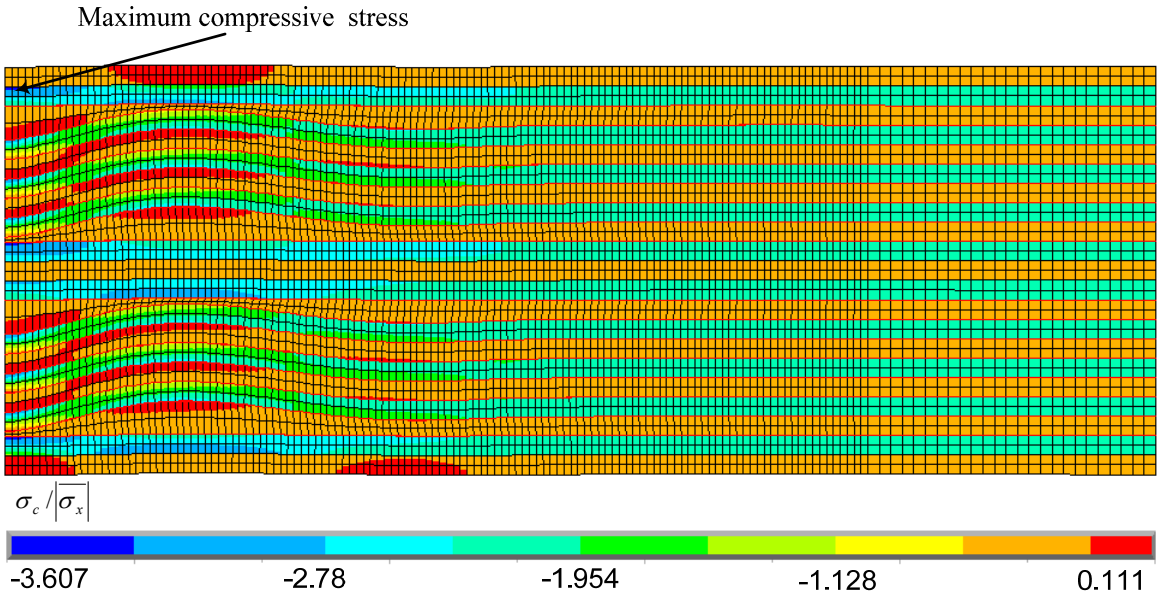

Figure 4.51 Normalized σ_c contour plot for 1~~~2~~~1 laminates.

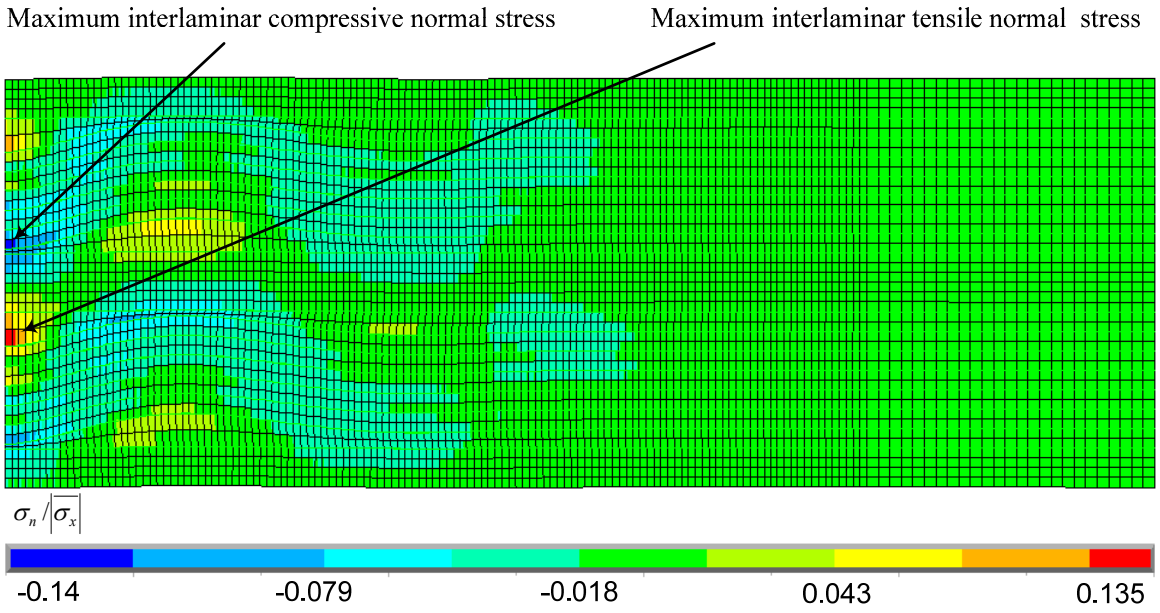

Figure 4.52 Normalized σ_n contour plot for 1~~~2~~~1 laminate.

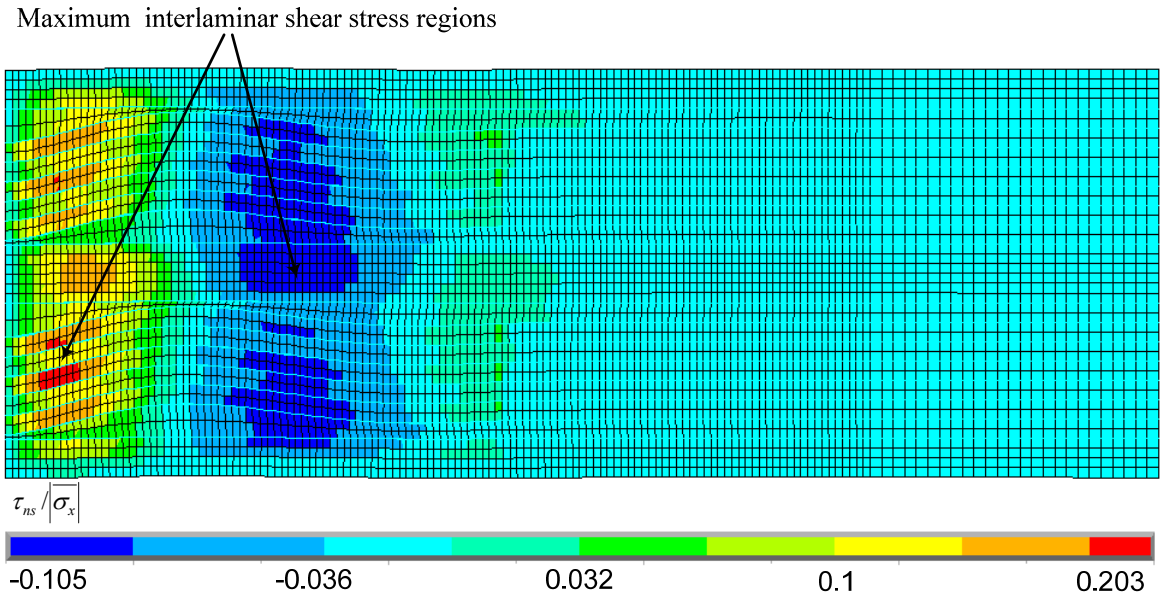

Figure 4.53 Normalized τ_{ns} contour plot for 1~~~2~~~1 laminate.

For the maximum interlaminar normal stresses shown in Figure 4.52, the peak compressive and tensile normal stresses were identified near the central plane of the layer waviness. The highest tensile stress, located within the lower set of wavy layers, occurred near the central trough of the layer waviness, at the interface between the uppermost wavy 0° layer and the top adjacent 90° layer. The location of highest interlaminar normal compressive stress was identified within the upper set of wavy layers, and in the center of the 90° layer below the bottommost wavy 0° layer. The highest interlaminar shear stresses occurred within the wavy layers where the slope of the wavy 0° layers was maximum as shown in Figure 4.53. This location of maximum slope of the wavy layers was the inflection point of the wavy 0° layers, midway between the central trough and adjacent crest of the wave. Thus, the two possible locations of initial failure of this laminate were these two regions of high interlaminar stresses.

After analyzing the areas susceptible to initial damage formation, the Hashin failure criterion was used to determine the finite elements within these regions in which initial failure is predicted. In this 1~~~2~~~1 layer waviness model, elements in the 90° layer above the nonwavy 0° layers failed initially as shown in Figure 4.54. The material properties of these failed elements (pink colored elements) were then reduced using the prescribed degradation factors, and the loading was increased incrementally. Next, an initial delamination was identified on the line of symmetry, located within the lower set of wavy layers at the interface between wavy 0° layers and above adjacent 90° layers. Location of initial delamination corresponds with the location of the highest interlaminar normal tensile stress predicted as shown in Figure 4.52.

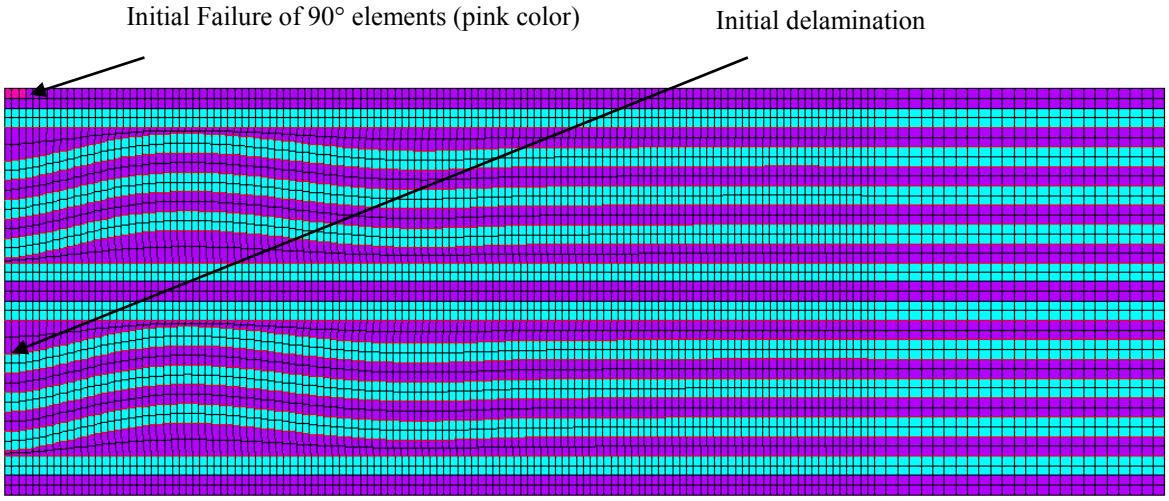

Figure 4.54 Initial failure of 90° elements in 1~~~2~~~1 layer waviness model.

After the initial failures were identified, the progressive failure approach was used to predict the sequence of damage formation leading to ultimate failure. The maximum stress failure criterion was used to determine 0° layer fiber failure. The initial fiber failure, identified as green colored elements is shown in Figure 4.55(a) was located below the adjacent failed 90° elements. Figure 4.55(b) shows the locations of additionally failed 90° and 0° elements prior to ultimate failure. The predicted stress versus strain response of the 1~~~2~~~1 layer waviness model is shown in Figure 4.56. The stress levels corresponding to the initial matrix failure, the onset of delamination, and the fiber failure for this laminate are shown on the plot.

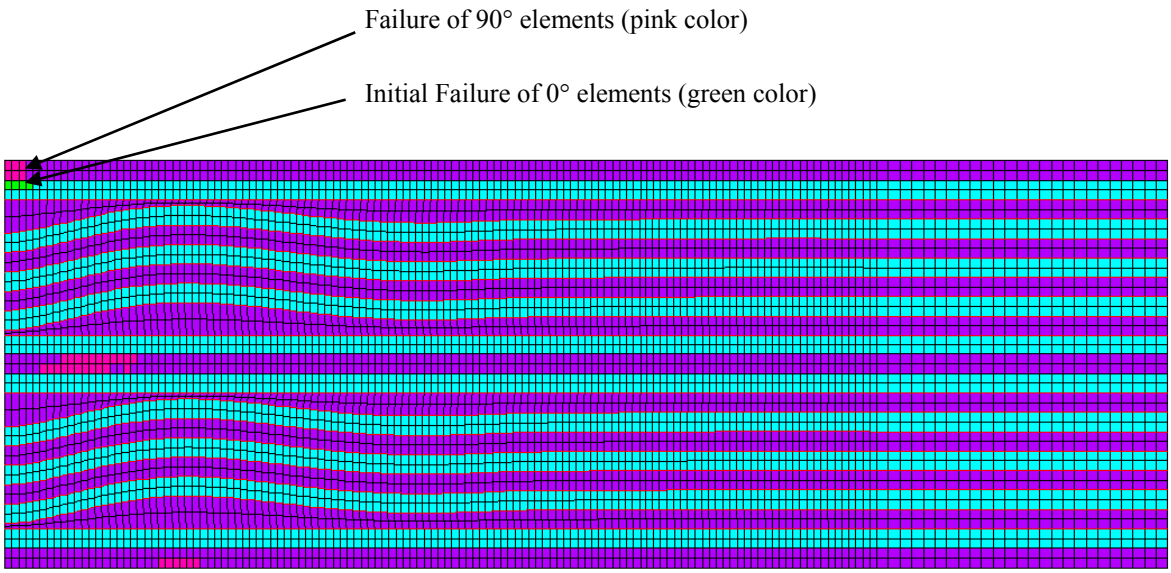

(a) Initial failure of 0° elements of 1~~~2~~~1 layer waviness model.

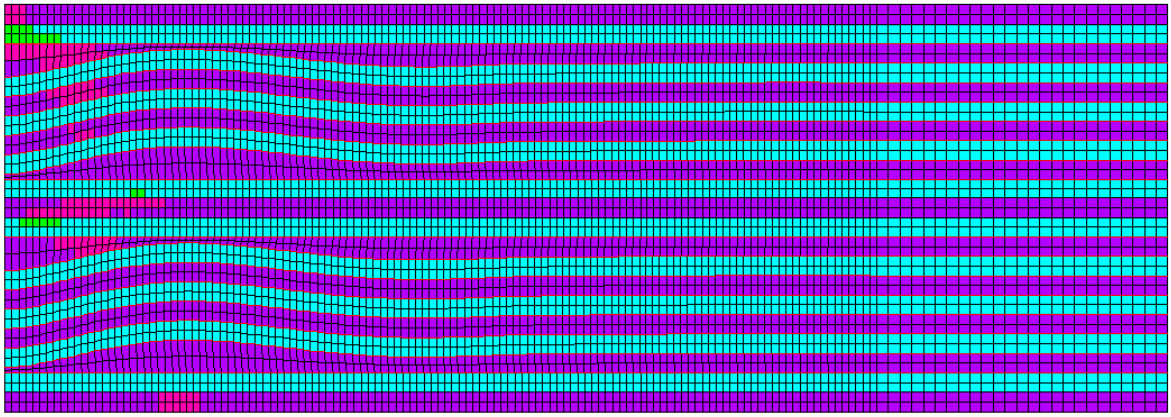

(b) Progressive failure of 0° and 90° elements of 1~~~2~~~1 layer waviness model.

Figure 4.55 Progressive failure of the 0° layers leading to ultimate failure, 1~~~2~~~1 layer waviness model.

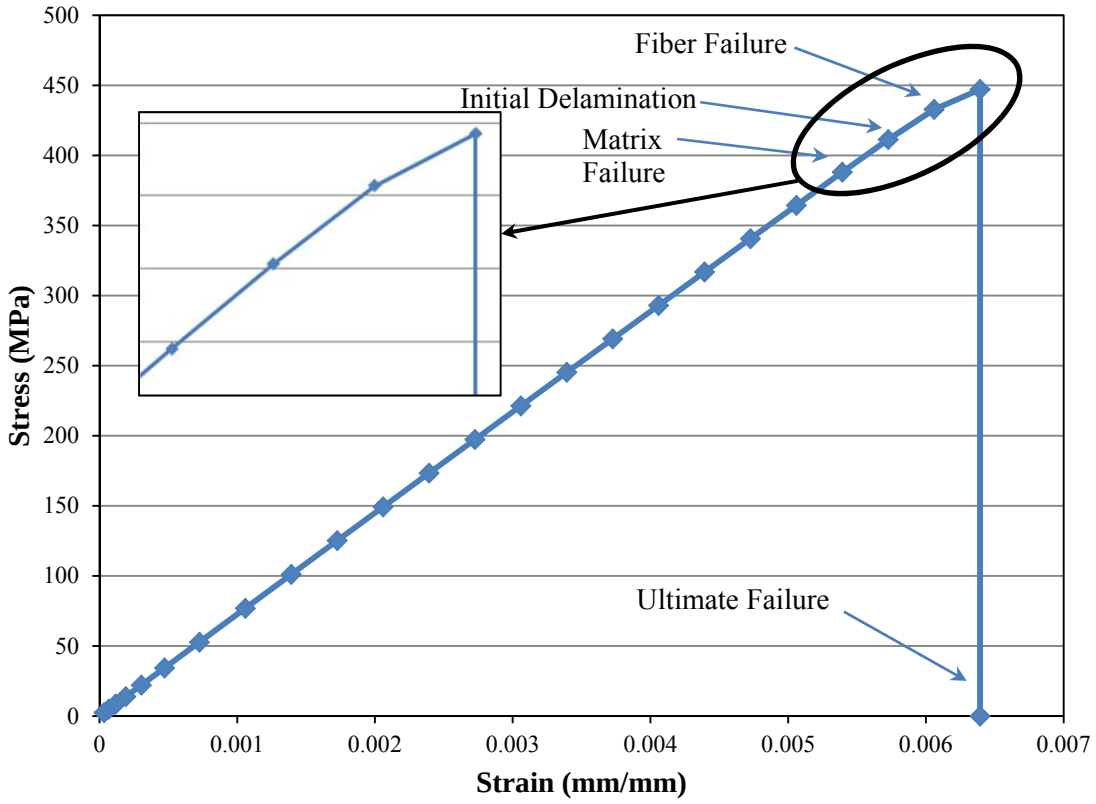

Figure 4.56 Stress-strain relationship of 1~~~2~~~1 layer waviness model.

The predicted compression stress corresponding to both initial failure and ultimate failure for all of the laminates described above are presented in Table 4.11 and Table 4.12. Interface failure was identified as the initial failure for all layer wave formations investigated with the exception of the 1~~2~~1, 1~~~2~~~1, 1~~2~~2~~1, and 1~~~2~~~2~~~1 laminates. Matrix failures in a 90° layer occurred prior to interface failure in these laminates. Finite element predictions for both the initial failure stress and ultimate failure stress are compared with the compression strengths obtained from mechanical testing in Table 4.13.

Table 4.13 Comparison of predicted and measured compression strengths for laminates tested by Adams [10].

Shorthand designation	Wave fraction, F_w	Laminate thickness, T (mm)	Predicted ultimate strength (wave free) (MPa)	Experimental failure			Initial failure			Ultimate failure		
				Stress (MPa) Avg.	Strength ratio, F_{ex} Avg.	Strength reduction (%)	Stress (MPa)	Strength ratio, F_{fp}	Strength reduction (%)	Stress (MPa)	Strength ratio, F_u	Strength reduction (%)
3~3	0.143	3.81	743	653	0.879	12.1	625	0.841	15.9	666	0.896	10.4
3~6~3	0.143	7.37	766	686	0.896	10.4	637	0.832	16.9	697	0.909	9.03
6~~6	0.143	7.37	766	558	0.729	27.1	477	0.623	37.7	564	0.737	26.3
2~8~2	0.143	7.37	766	655	0.856	14.4	597	0.779	22.1	676	0.883	11.7
3~6~6~3	0.143	10.9	774	659	0.852	14.8	603	0.780	22.0	704	0.910	9.02
5~4~4~5	0.143	10.9	774	540	0.698	30.2	567	0.732	26.8	692	0.895	10.5
2~2	0.2	2.79	726	592	0.816	18.4	617	0.850	15.0	627	0.863	13.7
2~4~2	0.2	5.33	756	610	0.806	19.4	626	0.827	17.3	665	0.879	12.1
4~~4	0.2	5.33	756	659	0.871	12.9	471	0.623	37.7	554	0.733	26.7
3~~~9~~~3	0.286	10.9	774	445	0.575	42.5	378	0.488	51.2	520	0.673	32.7
2~~2	0.333	3.30	736	480	0.652	34.8	448	0.609	39.1	560	0.761	23.9
2~~4~~2	0.333	6.35	762	473	0.621	37.9	468	0.614	38.6	544	0.714	28.6
1~~~5~~~1	0.462	6.86	764	517	0.676	32.4	466	0.610	39.0	523	0.684	31.6
2~~~2	0.429	3.81	743	477	0.642	35.8	410	0.552	44.8	470	0.633	36.7
2~~~4~~~2	0.429	7.37	766	474.	0.619	38.1	401	0.524	47.6	484	0.632	36.8
1~~~5~~~5~~~1	0.429	10.9	774	447	0.578	42.2	366	0.473	52.7	446	0.576	42.4
1~~1	0.5	2.29	712	479	0.672	32.8	403	0.566	43.4	459	0.644	35.6
1~~2~~1	0.5	4.32	749	462	0.618	38.3	445	0.594	40.6	479	0.639	36.0
1~~2~~2~~1	0.5	6.35	762	501	0.658	34.2	460	0.604	39.6	533	0.699	30.0
1~~~1	0.6	2.79	726	445	0.613	38.7	382	0.527	47.3	476	0.656	34.4
1~~~2~~~1	0.6	5.33	756	403	0.533	46.7	388	0.513	48.7	433	0.572	42.8
1~~~2~~~2~~~1	0.6	7.87	767	375	0.489	51.1	395	0.514	48.6	440	0.574	42.6

The ultimate strength ratios F_u predicted from finite element analysis are in good general agreement with the experimentally determined strength ratios F_{ex}. Comparisons of measured and predicted strength ratios for selected sets of laminates are shown in Figure 4.57 through Figure 4.59. In each of these plots, the relationship of the measured and predicted strength ratios (F_{ex}, F_{fp}, and F_u) are plotted versus total laminate thickness for different sets of laminates having constant wave fractions, F_w.

For most of the laminates investigated, the measured compression strength ratios were between the predicted initial and ultimate strength ratios. In sets of laminates having constant wave fractions, however, differences in compression strength ratios were small.

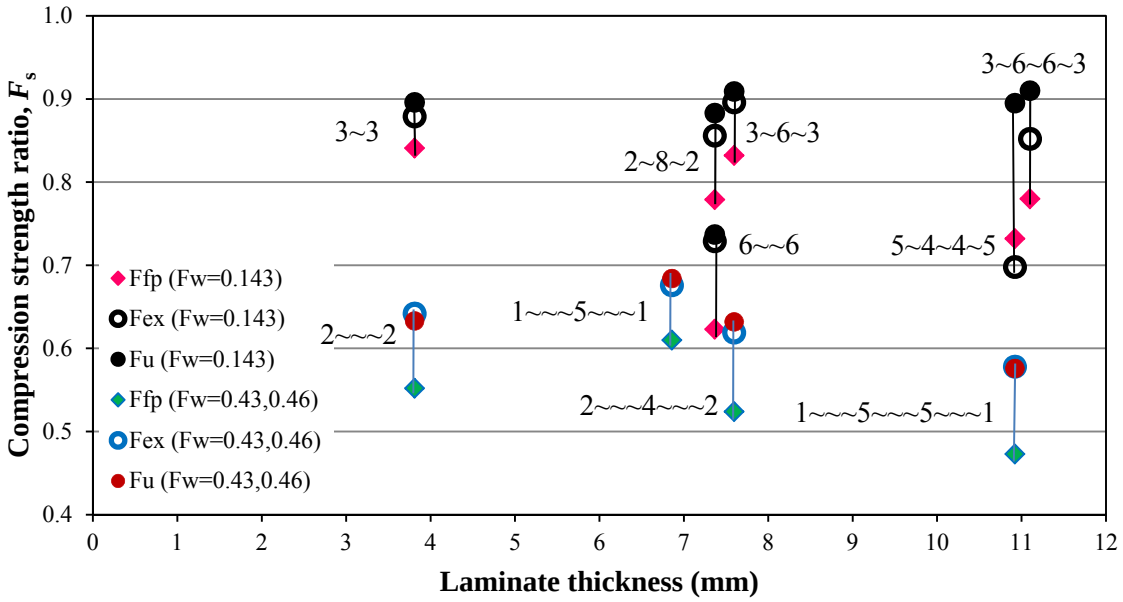

Figure 4.57 Compression strength ratios versus laminate thicknesses for wave fraction of 0.143, 0.43 and 0.46.

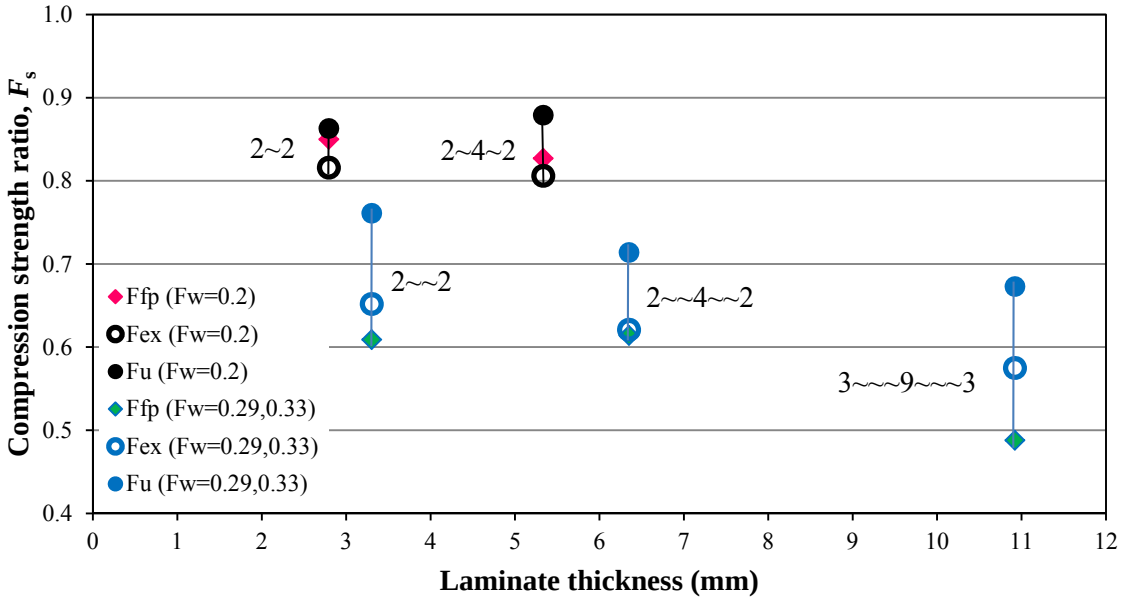

Figure 4.58 Compression strength ratios versus laminate thicknesses for wave fraction of 0.2, 0.29 and 0.33.

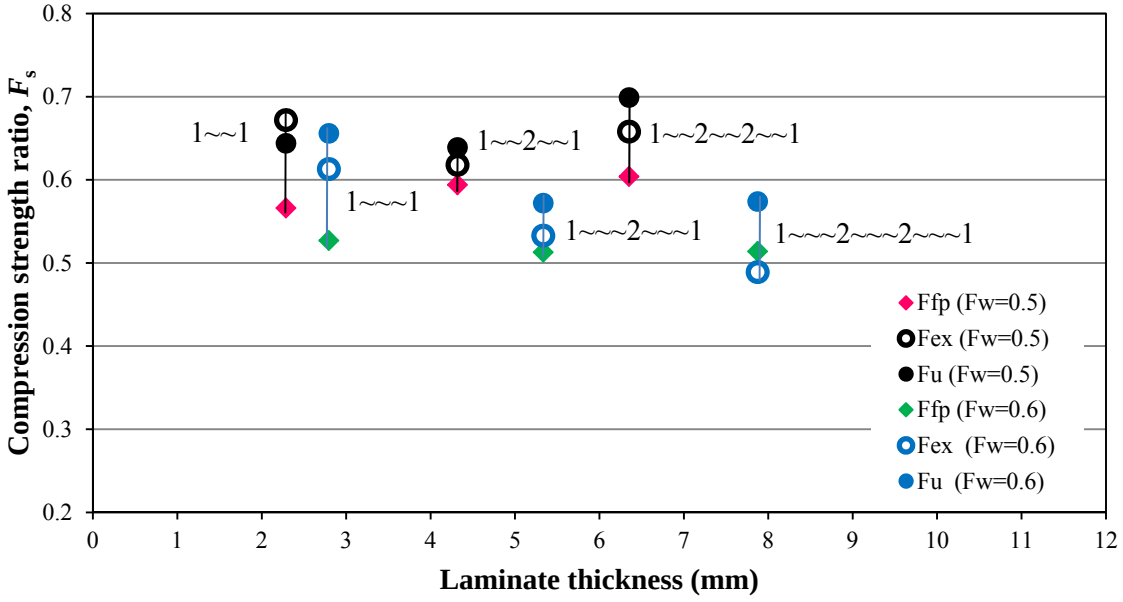

Figure 4.59 Compression strength ratios versus laminate thicknesses for wave fraction of 0.5 and 0.6.

From Figure 4.57, the 6~~6 laminate exhibited a lower compression strength ratio than the 2~8~2 and 3~6~3 laminates even though the wave fraction and the thickness of these three laminate were identical. Further, the 5~4~4~5 laminate exhibited a lower strength ratio than the 3~6~6~3 laminate. As discussed above, if the nonwavy 0° layers at the midplane of the laminates containing the same wave fraction and laminate thickness are increased, a higher compression strength ratio is typically produced.

In a majority of the laminates investigated, the initial, experimental and ultimate strength ratios for different laminates containing identical wavy 0° layer fractions F_w can be different based on the laminate lay-up and location of the wavy layers. Consequently, an accurate prediction of the compression strength ratio based solely on the wavy 0° layer fraction is not possible. In addition to the wave fraction, the compression strength ratio is also dependent on the wave locations and thickness of the laminate.

CHAPTER 5

CONCLUSIONS AND RECOMMENDATIONS

In this research, the effects of layer waviness on the static compression strength of the IM7/8551-7A carbon/epoxy composite laminates were investigated. Out-of-plane layer waviness, a manufacturing-induced imperfection in multidirectional composite laminates, has been shown to produce significant decreases in compression strength. To date, failure predictions based on initial "first-ply" failure analyses as well as compression strength estimates based on the ply fraction containing waviness have shown limited agreement for compression-loaded cross-ply laminates with idealized formations of layer waviness. Neither approach appears to be practicable for a broad range of layer waviness formations. Thus, both mechanical testing and finite element analysis were performed in this study. A finite element modeling method employing progressive failure analysis was developed for predicting compressive strength reductions and validated using compression test results from composite laminates containing layer waviness.

5.1 Conclusions

There were two main topics of this investigation: mechanical testing and finite element analysis. Conclusions related to each of these topic areas are summarized in the following sections.

5.1.1 Mechanical Testing

1. The Mode I and Mode II critical strain energy release rates, the primary material property employed to predict delamination growth, were experimentally determined for IM7/8551-7A carbon/epoxy laminates. The average values of the energy release rates for Mode I and Mode II were subsequently used as inputs for the cohesive elements used in finite element analysis.
2. A single-step fabrication procedure was employed to fabricate both single and multiple-nested wavy 0° layers into otherwise wave-free cross-ply composite laminates. The fabrication of the composite laminates with a variety of layer wave formations was successful even though the layer wave severities, δ/λ for some specimens were lower than the target value of 0.075.
3. The NASA short block compression test configuration was employed to perform static compression testing of specimens with layer waviness and determine compression strength reductions associated with the different layer waviness formations. For the 4~~4 laminate, layer waviness of severity δ/λ = 0.043 in the central two 0° layers produced a 12% compression strength reduction for the laminate having the wave severity of δ/λ = 0.043. Two other laminates tested had the same laminate thickness and the same wave fraction, but different separation distances between layer wave formations within the laminate: a 2~~2 laminate with bottom symmetry and a 3~~1 laminate with bottom symmetry. The difference in through-the-thickness wave separation distance did not produce a significant difference in the measured compression strength reduction.

5.1.2 Finite Element Analysis

As discussed in Chapter 4, a finite element modeling approach using a progressive failure analysis has been used to investigate layer waviness effects on the static compression strength of composite laminates. A summary and conclusions from the finite element analyses for this research are summarized in this section.

1. Two-dimensional plane strain finite element analyses of composite laminates with waviness were performed to predict compression strength reductions from a variety of layer waviness formation. This investigation extended previous research by employing a progressive failure analysis. These analyses featured cohesive elements to model the formation and growth of interlaminar delaminations under general mixed-mode loading. Additionally, lamina failure progressions in the 0° and 90° layers were modeled by applying the Hashin failure criteria to an incremental analysis, degrading failed elements at each load step.
2. In order to validate the interlaminar delamination model in the vicinity of layer waviness using cohesive elements, a series of simplified analyses were performed and the results compared to experimental results. Input properties required for the cohesive elements were obtained from mechanical testing.
3. To predict the most critical areas for initial delamination, the locations of the highest interlaminar normal and interlaminar shear stresses were identified. The most critical area under compressive loading was determined to be the region having the highest interlaminar tensile stresses, located above the wavy 0° layer at the central trough of the wave (the interface at the top of the wavy 0° layer). The Hashin failure criterion was employed to predict the occurrence of failure within

individual finite elements representing either 0° or 90° layers. A progressive failure approach was used to predict ultimate failure of cross-ply laminates with various layer waviness formations.

4. Three sets of layer waviness models with layer waviness (single, double, and triple) centered about the laminate mid-plane were used as examples to illustrate the first-ply failure analysis. For all layer waviness models, the critical locations were found in vicinity of the layer waviness. Interface delamination was identified as the first-ply failure in a majority of the layer waviness models. Failure of 90° composite lamina elements was then predicted after the initial delamination, employing the Hashin failure criterion. The material properties of failed elements were reduced using appropriate degradation factors. At this point of interface delamination formation and propagation as well as progression of 90° elements failure predicted, no fiber failure was identified in the 0° layers.
5. The progressive failure approach was used to predict the ultimate compression strength of the laminates. Delamination propagation of up to 10 element lengths (0.91 mm) were predicted in laminates having single, double, and triple wavy 0° layers centered about the laminate mid-plane prior to ultimate failure. The predicted ultimate compression strengths using progressive failure analysis were in good agreement with the experimentally determined compression strengths.
6. Separated waves with symmetry above and below the top and the bottom 90° layer were modeled to investigate the interaction effects of opposing formations of layer waviness under compressive loading. For the laminates with the top horizontal symmetry, the different opposing wave formation did not produce a significant

influence on the predicted compression strength ratios. Further, the different opposing wave formations investigated did not show any significant effects on either the first-ply or ultimate strength ratios for laminates with bottom symmetry.

7. Layer waviness occurs most often in thick composite laminates. Thus laminates containing multiple sets of waviness, either at the laminate mid-plane or at different through the thickness locations within the laminate were modeled. For the different layer wave formations having the same wave fraction and laminate thickness, results indicate that a greater number of non-wavy 0° layers at the laminate mid-plane can produce greater compression strength ratios. Further, the ultimate failure strength ratios, F_u predicted using progressive failure analysis were in good agreement with the experimental strength ratios, F_{ex}. Generally, the experimental strength ratio, F_{ex}, lies between the first-ply failure strength ratio, F_{fp}, and the ultimate failure strength ratio, F_u. Finally, a compression strength reduction due to layer waviness in composite laminates is not only dependent upon the wave fraction, but is also dependent on the through-the-thickness wave locations as well as the overall thickness of the laminate.
8. This research has demonstrated that the two-dimensional plane strain finite element modeling methodology, employing a progressive failure approach, is effective for predicting compression strength reductions in composite laminates with layer waviness.

5.2 Recommendations

Although a finite element modeling methodology using progressive failure analysis has been used successfully to investigate layer waviness effects in composite

laminates with a variety of wave geometries, thicknesses, and wave locations, additional modeling and testing is desired. Although the results from this research showed good agreement between experimental and numerical results, the number of actual specimens tested and layer wave formations modeled was limited. Additionally the layer waviness considered was of a somewhat idealized wave shape and a constant layer wave severity (δ / λ). Further research is desired to investigate compression strength reductions for composite laminates with more complex wave shapes and various values of layer wave severity. Further research is also desired to investigate layer waviness effects in laminates other than cross-ply laminates.

REFERENCES

[1] Adams, D. O. and Hyer, M. W., "Analysis of Layer Waviness in Flat Compression-Loaded Thermoplastic Composite Laminates." Journal of Engineering Materials and Technology, 1996, Issue 1, Vol. 118, pp. 63-70.

[2] Adams, D. O. and Hyer, M. W., "Effects of Layer Waviness on the Compression Strength of Thermoplastic Composite Laminates." Journal of Reinforced Plastics and Composites , 1993, Issue 4, Vol. 12, pp. 414-429.

[3] Bradley, D. J., Adams, D. O. and Gascoigne, H. E., "Interlaminar Strains and Compressive Strength Reductions Due to Nested Layer Waviness in Composite Laminates." Journal of Reinforced Plastics and Composites, 1998, Vol. 17, pp. 989-1011.

[4] Adams, D. O. and Bell, S. J., "Compression Strength Reductions in Composite Laminates Due to Multiple-Layer Waviness." Composites Science and Technology, 1995, Vol. 53, pp. 207-212.

[5] Hyer, M. W., Maas, L. C. and Fuchs, H. P., "The Influence of Layer Waviness on the Stress State in Hydrostatically Loaded Cylinders." Journal of Reinforced Plastics and Composites, Blacksburg, VA, November 1988, Vol. 7.

[6] Telegadas, H. K. and Hyer, M. W., "The Influence of Layer Waviness on the Stress State in Hydrostatically Loaded Cylinders: Further Predictions." Journal of Reinforced Plastics and Coposites, September 1990, Issue 5, Vol. 9, pp. 503-518.

[7] Telegadas, H. K. and Hyer, M. W., "The Influence of Layer Waviness on the Stress State in Hydrostatically Loaded Cylinders: Failure Predictions." Journal of Reinforce Plastics and Coposites, February 1992, Issue 2, Vol. 11, pp. 127-145.

[8] Ansys, Inc., *ANSYS 12.1*. Cannonburg, PA.

[9] Hashin, Z., "Failure Criteria for Unidirectional Fiber Composites." Journal of Applied Mechanics, 1980, Vol. 102, pp. 329-334.

[10] Adams, D. O., "Unpublished Experimental Results of Compression Strength for Composite Laminates Fabricated and Tested by Adams and Natalie Hammer."

[11] Rosen, B. W., "Mechanics of Composite Strengthning." Fiber Composite Materials, Metals Park, OH, 1995, Chapter 3.

[12] Davis, J. G. and Jr., "Compressive Strength of Fiber-Reinforced Composite Materials." Composite Reliability, ASTM STP 580, Philadephia, PA : American Society for Testing and Materials, 1975, pp. 364 - 377.

[13] Hyer, M. W., *Micromechanics of Compression in Unidirectional Composites.* Mechanical Engineering Department, University of Maryland. College Park, MD, August, 1986. Technical Report 86-9.

[14] Argon, A. S., "Fracture of Composites." Treatise on Material Science and Technology, 1972, Vol. 1, pp. 106 - 114.

[15] Budiansky, B., "Micromechanics." Computers and Structures, 1983, Issue 1-4, Vol. 16, pp. 3-12.

[16] Steif, P.S., "A model for kinking in fiber composites—I. Fiber breakage via microbuckling." International Journal of Solids and Structures, 1990, Issue 5-6, Vol. 26, pp. 549-561.

[17] Guynn, E. G., Ochoa, O. O. and Bradley, W. L., "A Parametric Study of Variables That Affect Fiber Microbuckling Initiation in Composite Laminates: Part 1-Analyses." Journal of Composite Materials, Houston, TX : American Society for Composites, 1992, Issue 11, Vol. 26, pp. 1594-1616.

[18] Shuart, M. J., *Short-Wavelength Buckling and Shear Failaures for Compression Loaded Composite Laminates.* National Aeronautics and Space Administration. Washington, D.C., November, 1985. NASA TM-87640.

[19] Peel, L.D., *Compression failure of angle-ply laminates.* Department of Engineering Science and Mechanics, Virginia Polytechnic Institute and State University. Blacksburg, VA, 1990. NASA CR-189485.

[20] Abdallah, M. G., Caims, D. S. and Gascoigne, H. E., "Experimental Investigation of Thick-Walled Graphite/Epoxy Rings Under External Hydrostatic Compressive Loading." Milwaukee, WI, 1991. Proceedings of the SEM Spring Conference on Experimental Mechanics. pp. 626-631.

[21] Harris, C. E. and Lee, J. W., *A Micromechanics Model of the Stiffness and Strength of Laminate with Fiber Waviness.* NASA Langley Research Center. Hampton, VA, July, 1988. NASA Contractor Report Nasa CR-181670.

[22] Bogetti, T. A., Gillespie, J. W.,JR and Lamontia, M. A., "Influence of Ply Waviness on the Stiffness and Strength Reduction on Composite Laminates." Journal of Thermoplastic Composite Materials, Aberdeen Proving Ground, MD, 1992, Vol. 5, pp. 344-369.

[23] Bogetti, T. A., Gillespie, J. W.,JR and Lamontia, M. A., "The Influence of Ply Waviness with Nonlinear Shear on the Stiffness and Strength Reduction of Composite Laminates." Journal of Thermoplastic Composite Materials, April 1994, Vol. 7.

[24] Adams, D. O. and Hyer, M. W., "Effects of layer waviness on the compression fatigue performance of thermoplastic composite laminates." International Journal of Fatigue, 1994, Issue 6, Vol. 16, pp. 385-391 .

[25] Chun, H.J., Shin, J.Y. and Daniel, I.M., "Effect of material geometric nonlinearities on the tensile and compressive behavior of composite materials with fiber waviness." Composites Science and Technology, 2001, Vol. 61, pp. 125-134.

[26] Hale, R. D. and M., Villa., "Influence of Opposing Wave Nesting in Compression-Loaded Composites." Journal of Composite Materials, Lawrence, KS, 2003, Issue 13, Vol. 37, pp. 1149-1166.

[27] Jumahat, A., et al., "Fracture mechanisms and failure analysis of carbon fibre-toughened epoxy composites subjected to compressive loading." Composite Structures, 2010, Vol. 92, pp. 295-305.

[28] Berbinau, P., Soutis, C. and Guz, I.A., "Compressive failure of 0° unidirectional carbon-fibre-reinforced plastic (CFRP) laminates by fibre microbuckling." Composites Science and Technology, July 1999, Issue 9, Vol. 59, pp. 1451-1455.

[29] Griffith, A. A., "The Phenomena of Rupture and Flow in Solids." Philosophical Transactions of the Royal Society of London, Series A, 1920, Vol. 221, pp. 163-198.

[30] Krueger, R., *The Virtual Crack Closure Technique: History, Approach and Applications.* NASA Langley Research Center. Hamton, VA, 2002. NASA/CR-2002-211628. ICASE Report No. 2002-10.

[31] Irwin, G. R., "Fracture." *Handbuch der Physik.* s.l. : Spring-Verlag, 1958, p. 551.

[32] Rybicki, E.F. and Kanninen, M. F., "A Finite Element Calculation of Stress Intensity Factors By A Modified Crack Closure Integral." Engineering Fracture Mechnics, 1977, Vol. 9, pp. 931-938.

[33] Rybicki, E.F., Schmueser, D.W. and Fox, J., "An energy Release Rate Approach For Stable Crack Growth in the Free - Edge Delamination Problem." Journal of Composite Materials, October 1997, Vol. 11, pp. 470-487.

[34] Ansys, Inc., *ANSYS 11.0.* Cannonburg, PA.

[35] Camanho, P.P., Davila, C.G. and Amber, D.R., *Numeriacal Simulation and Delamination Growth in Composite Materials.* National Aeronautics and Space Administration, NASA Langley Research Center. Hampton, VA : NASA, 2001. NASA/TP-2001-211041.

[36] Turon, A., et al., "An engineering solution for mesh size effects in the simulation of delamination using cohesive zone models." Engineering Fracture Mechanics, s.l. : Elsevier, 2007, Vol. 74, pp. 1665-1682.

[37] Davila, C.G., Camanho, P.P. and Turon, A., *Cohesive Element for Shells.* National Aeronautics and Space Administration, NASA Langley Research Center. Hampton, VA : NASA, 2007. NASA/TP-2007-214869.

[38] Mi, Y., et al., "Progressive Delamination Using Interface Element." Journal of Composite Materials, s.l. : SAGE, 1998, Issue 14, Vol. 32.

[39] Schellekens, J.C.J. and Borst, R. De., "Numerical Simulation of Free Edge Delamination in Graphite-Epoxy Laminates Under Uniaxial Tension." 1991. Proceedings of the 6th International Conference on Composite Structures. pp. 647-657.

[40] Wu, EM. and Reuter, Jr. C., *Crack extension in fiberglass reinforced plastics.* University of Illinois. s.l. : T&AM, 1965. Report no. 275.

[41] Reeder, Jr., *An Evaluation of Mixed-Mode Delamination Failure Criteria.* NASA National Aeronautics and Space Administration, Langley Research Center. Hampton, VA, 1992. NASA. TECHNICAL MEMORANDUM 104210.

[42] *Standard Test Method for Mode 1 Interlaminar Fracture Toughness of Unidirectional Fiber-Reforced Polymer Matrix Composite.* ASTM International. West Conshohocken, PA, 2002. ASTM Standards. D 5528 - 01.

[43] Davidson, B., *Standard test method for determination of the mode II interlaminar fracture toughness of unidirectional fiber reinforced polymer matrix composites using the end-notch flexure (ENF) test.* West Conshohocken, PA, 2010.

[44] *Magnamite 8551 - 7A Tough Resin: Graphite Prepreg Tape and Fabric Module.* Hercules Aerospace Products. UT, 1985.

[45] O'Brien, T. K. and Martin, R. H., "Results of ASTM round robin testing for mode 1 interlaminar fracture toughness of composite materials." Journal of composites Technology and Research, 1993, Issue 4, Vol. 15.

[46] Hashemi, S., Kinloch, A. J. and Williams, J. G., "Corrections needed in double-cantilever beam tests for assessing the interlaminar failure of fibre-composites." Journal of Materials Science, Issue 2, Vol. 8, pp. 125-129.

[47] Berry, J. P., "Determination of Fracture Surface Energies by the Cleavage Technique." Journal of Applied Physics, Schenectady, NY, 1963 January, Issue 1, Vol. 34, pp. 62-68.

[48] *Standard test method for detemination of the mode II interlaminar fracture toughness of undirectional fiber reinforced polymer matrix composites using the end-notched flexure (ENF) test (Draft only).* 2010. pp. 1-15, ASTM standard.

[49] Davidson, B.D. and Sun, X., "Geometry and Data Reductions for a Standardized End Notch Flexure Test for Unidirectional Composites." Journal of ASTM International, 2006, Issue 9, Vol. 3.

[50] O'Brien, T. K., *Composite Interlaminar Shear Fracture Toughness G_{IIc}: Shear Measurement of Shear Myth*, U.S. Army Research Laboratory Vehicle Technology Center, NASA Langley Research Center. Hampton, VA, Feb. 1997. NASA-TM-110280.

[51] Agarwal, B.D. and Broutman, L.J., *Analysis and Performance of Fiber Composites.* New York, USA : John Wiley and Sons, 1990.

[52] Chen, J, et al., "Predicting Progresive Delamination of Coposite Material Specimens via Interface Elements." Mechanics of Composite Materials an Structures, March 1999, Vol. 6, pp. 301 - 317.

[53] Alfano, G and Crisfield, M.A., "Finite Element Interface Models for the Delamination Analysis of Laminated Composites: Mechanical and Computational Issues." International Journal for Numerical Method in Engineering, London, U.K, 2001, Vol. 50, pp. 1701-1736.